RICE UNIVERSITY

High Resolution Optical Imaging Techniques for Rapid Assessment of Breast Cancer

by

Jessica Lupinacci Dobbs

A THESIS SUBMITTED
IN PARTIAL FULFILLMENT OF THE
REQUIREMENTS FOR THE DEGREE

Doctor of Philosophy

APPROVED, THESIS COMMITTEE:

Rebecca Richards-Kortum, Stanley C. Moore Professor and Chair
Bioengineering, Rice University

Tomasz Tkaczyk, Associate Professor
Bioengineering, Rice University

Mary C. Farach-Carson, Ralph and Dorothy Looney Chair of Biochemistry and Cell Biology, Department of BioSciences, Rice University

Wei Yang, Professor
Diagnostic Radiology, University of Texas MD Anderson Cancer Center

HOUSTON, TEXAS
MAY 2016

ABSTRACT

High Resolution Optical Imaging Techniques for Rapid Assessment of Breast Cancer

by

Jessica Dobbs

Breast cancer is the most prevalent and deadly cancer among women worldwide. The current standard for breast lesion diagnosis is histologic assessment with hematoxylin and eosin (H&E) staining. Histology has high diagnostic accuracy, but requires extensive time and resources to perform. The objective of this work was to improve diagnosis of early breast cancers by developing approaches to rapidly image and characterize neoplastic tissue and the tumor microenvironment in high resolution optical images.

Confocal fluorescence microscopy can image optical sections of tissue without the need for extensive tissue processing. Three studies were performed to evaluate if confocal microscopy images contain sufficient information to identify neoplasia in breast tissue. In a 31 patient study, five pathologists identified neoplasia with high accuracy in confocal and histologic images. In another study, an expert pathologist estimated tumor cellularity in core biopsies with moderate agreement between confocal and histologic images. In a third study, an expert pathologist assigned diagnoses and grades to neoplastic tissue in confocal and histologic images. Limitations of these studies include recruitment of patients at a single center and data assessment by a single reader in two of three studies.

Visual assessment for cancer diagnosis is limited by the potential for inter- and intra-observer error. Using a computerized algorithm to segment and quantify architectural features of

breast ducts and nuclei, a decision-tree model was developed that classified confocal images of breast tissue sites as neoplastic or non-neoplastic with an overall accuracy of 90%. Another computerized algorithm was developed to segment adipocytes in confocal images and results showed significant differences in phenotypic properties of adipocytes adjacent to neoplastic and non-neoplastic tissue.

High resolution microendoscopy (HRME) can be used to rapidly acquire images at a lower cost than confocal microscopy. In a study evaluating HRME and two approaches to improve image contrast, results demonstrated that HRME with structured illumination yields images with high contrast relative to HRME with standard illumination.

The unique contribution of these results is the characterization of qualitative and quantitative criteria to evaluate breast tissue and classify neoplasia in optical images, although recognition of invasive lobular carcinoma was limited. The criteria developed in this research may be applied to further development of techniques for objective classification and diagnosis of breast cancer in optical images.

Acknowledgments

I would like to thank my advisor, Dr. Rebecca Richards-Kortum, for being an inspiring mentor. You have been an excellent role model for me as a scientist with a true passion for what you do. I am so thankful that I got to learn from you as a member of your research team.

I would also like to thank the other members of my committee, Dr. Tomasz Tkaczyk, Dr. Wei Yang, and Dr. Farach-Carson for their advice and enthusiastic support for this research. In addition, I would like to thank Dr. Savitri Krishnamurthy for spending countless hours reviewing images and for sharing her knowledge about breast histology with me.

There are several people without whom this work would not have been possible. Thanks to Dr. Donnie Shin, whose assistance with the breast duct and adipocyte segmentation studies was very instructive and valuable to me, to Dr. Matt Kyrish for developing the structured illumination system used in the HRME study, to Dr. Henry Kuerer for his support of all the studies, and Dr. Jenna Mueller and Dr. Nimmi Ramanujam for being excellent collaborators during every phase of the duct and nuclear segmentation and classification study.

I would like to thank all the members of the Richards-Kortum Group, especially Richard Schwarz, Jennifer Carns, Vivian Mack, Eric Yang, Pelham Keahey, Jennifer Burnett, Anne Hellebust, and Ben Grant, and John Wright. Thank you for your invaluable assistance, instruction, and many helpful conversations and ideas.

A special thank you to Meaghan Bond, who was an amazing friend through every day of graduate school. Thanks for all the fun, advice, conversations, and care. I could not have done this without you.

Thank you to my parents, Cory and Julia Lupinacci, for their unending love and guidance. Your support means the world to me. I would like to thank my brother, Kevin Lupinacci, for always cheering me on and having my back. I would also like to thank my parents-in-law, Steve and Sara Dobbs, for their overwhelming support for me.

Most importantly, I would like to thank my husband, Austin Dobbs, for his endless encouragement and unwavering love and faith in me. Thank you for comforting me on every difficult day and for celebrating every accomplishment with me. I could not have done this without you by my side.

Table of Contents

LIST OF FIGURES

LIST OF TABLES

1 CHAPTER 1: Introduction

1.1 Objective and Specific Aims

The objective of this work was to improve the diagnosis of early breast cancers through the development of approaches to analyze high resolution optical images of breast tissue and quantitative criteria to characterize breast lesions and the tumor microenvironment. The following specific aims were designed to achieve this objective:

Specific Aim One: Evaluate the feasibility of identification and characterization of normal, benign, and malignant breast features in images acquired with confocal fluorescence microscopy.

Specific Aim Two: Characterize morphological features of stromal adipocytes in the breast tumor microenvironment to identify differences in adipocyte phenotype in normal tissue and adjacent to malignant lesions.

Specific Aim Three: Explore structured illumination and Lugol's Iodine as potential methods to reject background light in images acquired with high resolution microendoscopy.

1.2 Chapter Summaries

This dissertation describes the studies performed to accomplish these specific aims in the following chapters:

Chapter 1 lists the specific aims of this research and provides an overview of the research to be discussed.

Chapter 2 provides background information on the motivation and significance of this work, a brief overview of breast anatomy and histology, and a discussion on the role of breast

stroma in tumor progression and invasion. Current clinical breast imaging modalities and optical imaging techniques in development for breast imaging are reviewed.

Chapter 3 describes the development of a library breast tissue images acquired with confocal fluorescence microscopy and criteria for visual assessment and interpretation of benign non-neoplastic features, benign proliferative features, and neoplasia. The library and assessment criteria were used to perform a validation study in which five readers visually assessed confocal and histologic images based on the presence of neoplasia. Chapter 3 was published previously in *Journal of Biomedical Optics* [1].

Chapter 4 describes the results of a study in which tumor cellularity was estimated in grayscale confocal, pseudo-colored confocal, and histologic images of core needle biopsy specimens from patients diagnosed with inflammatory breast carcinoma. Chapter 4 was published previously in *Breast Cancer Research and Treatment* [2].

Chapter 5 describes the results of a study in which a diagnosis and tumor grade were assigned to histologic images of neoplastic breast tissue specimens based standard histologic criteria and to confocal images using the modified criteria described in Chapter 3 [1].

Chapter 6 describes the development of computerized algorithms to segment and analyze quantitative ductal and nuclear features in confocal images of breast tissue. These algorithms were used to create a decision tree model to classify neoplastic and non-neoplastic breast tissue in confocal images. Chapter 6 was published previously in *Breast Cancer Research* [3].

Chapter 7 describes the development of a computerized algorithm to segment and analyze parameters of adipocytes in confocal images acquired from the microenvironment of neoplastic lesions and in non-neoplastic stroma.

Chapter 8 describes the evaluation of two methods to potentially improve contrast in images acquired with high resolution microendoscopy, including structured illumination and topical application of Lugol's Iodine.

Chapter 9 provides a summary of the research presented in this dissertation.

2 CHAPTER 2: Background

2.1 Motivation and Significance

Breast cancer is the most common form of cancer among women worldwide. It was estimated that in the year 2012 there were approximately 230,000 new cases of breast cancer and 40,000 deaths due to breast cancer among women in the United States [4, 5]. There were an estimated 1.4 million new cases and 460,000 deaths worldwide in women due to breast cancer over the same period [6]. The incidence of invasive breast carcinoma varies in different geographical regions, with the highest incidence rates seen in western and northern Europe, Australia and New Zealand, and North America. [6]. The two clinical factors thought to have the greatest influence on breast cancer risk are gender and age; breast cancer incidence increases with age and the incidence rate for breast cancer is approximately 100 times higher in women than in men [5, 7]. Increased breast cancer risk is associated with many other clinical factors including family history of breast cancer, a mutation in the BRCA 1 or 2 genes, long menstrual history, use of hormone replacement therapy, prior history of breast cancer, and lack of access to screening services [6]. Some well-documented behavioral risk factors for breast cancer in the United States include being overweight or obese, a sedentary lifestyle, lack of physical activity, moderate or high consumption of alcohol, and tobacco use [8, 9].

Breast cancer is classified by stage, which is based on assessment of tumor size, lymph node involvement, and metastasis, and impacts the course of treatment. Women with early stage disease (Stage I, IIA, or IIB disease) undergo surgical resection of the lesion through lumpectomy or mastectomy, post-surgical radiation therapy, and possible chemotherapy based on the number of axillary lymph nodes involved. Treatment of regional and distant disease (Stage III and IV) involves total mastectomy followed by radiation therapy and / or targeted

chemotherapy. Chemotherapy regimens can be administered pre- or post-surgical resection depending on the extent of disease. Pre-surgical chemotherapy may be used to decrease tumor bulk to increase the possibility of total surgical resection. Chemotherapy regimens generally consist of a combination of targeted agents, which are selected according to tumor metabolism and stage of disease [10].

Five-year survival rates for invasive breast carcinoma among all women in the United States are highest (99%) when the disease is localized at the time of diagnosis [11, 12]. When breast cancer is at the regional stage, five-year survival is 85% and when the primary tumor has metastasized to a distant location, five year survival is 25% [12]. Five-year survival rates in the United States differ by race: African American women are observed to have a much lower rate of survival (79%) than non-Hispanic white women (90%), Asian American women (90.3%), American Indian women (85.6%), and Hispanic women (83.8%) [5, 12]. The lower survival rate for African American women is influenced by lower access to health care, high quality cancer screening and treatment facilities, which results in later stage at diagnosis [4, 5, 13]. There is a critical need for improved early diagnostic techniques, which are affordable enough to enable access to all racial and socioeconomic groups.

2.2 Breast Anatomy and Histology

2.2.1 Normal Breast Anatomy and Histology

Female breasts are organized into several lobes, which are innervated by a network of ducts radiating from the base of the nipple. Although several texts describe breasts as having between 15-20 lobes and milk ducts [14, 15], more recent studies have identified breasts with averages of 5-9 milk ducts [16-18]. As they lead away from the nipple, large milk ducts branch into smaller vessels which extend to the lobules. The ductal epithelium is made of columnar and

cuboidal cells, and the layer between the epithelium and basal lamina is made up of myoepithelial cells. The portions of ducts extending into lobules and the lobular units are called terminal ductal lobular units (TDLUs). Lobules are clusters of many alveolar glands, which secrete fluid during lactation. During a resting (or non-lactating state), lobular glands are surrounded by a layer of cuboidal cells and reinforced by myoepithelial cells.

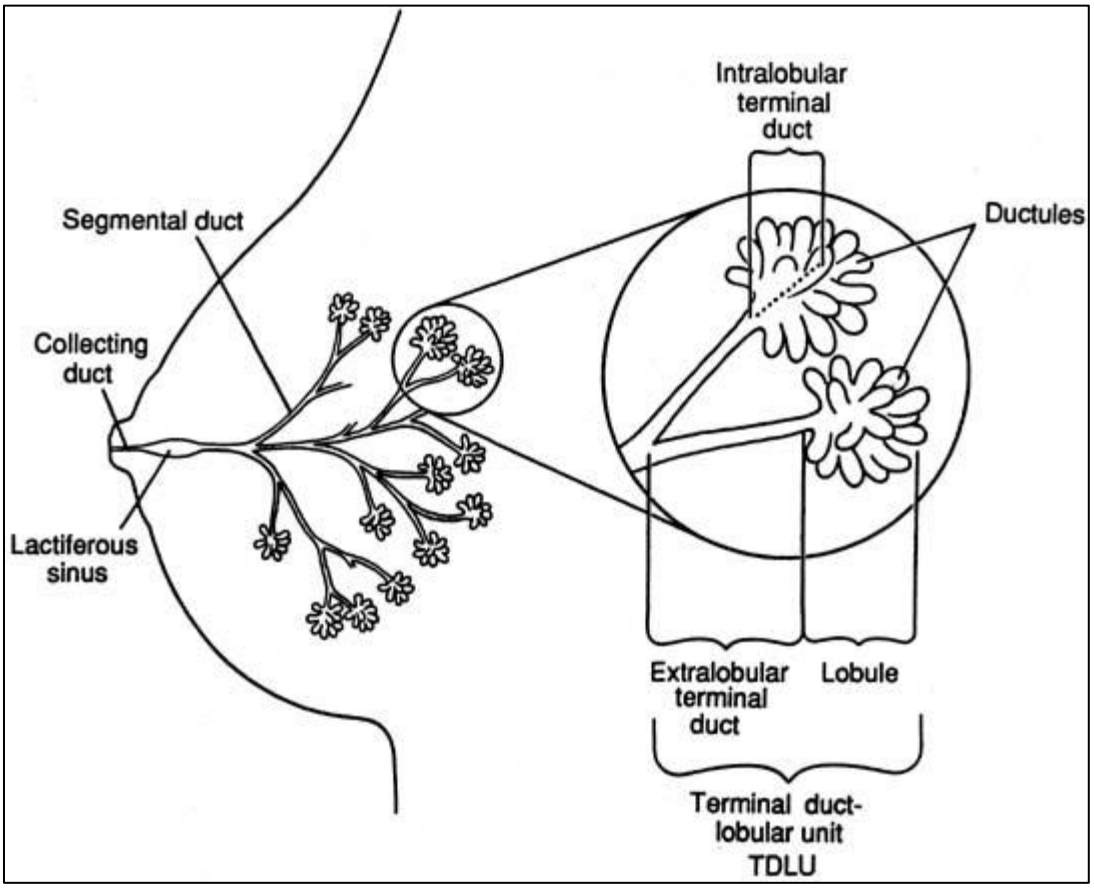

Figure 2-1: Diagram of the ductal and lobular architecture within the breast (Breast care: a clinical guidebook for women's primary health care providers, Development and growth of the breast, 1999, p. 34, Figure 3.7, WH Hindle, ©Springer-Verlag New York 1999. Used with permission of Springer [19]).

Significant changes to the molecular structure and composition of the breast occur during puberty, pregnancy, lactation, and menopause. Prior to puberty, the breasts are composed of

collagenous and adipose tissue, with little glandular tissue [15]. During puberty, an increase in the hormones estrogen and progesterone cause the breast to grow to its mature size through ductal growth and lobular differentiation and growth [15]. The mature, non-lactating female breast is composed of approximately equal amounts of glandular and adipose tissue. During pregnancy and lactation, the amount of glandular tissue increases to approximately twice that of adipose tissue [16, 20, 21]. Alveolar glands within the lobules secrete fluid and lobular epithelial cells show abundant vacuoles. When a woman is breastfeeding, milk is transported from the lobules, through the network of ducts, and to the nipple [16]. After lactation ceases milk is no longer produced, and the number and size of lobules decreases [15]. During menopause ductal and lobular epithelia undergo atrophy in response to a decrease in systemic estrogen and progesterone levels. Thus the quantity of glandular tissue decreases and the breast is primarily composed of adipose tissue and collagenous stroma [15].

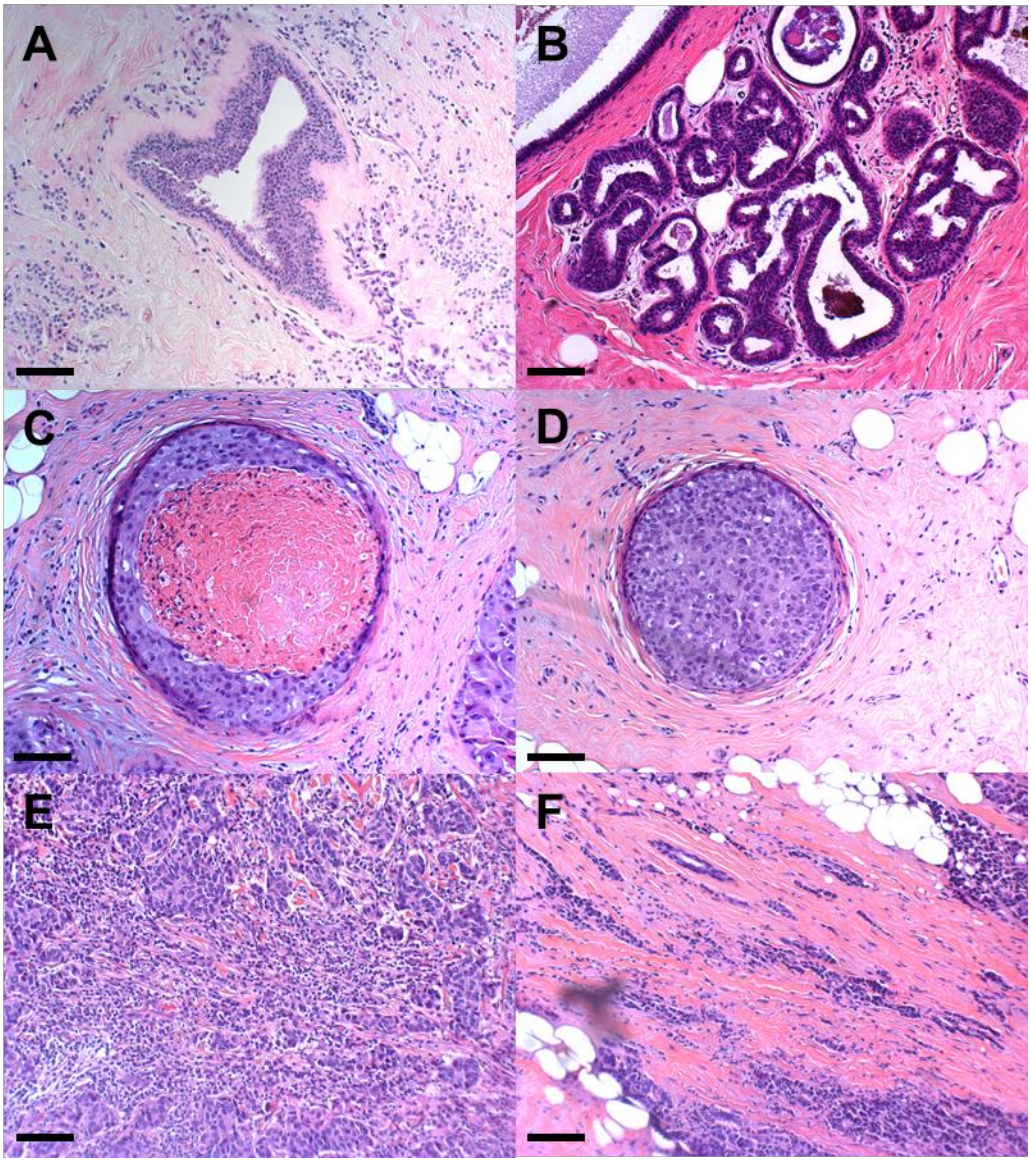

Figure 2-2: Representative high magnification histologic images of benign and malignant breast tissues stained with hematoxylin and eosin. A: Usual ductal hyperplasia. B: Atypical ductal hyperplasia. C: Comedo DCIS. D: Solid DCIS. E: Invasive ductal carcinoma of the breast. F: Invasive lobular carcinoma of the breast. Scale bars are 100 µm.

2.2.2 Benign Breast Conditions

There are a number of benign breast conditions that can occur in a normal female breast. Inflammation, which is a local increase in lymphocytes, is an immune response. Fibrosis is a localized increase in connective tissue that occurs during the formation of scar tissue in response to injury or infection. Lobules in aging breast tissue may undergo sclerosing adenosis, which causes the lobular alveoli to unfold and display disorganized histology. Ducts can also display

hyperplasia without atypia (usual ductal hyperplasia, Figure 2-2A), which is an increase in ductal epithelial cells that do not show abnormal histology such as increased mitotic events, pleomorphism, or increased nuclear size [15].

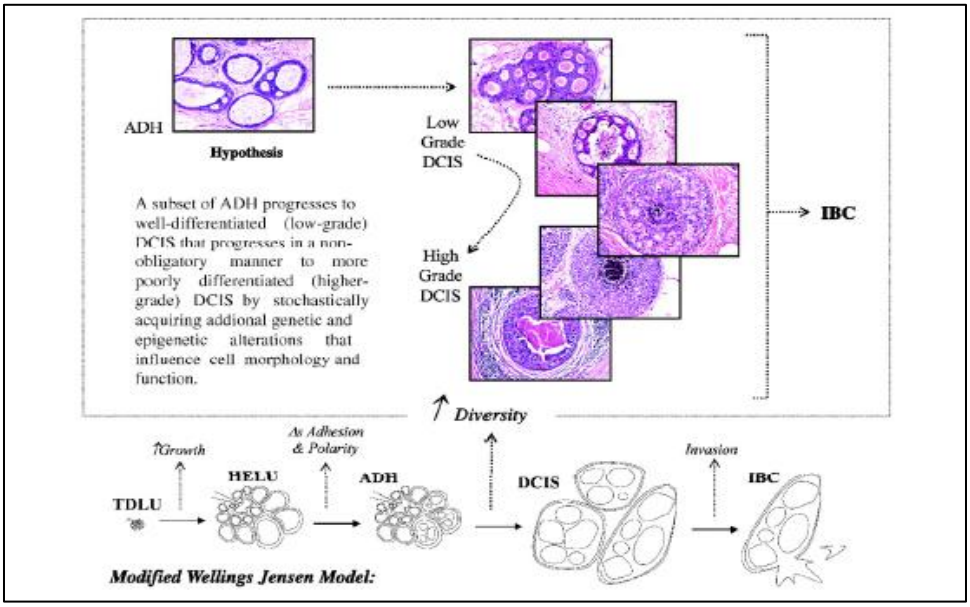

Figure 2-3: Revised Wellings and Jensen model of human breast cancer evolution. Reprinted from Clinical Cancer Research, 2008, 14/2, 370-378, Allred DC et al., Ductal carcinoma in situ and the emergence of diversity during breast cancer evolution, with permission from AACR [22].

2.2.3 Breast Carcinogenesis

The transition from normal to malignant breast tissue is a complex process. Originally, this transition was thought to be a continuum: normal TDLUs became hyperplastic enlarged lobular units (HELUs) after undergoing increased growth, HELUs progressed to atypical ductal hyperplasia (ADH) through a loss of adhesion and polarity and progression from ADH to ductal carcinoma in situ (DCIS), which progressed to invasive breast cancer (IBC) as carcinoma cells invaded the surrounding stroma [23]. This model was revised by Allred et al. [22] to reflect a more gradual, less obligatory transition from ADH to DCIS (Figure 2-3). In this revised model, some ADH foci progress to low grade (well-differentiated) DCIS, which may undergo many genetic and epigenetic changes towards high grade (poorly-differentiated) DCIS [22].

2.2.4 Pre-invasive breast cancer

Atypical ductal hyperplasia (ADH) is generally described as having some features of usual ductal hyperplasia and some features of ductal carcinoma *in situ* (DCIS). ADH is histologically distinguished from usual hyperplasia by increased mitotic activity and pleomorphism, and decreased cellular adhesion and polarity (Figure 2-2B) [15, 24]. There are various qualitative methods of distinction between ADH and DCIS which are somewhat arbitrary, including number of duct cross-sections affected and cross-sectional diameter [15].

DCIS appears to originate in the terminal duct-lobular unit (TDLU) [25], with exceptions in cases of carcinoma in major central ducts and carcinoma of the nipple [15]. DCIS is defined as a pre-invasive malignancy because it is confined within involved ducts and lobules. There are five common subtypes of DCIS with differences in architecture and malignant potential, including comedo, cribriform, papillary, micropapillary, and solid DCIS. Comedo DCIS is generally characterized as a solid proliferation of large carcinoma cells, which tend to be poorly-differentiated and pleomorphic (Figure 2-2C) [26]. Comedo DCIS is a histology that is associated with poor prognosis, generally described as having high nuclear grade, aneuploidy, high proliferation rate, over-expression of HER2, and aggressive behavior [27]. Some classifications of DCIS simply distinguish between comedo and "non-comedo" DCIS subtypes, because non-comedo DCIS subtypes tend to have the opposite characteristics, such as low nuclear grade, relatively lower rate of proliferation, and less aggressive behavior [27]. Cribriform DCIS is characterized by the arrangement of ductal epithelial cells in back-to-back orientations to form micro-lumens (Figure 2-2D, right). The papillary and micropapillary DCIS subtypes are distinguished by folds of epithelial cells projecting into the ductal lumen; micropapillary folds are smaller than those in the papillary subtype. Solid DCIS features ductal lumens entirely filled by malignant cells, with no micropapillary structure or micro-lumens (Figure 2-2D, left) [15].

The management of DCIS is controversial, with treatments ranging from local lumpectomy to mastectomy followed by radiation therapy [27]. A recent observational study following over 100,000 women diagnosed with DCIS demonstrated that, contrary to the current clinical paradigm [28, 29], DCIS follows a similar clinical course to small, invasive breast cancers and some cases have the potential for distant metastasis. This study showed that the risk of death following a diagnosis of DCIS is higher for black women and women younger than 35 years. However, a major finding of this study is that radiation therapy following lumpectomy for women with diagnosed DCIS did not lead to a significant improvement in 10-year survival rate relative to lumpectomy without radiation therapy [30].

2.2.5 Invasive breast cancer

There are several types of breast carcinoma, commonly classified to include invasive ductal carcinoma, invasive lobular carcinoma, tubular carcinoma, cribriform carcinoma, mucinous carcinoma, papillary carcinoma, micropapillary carcinoma, medullary carcinoma, carcinoma with metaplasia, and inflammatory breast carcinoma. The most common form of invasive breast disease is invasive ductal carcinoma (IDC, Figure 2-2E), which accounts for approximately 80% of breast carcinomas [31]. IDC tumors are generally dense, solid tumors, which often metastasize to lymph nodes in the axilla and have a poor prognosis.

The second most common breast malignancy is invasive lobular carcinoma (ILC), which accounts for 3-14% of breast carcinoma cases, depending on diagnostic criteria used [32-35]. ILC tumors are generally characterized by single file lines of uniform cells invading into stromal tissue (Figure 2-2F). This growth and invasion pattern is a result of low E-cadherin expression, which results in low cellular adhesion and motility [15, 24]. Medullary, tubular, and mucinous (colloid) account for 3-6% [36, 37], 1-2% [31], 1-2% [38, 39], respectively. Inflammatory breast

carcinoma (IBC) accounts for approximately 1% [40] of cases and is a very aggressive form of breast cancer, which causes edema and enlargement of the breast. IBC is characterized by young age at diagnosis, rapid onset and progression, and poor survival rates [41]. All other types of breast carcinoma account for the remaining 2% of cases [24].

2.3 The role of breast stroma in cancer progression and invasion

It has recently been suggested that breast stromal tissue plays a dynamic and influential role in breast tumor development and progression [42-45]. Collagen and adipocytes in particular are currently being investigated for their role in breast disease [46-51].

Epithelial and stromal cell proliferation is considered to be a major contributor to increased breast cancer risk [52]. The complex transition from normal to malignant breast tissue is thought to occur primarily in ductal and lobular epithelial tissue [22, 23]. It is well known that high mammographic breast density is associated with a 4-to-6-fold increase in breast cancer risk; however the molecular explanation for this association has not been fully elucidated. It was recently reported that high mammographic density is associated with high collagen density [52], which has been shown to directly promote proliferation of mammary epithelial cells *in vitro* and in murine models [47].

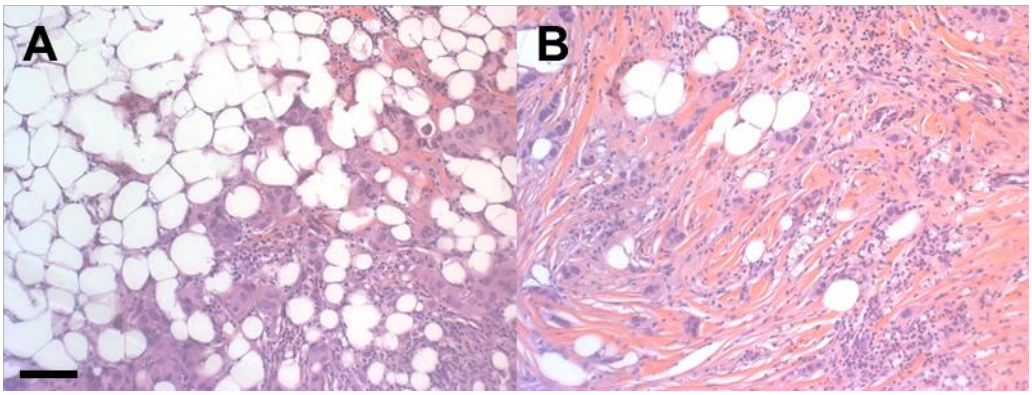

Figure 2-4: Histology of the invading front and the center of a human breast carcinoma. A: Adipocytes at the interface of the invading front show decreased size relative to normal adipocytes located at a short distance. B: At the center of the same tumor, there is an accumulation of fibroblasts and cancer-associated fibroblasts; adipocytes are not present. Scale bar is 100 μm.

Another stromal component that plays a dynamic role in tumor behavior is adipose tissue. Although adipocytes are the most common cell type in mammary tissue, they are rarely present in the center of tumors, where there are an increased number of fibroblasts and epithelial cells relative to normal breast tissue. Tan et al. have found that adipocytes near the invasive front of breast tumors tend to be smaller in size than those located a distance from the tumor (Figure 2-4)[49]. Another study showed that adipocytes co-cultured with breast cancer cells develop a fibroblast-like phenotype in which the lipid vesicles greatly decreased in size and the cells took on a spindle-shaped appearance [50]. One theory for this dramatic change in adipocyte phenotype is that, as a result of crosstalk between adipocytes and breast cancer cells, adipocytes undergo de-differentiation [49]. Co-culturing adipocytes and cancer cells (Figure 2-4) has shown evidence of this crosstalk at a molecular level, including a decrease in adipocyte markers and an overexpression of matrix metalloproteinase-11 (MMP-11) – an ECM-remodeling proteinase associated with tumor invasion and interleukin-6 (IL-6) – a cytokine associated with inflammation [50].

Adipocytes have been shown to influence their surroundings to promote tumor growth and invasion [49, 50, 53]. Continued study of mammary collagen and adipocytes is needed to investigate the role of interaction of these components with pre-malignant lesions and to determine the association between phenotype and clinical outcome. Research to develop high resolution molecular imaging techniques to visualize these stromal components is in the early stages.

2.4 Current methods for breast cancer screening and diagnosis

Common methods for detection of breast carcinoma include self-breast exams, clinical breast exams, mammography, ultrasound, and magnetic resonance imaging (MRI). These clinical imaging techniques are commonly used to indicate the presence of suspicious lesions, but are limited by a number of factors including low sensitivity and specificity, and a dependence on age, breast density, and menopausal status [54-59].

Clinical breast examination (CBE) of the breast is based on visual inspection and palpation of the breast and lymphatic areas according to standard guidelines [56]. CBE is performed by a physician either during a routine physical examination or following identification of a mass during breast self-examination. Based on findings of CBE, including appearance and texture of the nipple and nodularity, and size and shape of the mass, physicians record the findings of the CBE as either normal or abnormal - suspected benign finding or suspicious of malignancy. If findings are abnormal, a follow-up examination is recommended [56, 58]. Data from several studies on the accuracy of CBE have demonstrated that CBE identifies some breast cancers missed by mammography [57, 60]. Sensitivity and specificity of breast cancer diagnosis by CBE has been estimated by pooling results from several studies; values range from 17.9-58.8% and 92-98.8%, respectively [55, 57, 61, 62].

Mammography is used as both a screening and diagnostics technique for breast cancer in women. The introduction of mammography screening programs resulted in a significant decrease in breast cancer mortality in the United States and other countries [63-65]. During mammography procedures, X-ray images are generally obtained from 2 conventional views of the breast: cranio-caudal (X-ray from the head to the feet) and medio-lateral oblique (from the medial to the lateral side of the body, at an angle). The X-ray images are reviewed by radiologists, who assess the findings using the American College of Radiology Breast Imaging Reporting and Data System (BI-RADS) five point scale: 1 = negative, 2 = benign finding, 3 = probably benign finding, suggest a short follow up time, 4 = suspicious of abnormality, biopsy should be considered, and 5 = highly suggestive of malignancy [66]. Sensitivity and specificity values for mammography have been reported as ranges from 33-98.5% and 75-98.8%, respectively [59, 61, 62, 67-70]. Several studies have demonstrated that sensitivity of mammography is dependent on patient age and breast density: sensitivity is much lower for patients younger than 45-50 years, and in women with high breast density [67-69, 71]. Deceased mammographic sensitivity was also observed in patients with increased tumor size and a family history of breast cancer [69]. In addition, a recent study found that mammography is associated with an increased breast cancer risk among carriers of BRCA 1/2 mutations who are younger than 30 years [72].

Ultrasound (US) is another imaging technique used to assess suspicious breast lesions. US imaging is performed by a radiologist who evaluates the mass according to criteria describing lesion shape, margin features, and acoustic properties [73]. Like mammography findings from US scans are reported using BI-RADS categories [66]. Ultrasound sensitivity and specificity has been reported as values ranging from 40-98.4% and 34-96.8%, respectively [61, 62, 68, 70, 73].

Similar to mammography, US sensitivity is dependent on patient age and breast density – lower sensitivity is associated with patient age younger than 50 and high breast density [71]. Another limitation of US is the tendency for overestimation of tumor size [61].

Magnetic Resonance Imaging (MRI) for breast lesion assessment is performed using a standard MRI system with a bilateral breast coil. MR images are assessed using a similar pattern to BI-RADS classification, through integration of morphology and enhancement kinetics [74]. Reported ranges of MRI sensitivity and specificity are 79.5-94.4% and 26-97.2% [61, 70, 75]. Like US, MRI is limited by a tendency to overestimate tumor size [61]. MRI is an expensive procedure, with the average cost for a bilateral scan at approximately $1,000; by comparison, the average cost for a bilateral mammogram is approximately $50 [76].

Although breast cancer is often detected with low resolution imaging techniques, the gold standard for breast cancer diagnosis is histologic assessment, an extensive and time-consuming process that requires core needle biopsy or surgical tissue excision and rigorous tissue preparation. Immunohistochemistry (IHC) is often performed on histologic slides to characterize expression of relevant biomarkers, such as estrogen and progesterone receptors, HER-2/neu, and markers of proliferation, including p53 and Ki-67 [10, 77]. Highly trained pathologists evaluate fixed and stained tissue samples for presence and type of malignant breast tissue based on standardized histologic criteria [15, 78-80]. Malignant breast tumors are graded and categorized to reflect their expected pattern of progression. Bloom and Richardson developed one of the most widely used grading systems for breast tumors, which used only qualitative criteria to evaluate breast lesions [78]. Elston and Ellis published the Nottigham modification incorporating semi-quantitative criteria into the Bloom and Richardson grading system [80]. Extensive research to evaluate the rate of inter- and intra-observer discordance using these grading systems

and while some studies have shown that inter-observer agreement is high in the majority of cases [81], other studies have shown that subjective criteria can lead to inter-observer variation for margin assessment and poor reproducibility in evaluation of borderline and *in situ* lesions [82-87].

2.5 Optical imaging for breast tissue characterization

Optical imaging has the potential to address the limitations of conventional breast cancer detection and diagnosis techniques. There are multiple modalities of optical imaging techniques, including optical coherence tomography, confocal reflectance microscopy, confocal fluorescence microscopy, fiber optic microendoscopy, and a variation of fiber optic microscopy that employs structured illumination.

Optical coherence tomography (OCT) is a high resolution optical imaging modality which uses near-IR light as the light source for tissue illumination [88, 89]. Diverse scattering and absorption properties of different tissues provide endogenous contrast, so an exogenous contrast agent is unnecessary. OCT has been used in several studies to image human axillary lymph nodes and breast tumor margins [90-94]. McLaughlin et al. performed a study comparing OCT to histologic assessment for identification of metastatic cells in lymph nodes [90]. The results of this study showed that OCT was able to accurately distinguish lymph nodes from surrounding adipose tissue and identify evidence of metastatic cells in lymph nodes [90]. Nguyen et al. performed a 37 patient clinical study using OCT to assess breast tumor margins [91]. Based on comparison to histology, OCT had a sensitivity of 100% and a specificity of 82% for assessment of positive and negative tumor margins [91]. A multicenter, prospective study published by Zysk et al. in 2015 was performed to investigate the feasibility of using a handheld OCT probe to assess tumor margins following breast-conserving surgery and to evaluate

potential impact on the rate of reoperation. Of the 46 patients enrolled in the study, 8 patients had positive margins following breast-conserving surgery and the OCT device identified positive margins in 5/8 (63%) patients [94]. These results demonstrate that OCT can be used for real-time intraoperative assessment of breast tumor margins.

Confocal microscopy is an emerging tool that may address the limitations of current histologic approaches by providing imaging of tissue architecture and morphology with subcellular resolution in real time without the need for extensive tissue processing. When used with targeted agents, it also may enable rapid assessment of biomarkers. Some advantages of using confocal microscopy as an alternative to histologic assessment include are the ability to acquire images at the point-of-care and to use either reflectance or fluorescence mode with multilaser systems providing the ability to excite more than one fluorescent label. Confocal reflectance microscopy has been shown to capture high-resolution images of cellular and nuclear morphological features [95]. Tilli and colleagues showed that acetic acid enhanced image detail in confocal reflectance images of mouse mammary and resected human breast tissue [96]. Confocal reflectance microscopy of core-needle breast biopsy specimens enabled measurements of nuclear size, all of which were found to be within published ranges. Comparison of confocal reflectance images with histologic images showed that confocal reflectance microscopy can distinguish benign and malignant breast tissue [96]. Confocal fluorescence microscopy has not been used previously to evaluate breast carcinoma specimens. However, it has been used in a few studies to image melanoma [97] and basal cell carcinoma in Mohs skin excisions [98].

A simpler, cheaper and more portable alternative to confocal microscopy is high resolution microendoscopy (HRME). HRME is an optical imaging technique that, when coupled with an optical contrast agent, can obtain images of tissue *in vivo* with sub-cellular resolution in

precancerous and malignant lesions in the oral cavity, esophagus, and axillary lymph nodes [99-101]. The light source for HRME is a blue light emitting diode (LED) with excitation wavelength centered at 455nm to excite the optical contrast agent, proflavine. Images are obtained with HRME by placing a coherent fiber bundle consisting of 30,000 fibers on the sample surface after topical application of proflavine (Figure 2-5). Light from the LED is transmitted through the fiber bundle to the sample where tissue stained by the contrast agent is excited by light from the LED. Fluorescence emission is collected by the fiber bundle and transmitted through a dichroic mirror to a CCD camera [101]. The HRME system has been utilized in several studies to image the oral cavity [101], Barrett's esophagus [100], and axillary lymph nodes [99].

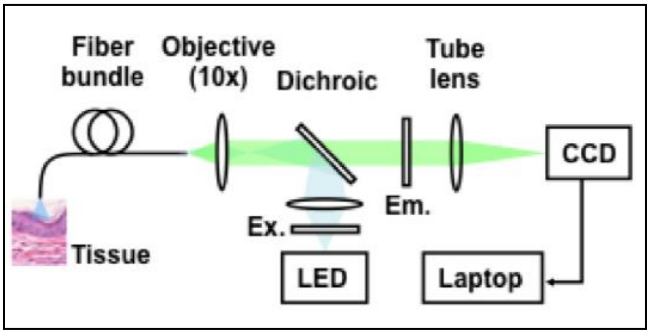

Figure 2-5: Optical diagram of the fiber optic micro-endoscope [Rosbach KJ et al. Biomed. Opt. Express, 2010][102]. Figure is from an open-access article distributed under the terms of the Creative Commons Attribution-Noncommercial-No Derivative Works 3.0 Unported License, which permits download and redistribution, provided that the original work is properly cited.

However, a major limitation of image acquisition with HRME, particularly for highly scattering tissues, is low resolution relative to confocal laser scanning microscopy. Structured illumination microscopy [103] is an inexpensive alternative to confocal microscopy that addresses the limitation of low resolution by illuminating tissue samples with a periodic light pattern to achieve optical sectioning. A one-dimensional grid or a sine wave [104] pattern is projected onto the sample and is refocused at the excitation plane, from which image is acquired.

During this procedure, three fluorescence images are acquired at the same axial depth, from three different positions of the grid separated laterally by one third of the grid period [105, 106]. An optically-sectioned image is produced by combining the three raw images with the following algorithm:

$$I_{SIM}(x) = \frac{1}{3\sqrt{2}}\sqrt{(I_1(x) - I_2(x))^2 + (I_2(x) - I_3(x))^2 + (I_3(x) - I_1(x))^2}$$ [105]

The three raw images are represented by the variables $I_1(x)$, $I_2(x)$, and $I_3(x)$, and *x* designates a 2D coordinate in the imaging plane [105]. Structured illumination microscopy has been used previously to detect cellular changes associated with cervical pre-malignant lesions [107]. A recent report described a high resolution microendoscope system using structured illumination microscopy (SI-HRME) and demonstrated the feasibility of using structured illumination microscopy to image thick samples with significant background signal [105]. Keahey et al. developed a portable structured illumination microendoscope system and quantified axial response of the system in optical phantoms in order to optimize modulation frequency. The optimized system was used to evaluate image contrast in *ex vivo* cervical columnar epithelium [108]. This system was also used to demonstrate the feasibility of structured illumination microendoscopy to evaluate response to treatment in murine mammary glands [109].

3 CHAPTER 3: Feasibility of confocal fluorescence microscopy for evaluation of neoplasia in fresh human breast tissue: outlining preliminary criteria for assessment of a confocal image library[1]

ABSTRACT: Breast cancer management could be improved by developing real-time imaging tools to assess tissue architecture without extensive processing. We sought to determine whether confocal fluorescence microscopy provides sufficient information to identify neoplasia in breast tissue. Breast tissue specimens were imaged following proflavine application. Regions of interest (ROIs) were selected in histologic slides and in the corresponding region on confocal images then divided into sets for training and validation. Readers reviewed images in the training set and evaluated images in the validation set for the presence of neoplasia. Accuracy was assessed using histologic diagnosis as the gold standard. 70 tissue specimens from 31 patients were imaged; 235 ROIs were identified and diagnosed as neoplastic or non-neoplastic. A training set was assembled using 23 matched ROIs; 49 matched ROIs were assembled into a validation set. Neoplasia was identified in histologic images: 93% sensitivity, 97% specificity (Area under the curve, AUC=0.987) and confocal images: 93% sensitivity, 93% specificity (AUC=0.957). Confocal fluorescence microscopy produced images of architectural features in breast tissue comparable to conventional histology while requiring little processing. Potential applications include assessment of excised tissue margins and evaluation of tissue adequacy for bio-banking and genomic studies.

[1] The contents of this chapter have been published in the following journal article: Dobbs JL, Ding H, Benveniste AP, Kuerer HM, Krishnamurthy S, Yang W, Richards-Kortum R. Feasibility of confocal fluorescence microscopy for real-time evaluation of neoplasia in fresh human breast tissue. J Biomed Optics 2013; 18(10), 106016. (Oct 28, 2013). ; http://dx.doi.org/10.1117/1.JBO.18.10.106016

3.1 Introduction

Approximately 1 in 8 women in the United States will develop breast cancer in their lifetime [110]. An estimated 207,000 new cases of breast cancer will be diagnosed in the United States in the next year, and approximately 40,000 U.S. women will die of this disease in the same period [111]. Currently, histologic assessment is the gold standard for differentiating neoplastic from non-neoplastic lesions to diagnose breast cancer. However histologic assessment has limitations, including the requirement for extensive tissue processing, and it takes several days to complete preparation before samples can be assessed by pathologists. Furthermore, if cores or tissue excised are inadequate for clinical diagnosis or research applications, an additional tissue excision procedure must be performed. Frozen section pathology can be performed the same day as tissue excision [26, 112]; however, frozen section has shown to be limited by sampling variability, which can lead to false negatives [113, 114]. Breast pathology experts in the United States [115] and Europe [116, 117] do not recommend frozen section for breast lesions which cannot be identified by macroscopic examination, are smaller than 10 mm in size, and for which a preoperative diagnosis is not possible [115, 116, 118]. Fine needle aspiration cytology (FNA) can also be used for rapid breast lesion assessment [113, 116], but does not preserve tissue architecture in the context of the lesion microenvironment. There is a need for a rapid technique that provides high resolution morphologic detail to differentiate neoplastic from non-neoplastic breast lesions in real-time to inform management of breast disease.

Confocal microscopy is an emerging tool that may address the limitations of current histologic approaches by providing images of tissue architecture and morphology with subcellular resolution in real time without the need for extensive tissue processing [96, 98, 119-121]. Confocal fluorescence images can be obtained in either reflectance or fluorescence mode.

When used following topical application of acetic acid, confocal reflectance microscopy can be used to acquire high-resolution images of excised breast tissue that reveal cellular and nuclear morphological features characteristic of neoplasia [95]. Application of proflavine enhances contrast in confocal images by staining DNA within nuclei. Proflavine was recently used as an optical contrast agent to assess Barrett's esophagus and axillary lymph nodes [99, 100, 122], and results from these studies demonstrate that fluorescence microscopy with proflavine yields images with morphologic detail that is visually comparable to that of histologic sections.

The goal of this work was to determine whether confocal fluorescence images of fresh human breast tissue provide sufficient information to enable discernment of neoplastic and non-neoplastic breast features. To achieve this goal, we characterized the microscopic features of normal, benign and neoplastic breast biopsies visible using confocal microscopy, and assessed diagnostic accuracy using these features compared to the gold standard of histology.

3.2 Materials and Methods

Patients were eligible for the study if they were undergoing surgery for breast cancer or ultrasound-guided core needle breast biopsy for untreated, newly diagnosed inflammatory breast cancer [123]. The study protocol was reviewed and approved by the institutional review boards of The University of Texas MD Anderson Cancer Center and Rice University, and each participant gave written informed consent. Thirty-one patients with known primary breast cancer who presented for imaging staging or for surgery agreed to participate in the study between November 2010 and February 2012. A total of 70 tissue specimens were collected: 62 specimens were obtained from 23 patients who underwent a surgical excision procedure and 8 specimens were obtained from 8 patients who underwent a core-needle biopsy procedure. Of the specimens imaged, 25 consisted of normal or benign tissue, 11 were diagnosed as ductal carcinoma *in situ*,

19 as invasive ductal carcinoma, 13 as invasive lobular carcinoma, and 2 as mucinous carcinoma.

For surgical specimens, two specimens (approximately 15 × 15 mm in size, with thickness varying between 2-7 mm) were taken from excised tissue within 10 minutes of resection; one specimen was selected from a grossly normal-appearing region and the other from an area that appeared grossly to contain neoplastic tissue. For core-needle biopsy specimens, a single core of breast tissue was obtained within 5 minutes of the procedure; core biopsy specimens were typically $1 \times 4 \times 12$ mm^3 in size. Specimens were kept moist in isotonic PBS (pH = 7.4) prior to imaging. Imaging was performed *in vitro* within 10 minutes of tissue removal. The superficial cell layers of fresh tissue specimens were stained before imaging by applying 0.01% proflavine in sterile PBS to the surface for 1 minute [124]. Proflavine is a fluorescent topical antiseptic; it preferentially stains nuclei and has been used previously as a contrast agent for fluorescence confocal microscopy [100, 122]. Proflavine has an excitation maximum of 460 nm and an emission maximum of 530 nm. After staining, tissue specimens were washed for 1 minute in isotonic PBS. A white-light photograph was taken with a digital camera to record tissue shape and gross appearance.

Confocal fluorescence images of each specimen were obtained using a scanning confocal microscope (Vivascope 2500®; Caliber Imaging and Diagnostics Inc., Rochester, NY). Images were obtained at 488 nm excitation with a 550nm ± 44 nm bandpass filter using a 30X water immersion objective lens with a numerical aperture of 0.8. At these settings, the lateral resolution was 1.0 μm at the center of the region of interest (ROI), the axial resolution was 5.0 μm at the center of the ROI, and the ROI was 750 × 750 μm. Images were acquired at a frame rate of 9 frames per second.

Tissue specimens were positioned on the microscope stage. The imaging depth was set to acquire images from the superficial cell layers of the tissue specimen and up to 60 μm into the tissue surface. Illumination power was initially set to 2.0 mW (± 0.4 mW) and manually adjusted to maximize signal while avoiding saturation. For the surgical specimens, the stage was scanned to obtain images from adjacent ROIs at the same axial depth in a grid pattern to create a composite image with a maximum area of 12.2 × 12.2 mm. For the core-needle biopsy specimens, the composite images comprised the surface of the entire specimen; approximately 4 × 12.2 mm. For each specimen, a series of three composite images was acquired at three different axial depths in increments of 20 μm beneath the surface. Total imaging time for each specimen was approximately 10 minutes. After imaging, each specimen was placed in a tissue cassette, fixed in 10% buffered formalin, and submitted for routine processing and histologic assessment by a dedicated breast pathologist.

Composite confocal images were visually compared to images of hematoxylin and eosin (H&E)–stained tissue sections at 4X magnification to identify ROIs with similar prominent architectural features. Confocal and histologic images of these areas were examined at higher magnification; single 750 × 750-μm ROIs obtained with the confocal microscope were compared to histologic images at 10X magnification (Fig. 1). Matched ROIs containing features that had similar appearances in the histologic slides and the corresponding confocal microscopy images were selected by two observers blinded to the histologic diagnosis (HD, JD); a board-certified, dedicated breast pathologist (SK) reviewed the H&E–stained image of each of these matched ROIs and provided a diagnosis using standard histologic criteria [15]. The confocal images of the matched ROIs were examined and compared to the corresponding histologic image to establish which features of neoplastic and non-neoplastic breast tissues could be imaged using confocal

fluorescence microscopy with proflavine staining; the procedure for identifying matching ROIs is shown in Figure 3-1. The matched ROIs were used to assess the ability of pathologists to identify the presence of neoplasia in a confocal fluorescence image.

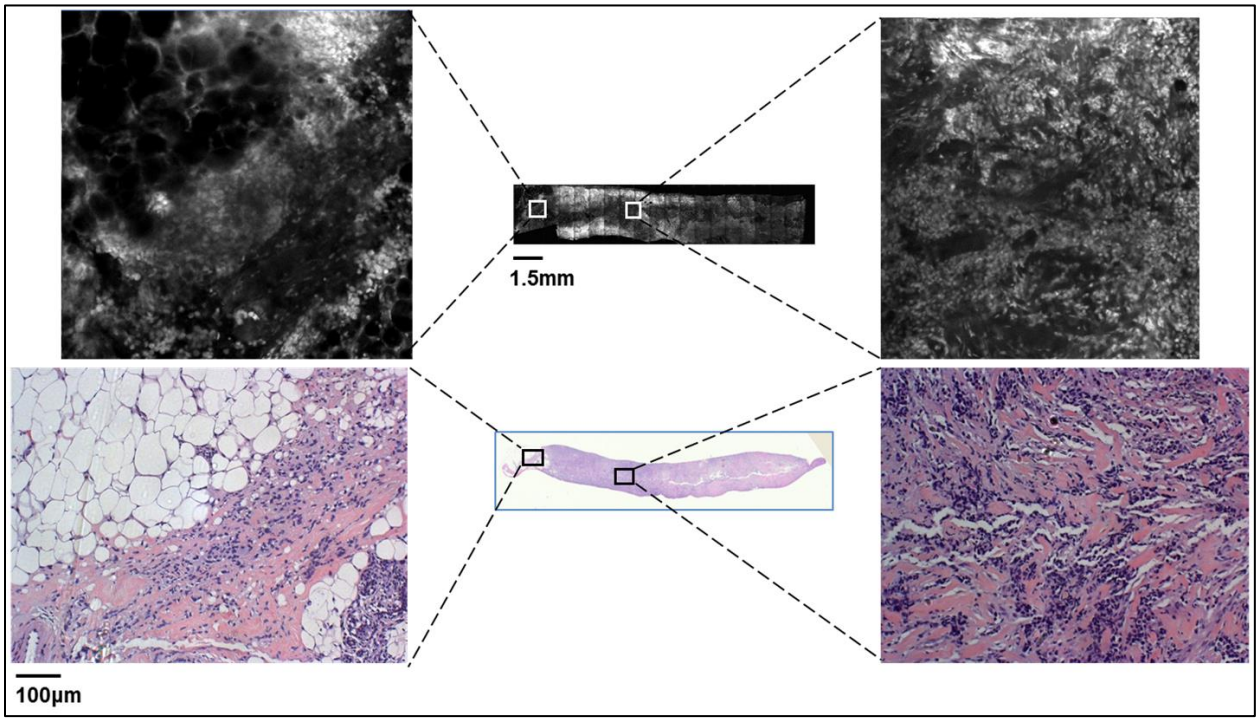

Figure 3-1: Schematic of the procedure used to identify matching regions of interest within images acquired by the confocal fluorescence microscopy system (top right, left, and center) and conventional histology (bottom right, left, and center). The two center images are low-resolution images of the entire breast core biopsy specimen. The high-resolution images at left represent a region of tissue exhibiting histologic transition from normal to neoplastic (invasive ductal carcinoma). The high-resolution images at right represent a region of tissue with invasive carcinoma. Scale bars are 1.5 mm for the low-resolution images and 100 μm for the high-resolution images.

To investigate the intensity of proflavine staining vs. histologic diagnosis, the mean fluorescence intensity was calculated for a representative group of ROIs from each diagnostic category. Confocal fluorescence images were manually segmented to isolate regions with morphology of interest, including non-hyperplastic ducts, hyperplastic ducts, ductal carcinoma *in situ*, and invasive ductal carcinoma. Fluorescence intensity was normalized by the laser power used for image acquisition and a mean fluorescence intensity value was measured for each region

by calculating the average pixel brightness over the area of the region. Statistical analysis of mean fluorescence intensity was performed using Student's t-test.

To compare the performance of confocal fluorescence microscopy and conventional histology, a validation study was performed using corresponding confocal and histologic images to calculate the sensitivity and specificity of these techniques for distinguishing between neoplastic and non-neoplastic breast features. A subset of matched confocal and histologic images was selected for use as a training set; these images were displayed side-by-side to familiarize readers with features of neoplasia visible in confocal fluorescence images. A subset of the remaining matched ROIs were used to create a validation set to compare the ability of readers to identify the presence of neoplasia in either confocal fluorescence images or standard histologic images. Readers first reviewed the training set for approximately 10 minutes. Readers were then asked to review histologic and confocal fluorescence images in the validation study based on standard histologic criteria and to use criteria presented in the training set to assist with review of confocal fluorescence images. Readers ranked images on a scale of 1-5 (1 = normal tissue or non-proliferative adipocytes, collagen, lobules, and ducts; 2 = indecisive between normal and benign changes; 3 = benign changes such as mild hyperplasia, chronic inflammation, fibrocystic changes and fibrosis; 4 = indecisive between benign changes and neoplasia; 5 = neoplastic tissue including ductal carcinoma *in situ*, invasive ductal carcinoma, and invasive lobular carcinoma). Both confocal fluorescence and histology images in the validation study were presented in random order. Accuracy was assessed relative to diagnosis by histology, which was made by a certified, dedicated breast pathologist (SK).

3.3 Results

A total of 235 unique ROIs were identified in the confocal fluorescence images that could be matched to an ROI in the corresponding standard histologic slide; a summary of patients, specimens, and ROIs from which data were acquired is shown in Table 3-1. Forty-nine ROIs showed histologically normal, non-neoplastic breast tissue. Figure 3-2 shows representative confocal fluorescence images of normal breast features with images of corresponding features identified in conventional histologic slides: adipocytes, collagen, blood vessels, ducts, and lobular units. Both confocal fluorescence images and conventional histologic images show closely packed adipocytes (Figure 3-2A, F). In confocal images, adipocytes exhibit weak proflavine staining of the pericellular nuclei, moderate staining of the cell membranes, and no staining of the lipid droplets within the cytoplasm (Figure 3-2F). Confocal fluorescence images of extracellular matrix are characterized by brightly stained fibroblast nuclei interspersed throughout bundles of collagen fibers, which exhibited weak proflavine staining (Figure 3-2B, G). Blood vessels are easily recognized in confocal fluorescence images; the nuclei of the endothelial cells are stained moderately with proflavine and arranged around a dark lumen (Figure 3-2C, H). Confocal fluorescence images of individual ducts show weakly stained myoepithelial and columnar cell nuclei that surround an unstained lumen (Figure 3-2D, I). Confocal and histologic images show cells arranged in acini to form terminal ductal lobular units (TDLU, Figure 3-2E, J). Confocal fluorescence images of lobules are characterized by intensely stained epithelial cell nuclei (Figure 3-2J).

Table 3-1: Summary of patients, specimens, and ROIs. *Non-neoplastic specimens contained sites with normal histologic features observed in the breast and features representative of benign changes.

	#	ROI
Patients	31	
Surgical tissue excision	23	
Core biopsy	8	
All specimens	70	235
Surgical tissue excision	62	208
Core biopsy	8	27
Non-neoplastic specimens	25	110
Normal	25*	49
Benign changes	25*	61
Neoplastic specimens	37	125
Ductal carcinoma *in situ*	11	27
Invasive ductal carcinoma	19	66
Invasive lobular carcinoma	13	28
Mucinous carcinoma	2	4

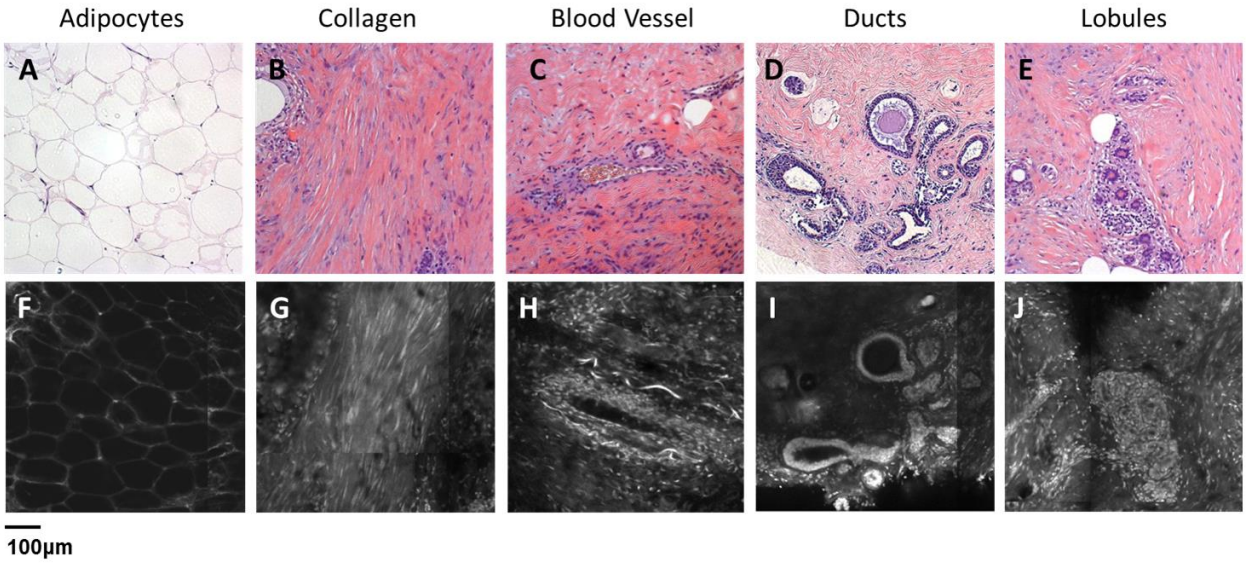

Figure 3-2: Normal, non-neoplastic breast architectural features (from left): adipocytes (A, F), collagen (B, G), blood vessel (C, H), ducts (D, I), and lobules (E, J). A-E: Architectural features in human breast tissue specimens prepared according to standard histologic technique with H&E staining. F-J: Architectural features from the same fields of view as A-E imaged with confocal fluorescence microscopy. Scale bar is 100 μm.

Sixty-one ROIs showed breast features considered to be non-neoplastic benign changes. Figure 3-3 shows representative confocal images of benign breast features with corresponding standard histologic images: chronic inflammation, fibrosis, mild hyperplasia, and fibrocystic changes. Chronic inflammation is identified in histologic images by the increased number of lymphocytes (Figure 3-3A). On corresponding confocal images, chronic inflammation is characterized by clusters of small, intensely stained inflammatory cell nuclei (Figure 3-3E). Fibrosis in confocal and histologic images is associated with an increased number of fibroblasts diffusely distributed throughout the stroma (Figure 3-3B, F). Confocal images of ROIs with fibrosis show fibroblasts with intensely stained nuclei interspersed throughout weakly stained collagen fibers in the stroma (Figure 3-3F). Mild ductal hyperplasia without atypia was identified in histologic images by an increase in number of cells lining a ductal space (Figure 3-3C, G). This increase in cell number is also evident in confocal images, where the columnar cell nuclei are weakly stained with proflavine (Figure 3-3G). Confocal and histologic images of sclerosing adenosis, a hallmark of fibrocystic changes, show distortion of acini with stromal fibrosis in TDLUs (Figure 3-3D, H). Sclerosing adenosis is identified in confocal images by small, weakly stained cuboidal cell nuclei that formed distorted acinar structures (Figure 3-3H).

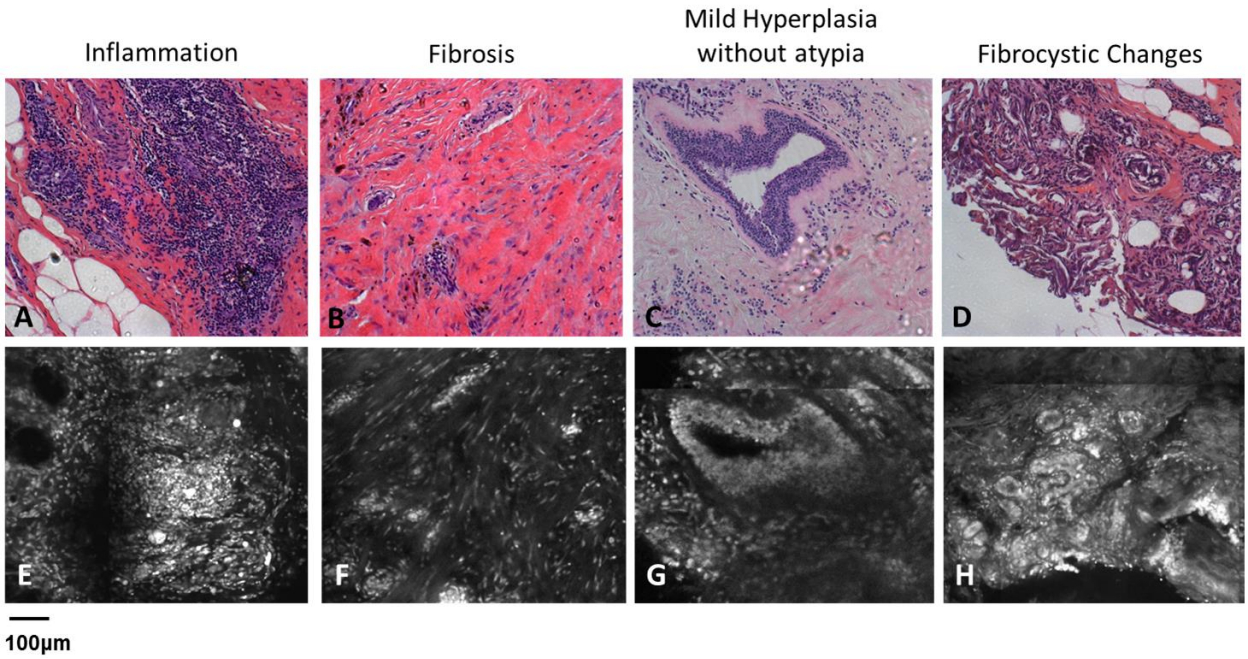

Figure 3-3: Benign, non-neoplastic breast architectural features (from left): Inflammation (A,E), fibrosis (B,F), mild hyperplasia without atypia (C,G), and fibrocystic changes (D,H). A-D: Architectural features in human breast tissue specimens prepared according to standard histologic technique with H&E staining. E-H: Architectural features from the same fields of view as A-E imaged with confocal fluorescence microscopy. Scale bar is 100 μm.

One hundred and twenty-five ROIs showed histologically neoplastic breast tissue. Figure 3-4 shows representative confocal and histologic images including neoplastic features: ductal carcinoma *in situ*, invasive ductal carcinoma, and invasive lobular carcinoma. Ductal carcinoma *in situ* was identified in histologic and confocal images by disorganized cell proliferation in ducts with no invasion into the surrounding stroma (Figure 3-4A, D). Invasive ductal carcinoma was characterized in histologic images by disorganized invasion of ductal carcinoma cells into stroma (Figure 3-4B). In confocal fluorescence images, invading ductal carcinoma cells show large, pleomorphic, weakly stained nuclei (Figure 3-4E). Invasive lobular carcinoma was characterized in histologic images by lobular carcinoma cells invading single-file into stroma (Figure 3-4C). These cells are easily identified in confocal fluorescence images, which show single-file invading cells with enlarged, intensely stained nuclei (Figure 3-4F).

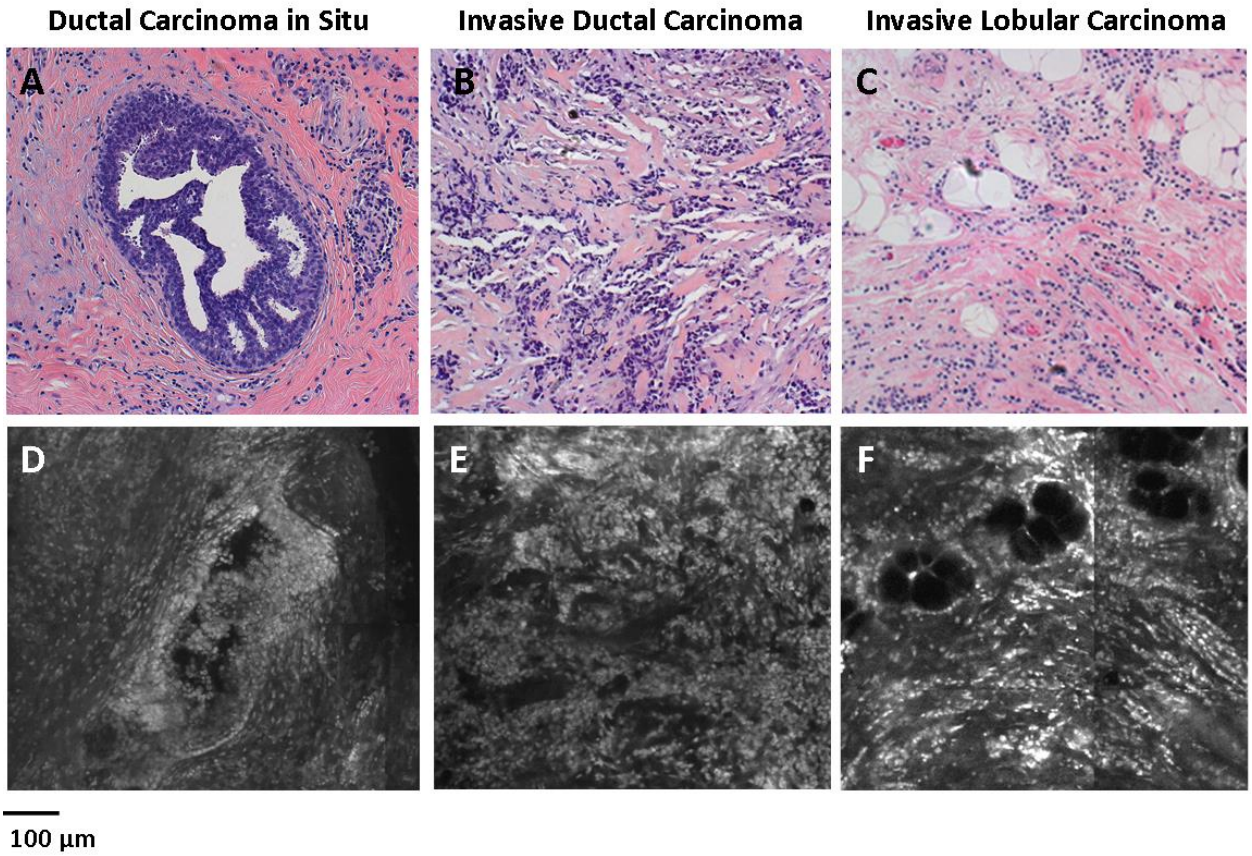

Figure 3-4: Neoplastic breast architectural features (from left): ductal carcinoma in situ (A,D), invasive ductal carcinoma (B,E) and invasive lobular carcinoma (C,F). A-C: Architectural features in human breast tissue specimens prepared according to standard histologic technique with H&E staining. D-F: Architectural features from the same fields of view as A-B imaged with confocal fluorescence microscopy. Scale bar is 100 μm.

The representative images of normal, benign, and neoplastic features (Figure 3-2, Figure 3-3, Figure 3-4) demonstrate that confocal fluorescence images capture a wide range of histologic features of the breast, which can be observed using standard histology. Confocal images were grouped into three categories based on histologic diagnosis: normal, benign, and neoplastic. Images in each category were reviewed to characterize the following features: 1) cell architecture and orientation, 2) nuclear spacing, 3) nuclear size, and 4) intensity of proflavine fluorescence. The confocal image features of each category were compiled into a lexicon by tissue diagnosis (Figure 3-5 and Figure 3-6).

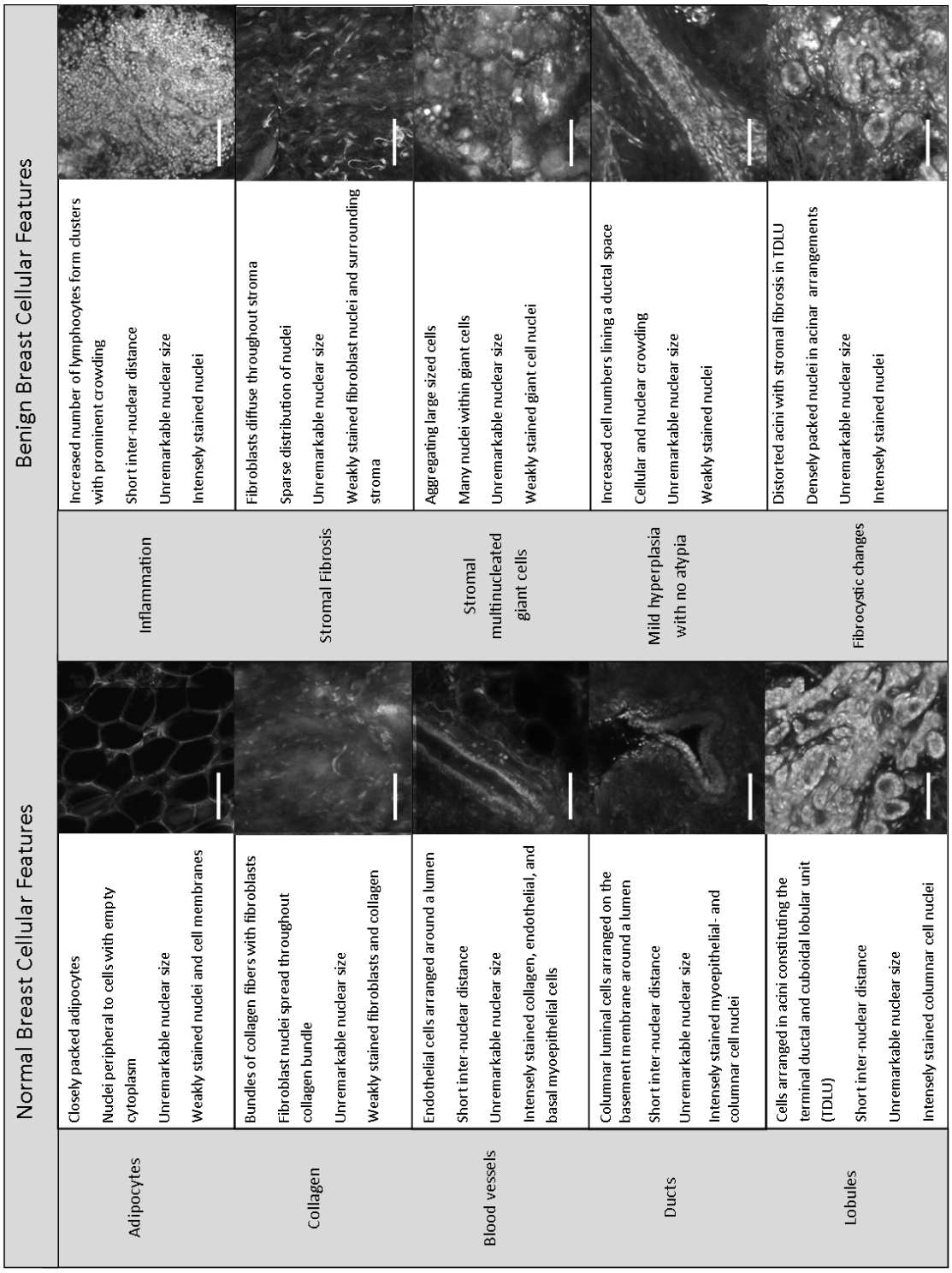

Figure 3-5: Normal and benign breast architectural features imaged by confocal fluorescence microscopy. Normal breast architectural features (left column): adipocytes, collagen, blood vessels, ducts, and lobules. Architectural features of benign changes in the breast tissue (right column): inflammation, stromal fibrosis, stromal multinucleated giant cells, mild hyperplasia with no atypia, and fibrocystic changes. Each feature is described by four criteria, which can be used to aid in interpretation of images acquired with confocal fluorescence microscopy: cell architecture, internuclear distance, nuclear size, and nuclear staining characteristics. Scale bars are 100 μm.

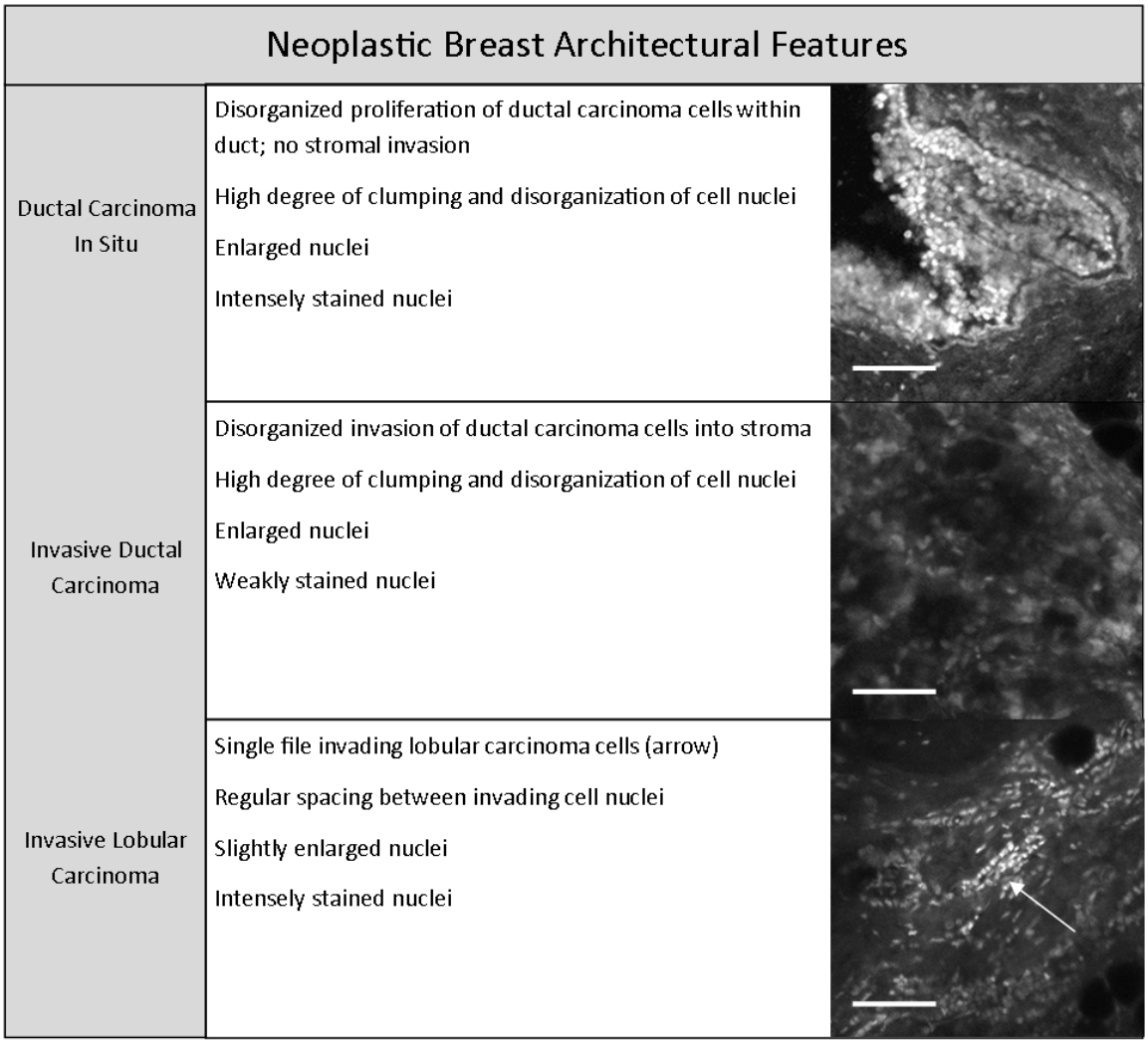

Figure 3-6: Neoplastic breast architectural features imaged by confocal fluorescence microscopy. Neoplastic breast architectural features: ductal carcinoma in situ, invasive ductal carcinoma, and invasive lobular carcinoma. Each feature is described by four criteria which can be used to aid in interpretation of images acquired with confocal fluorescence microscopy: cell architecture, internuclear distance, nuclear size, and nuclear staining characteristics. Scale bars are 100 μm.

Mean fluorescence intensity was measured at ROIs in confocal fluorescence images illustrating non-neoplasia: normal, non-hyperplastic ducts (n=36) and ductal hyperplasia (n=17), and neoplasia: ductal carcinoma *in situ* (n=12) and invasive ductal carcinoma (n=25). To ensure that mean fluorescence intensity was assessed in a representative set of samples, we measured mean fluorescence intensity in ROIs that were included in the training and validation sets and in additional ROIs identified in confocal fluorescence images of specimens summarized in Table

3-1. The histologic diagnosis for all additional ROIs identified in confocal fluorescence images and assessed for mean fluorescence intensity was verified by a dedicated breast pathologist. Figure 3-7 shows the mean fluorescence intensity by diagnostic category. The mean fluorescence intensity reported in Figure 3-7 supports the descriptors provided in Figure 3-5 and Figure 3-6. The mean fluorescence intensity of DCIS (intensely stained nuclei) is higher than IDC, normal ducts, and hyperplastic ducts, all described with weakly stained nuclei. Differences in the mean fluorescence intensity of DCIS are statistically significant when compared to that of IDC ($p = 0.007$) and non-neoplastic ducts ($p = 0.015$). Mean fluorescence intensity values observed in normal ducts (26.6 ± 9.9), ductal hyperplasia (29.3 ± 8.2) and invasive ductal carcinoma (25.9 ± 8.8) were not significantly different ($p > 0.05$).

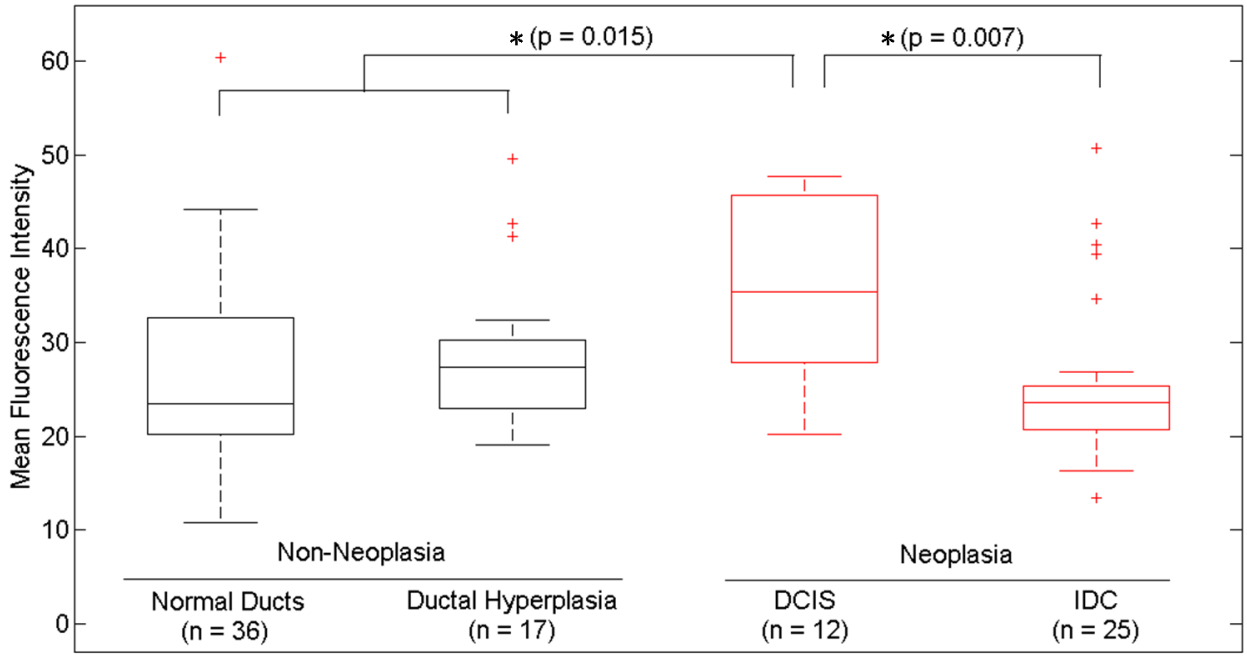

Figure 3-7: Mean fluorescence intensity measured in confocal fluorescence images at ROIs with non-neoplasia: normal, non-hyperplastic ducts (n= 36), ductal hyperplasia (n=17), and neoplasia: ductal carcinoma *in situ* (n=12), and invasive ductal carcinoma (n=25).

Matched confocal and histology images were assembled into a training and validation set to compare the diagnostic performance of confocal fluorescence microscopy and standard histology in distinguishing between neoplastic and non-neoplastic features. Matched pairs of confocal and histology images acquired from 23 sites were used to train readers to review confocal images based on characteristics including morphology, staining, and nuclear size (Figure 3-5 and Figure 3-6). From the remaining images, 98 images of 49 matched ROIs were separated into groups of confocal and histologic images, which were randomly ordered in the validation set. A total of 7 readers, 5 pathologists and 2 cytopathology fellows (Department of Pathology, MDACC), underwent training and reviewed validation images.

Table 3-2 illustrates the results of visual assessment of images acquired by histology with H&E staining (Table 3-2A) and confocal fluorescence microscopy (Table 3-2B). Results are organized based on the rankings assigned to the images in the validation set by each reader and by the true histologic diagnosis for each image as determined by a board-certified breast pathologist. Sensitivity and specificity of evaluation of confocal fluorescence images and conventional histologic images were calculated based on each reader's review of the validation images; neoplasia was classified by a ranking of 4 or 5, non-neoplasia was classified by a ranking of 1-3.

Table 3-2: Results of visual assessment of images in the validation study. The total number of rankings, 343, is based on the rankings assigned by 7 pathologists to each of the 49 images in the validation set. Each validation set included 18 images with histologically normal breast morphology, 10 images that showed morphology with benign changes, and 21 images with neoplastic breast morphology; when the images were ranked by all 7 readers, this resulted in 126 rankings for normal ROIs, 70 rankings for ROIs with benign changes, and 147 rankings for ROIs with neoplasia. False positives were classified as images whose true histologic diagnosis was normal or benign changes, but which were assigned a ranking of 4 or 5. Similarly, false negatives were designated as images with a diagnosis of neoplasia, which were assigned a ranking of 1-3.

A

H&E Images: Visual Assessment by Readers

		Normal	Normal or Benign Changes	Benign Changes	Benign Changes or Neoplasia	Neoplasia	
		1	2	3	4	5	Total
Histologic Diagnosis	Normal	107	3	16	0	0	126
	Benign Changes	14	3	47	6	0	70
	Neoplasia	0	0	11	1	135	147
	Total	121	6	74	7	135	343

B

Confocal Fluorescence Microscopy Images: Visual Assessment by Readers

		Normal	Normal or Benign Changes	Benign Changes	Benign Changes or Neoplasia	Neoplasia	
		1	2	3	4	5	Total
Histologic Diagnosis	Normal	76	2	41	3	4	126
	Benign Changes	17	2	45	1	5	70
	Neoplasia	1	0	10	5	131	147
	Total	94	4	96	9	140	343

Table 3-3 gives a summary of each reader's performance in reviewing images in the validation set. In Figure 3-8, a receiver operator characteristic (ROC) curve shows the averaged performance of all readers in distinguishing neoplastic from non-neoplastic breast cellular features. At the Q-point for the histology ROC curve (square markers, solid line), sensitivity is 93% and specificity is 97% with an area under the ROC curve of 0.987, and at the Q-point for the confocal fluorescence microscopy ROC curve, sensitivity is 93% and specificity is 93% with an area under the ROC curve of 0.957. When accuracy is assessed based on experience level, the readers with more experience in image review (pathologists A-E) have higher accuracy in identifying neoplasia than those with less experience (pathology fellows A and B). Pathologists

and pathology fellows assigned twice the number of false positive rankings in confocal fluorescence images than in H&E images. Readers assigned false negative rankings to the same number of sites in confocal fluorescence and H&E images. In both types of images, DCIS, IDC, and ILC sites were assigned false negative rankings. There were twice as many sites identified as false positives in confocal fluorescence images than in H&E images. More than half of the false positive rankings assigned to confocal fluorescence images were given to sites with normal lobules, however the highest number of false positive rankings was assigned to a single confocal fluorescence image of inflammation (classified incorrectly by 4/7 readers).

Table 3-3: Summary of reader accuracy in distinguishing neoplastic from non-neoplastic breast cellular features in conventional histologic and confocal fluorescence images. When the results are separated based on reader experience in image review, the averaged sensitivity and specificity values are higher for readers with more experience (pathologists A-E) than readers with less experience (pathology fellows A and B). FP = false positive rankings assigned; FN = false negative rankings assigned.

	Histology				Confocal Fluorescence Microscopy			
	FN	FP	Sensitivity	Specificity	FN	FP	Sensitivity	Specificity
Pathologist A	0	1	100%	96%	2	0	90%	100%
Pathologist B	0	2	100%	93%	0	3	100%	89%
Pathologist C	2	1	90%	96%	2	1	90%	96%
Pathologist D	1	0	95%	100%	0	2	100%	93%
Pathologist E	1	0	95%	100%	1	4	95%	86%
Pathology Fellow A	3	1	86%	96%	3	0	86%	100%
Pathology Fellow B	4	1	81%	96%	3	3	86%	89%
All Readers	11	6	93% (±8%)	97% (±2%)	11	13	93% (±5%)	93% (±6%)
Pathologists	4	4	96% (±4%)	97% (±3%)	5	10	95% (±5%)	93% (±8%)
Pathology Fellows	7	2	83%	96%	6	3	86%	95%

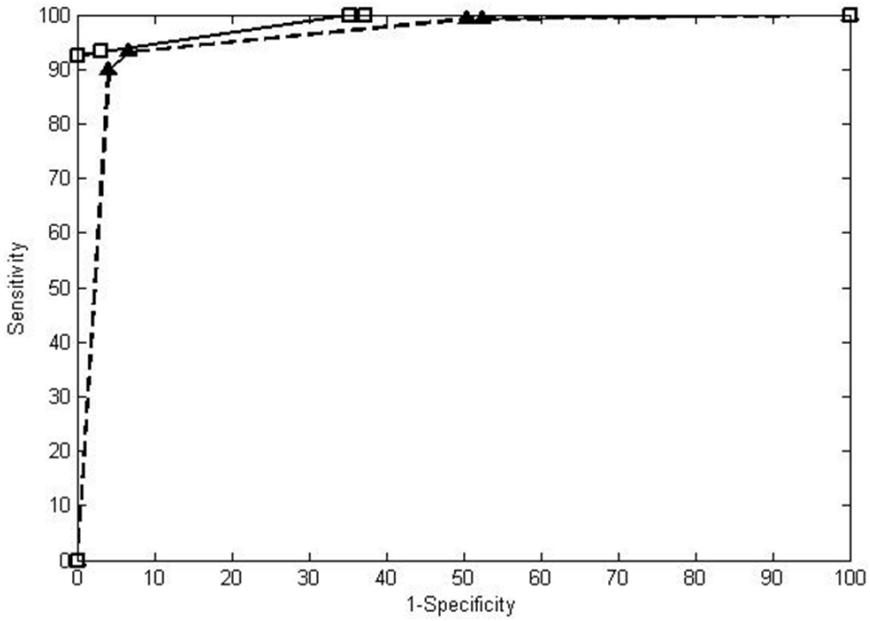

Figure 3-8: Receiver operator characteristic (ROC) curve for the averaged performance of all readers in distinguishing neoplastic from non- neoplastic breast architectural features in conventional histologic (square markers, solid line) and confocal fluorescence images (triangular markers, dashed line). At the Q-point of the ROC curve for histology performance, the sensitivity is 93% and the specificity is 97% with an area under the ROC curve of 0.987. At the Q-point of the ROC curve for confocal fluorescence microscopy performance, the sensitivity is 93% and the specificity is 93% with an area under the ROC curve of 0.957.

We calculated a Kappa score to evaluate inter-rater agreement for visual assessment of H&E and confocal fluorescence images. Since there were 7 raters who assigned rankings to images, we used a formula developed to calculate a Kappa score for multiple ratings per subject [125]. The Kappa score for raters' agreement when ranking H&E images is 0.63 and the Z test statistic is 30.0 ($p<0.001$). When ranking CFM images, inter-rater agreement is characterized by a Kappa score of 0.51 and a Z test statistic of 24.6 ($p<0.001$). Landis and Koch described the ranges of kappa statistic values in intervals of 0.2 from 0 to 1 (where kappa values of 1 and 0 indicate perfect agreement and agreement that could occur by chance, respectively), which are commonly used for kappa statistic interpretation [55, 126-128]. The ranges of kappa statistic values 0.41-0.60 and 0.61-0.80 indicate moderate and substantial agreement strengths, respectively.

3.4 Discussion

The objective of this work was to determine if assessment of breast architecture in confocal fluorescence microscopy images has similar performance to assessment of histologic slides with H&E staining without the need for extensive tissue processing. The findings of this study show that confocal fluorescence images of fresh human breast tissue stained topically using proflavine provide sufficient information to enable discernment of neoplastic and non-neoplastic breast features.

Histology slides are produced through an intricate, time-intensive process. Tissue specimens are fixed through immersion in a chemical fixative to prevent cell autolysis and degradation; adequate tissue fixation takes approximately 24-48 hours. After fixation, tissue specimens are dehydrated through immersion in alcohol to remove excess water and formalin, alcohol is removed from tissue, and specimens are infiltrated with an embedding agent such as paraffin wax. After the wax solidifies, a microtome is used to cut the tissue specimen into 5 μm thick sections. Excess wax is melted off over a few hours, and then a histochemical stain such as hematoxylin and eosin (H&E) is applied. Complete preparation of histologic slides is costly and delays assessment and diagnosis by 1 to 2 days.

Confocal fluorescence microscopy offers a number of important potential advantages as an imaging tool. Sample preparation for confocal fluorescence microscopy is fast and simple. Fresh, unprocessed tissue specimens are stained for 1 minute then washed to remove excess dye. The specimen is then imaged with no further processing and without the need for fixation, embedding, or sectioning. The camera in the microscope is integrated into the system hardware, allowing for image acquisition at near video rate; a 12.2 X 12.2 mm specimen can be imaged using confocal fluorescence microscopy in 10 minutes, and imaging a 4 X 12 mm core needle

biopsy requires less than 2 minutes. Portable confocal microscopes with real-time imaging capability are now commercially available.

A number of other optical imaging modalities have been explored for real-time imaging of breast tissue. Optical coherence tomography (OCT) has been evaluated in several studies for real-time, intraoperative assessment of lymph nodes and breast tumor margins [90, 91, 93], but the resolution of OCT has been too low to provide sufficient detail for rapid tissue assessment. While higher resolution OCT systems are in development, the greater axial resolution of confocal fluorescence microscopy enables resolution of cellular and nuclear features comparable to that of high-magnification (×40) light microscopic images of thin sections. Confocal reflectance microscopy offers resolution similar to that of confocal fluorescence microscopy. Tilli and colleagues showed that acetic acid enhances image detail in confocal reflectance images of mouse mammary and resected human breast tissue, which enabled measurements of nuclear size. Their work demonstrated that near-infrared reflectance confocal microscopy images of mouse mammary and human breast tissue morphology correlate to histologic images with H&E staining [96].

The work described here was performed as a small study to determine the features of neoplastic and non-neoplastic breast tissue that could be assessed at sample acquisition in a routine clinical setting using confocal fluorescence microscopy. All specimens were acquired at a single center, and only a small number of observers participated in image assessment. Further studies are necessary to determine whether confocal fluorescence images contain sufficient detail to enable diagnosis.

If confocal fluorescence images prove adequate for evaluation of breast tissue specimens, this technique could be useful in a number of clinical scenarios. A potentially significant clinical application of this platform is immediate evaluation of the adequacy of tissue core biopsy specimens procured with or without imaging guidance. The current technique of touch preparation of core biopsies does not ensure adequate representation of the targeted lesion for subsequent morphological, phenotypic, and molecular characterization [129]. A second potential application for this technique is rapid assessment of tumor margin status, which could be performed without the necessity for extensive tissue preparation while yielding results comparable to those of frozen section histology. Third, confocal microscopy could be useful to ensure procurement of adequate viable tumor tissue for molecular testing. The ability to image tissue morphology with minimal specimen preparation could be valuable in the era of sophisticated and detailed molecular analysis, including genomic sequencing, for purposes of developing targeted and personalized therapy. Other possible applications for confocal microscopy include assessment of adequate tissue specimens in bio-banking, assistance in identifying desired cell types for use in cell culture, and facilitation in identifying suitable tissue for genomic or proteomic studies. Finally, this technique may be useful to provide histologic diagnosis in low-resource settings where infrastructure for traditional histologic preparation is not available [130].

In conclusion, we present the results of an observational study comparing images acquired with minimal tissue processing using confocal fluorescence microscopy to identify characteristics of a wide range of neoplastic and non-neoplastic breast lesions. Confocal fluorescence microscopy can be performed inexpensively and at near video rate with optimal preservation of the entire tissue for any kind of subsequent analysis. High resolution images

acquired using confocal fluorescence microscopy have micron resolution allowing evaluation of nuclear features and cell morphology, which correlate to those observed in histologic images with H&E staining. In the validation study, image review based on visual assessment shows that confocal fluorescence microscopy and standard histology had similar sensitivity and specificity values for distinguishing between neoplasia and non-neoplasia. The potential utility of this platform for different types of clinical and research applications needs to be tested in larger studies.

4 CHAPTER 4: Confocal fluorescence microscopy for rapid evaluation of invasive tumor cellularity of inflammatory breast carcinoma core needle biopsies[2]

ABSTRACT: Tissue sampling is a problematic issue for inflammatory breast carcinoma, and immediate evaluation following core needle biopsy is needed to evaluate specimen adequacy. We sought to determine if confocal fluorescence microscopy provides sufficient resolution to evaluate specimen adequacy by comparing invasive tumor cellularity estimated from standard histologic images to invasive tumor cellularity estimated from confocal images of breast core needle biopsy specimens. Grayscale confocal fluorescence images of breast core needle biopsy specimens were acquired following proflavine application. A breast-dedicated pathologist evaluated invasive tumor cellularity in histologic images with hematoxylin and eosin staining and in grayscale and false colored confocal images of cores. Agreement between cellularity estimates was quantified using a kappa coefficient. 23 cores from 23 patients with suspected inflammatory breast carcinoma were imaged. Confocal images were acquired in an average of less than 2 minutes per core. Invasive tumor cellularity estimated from histologic and grayscale confocal images showed moderate agreement by kappa coefficient: $\kappa = 0.48 \pm 0.09$ ($p < 0.001$). Grayscale confocal images require less than 2 minutes for acquisition and allow for evaluation of invasive tumor cellularity in breast core needle biopsy specimens with moderate agreement to histologic images. We show that confocal fluorescence microscopy can be performed

[2] The contents of this chapter have been published in the following journal article: Dobbs J, Krishnamurthy S, Kyrish M, Benveniste AP, Yang W, Richards-Kortum R. Confocal fluorescence microscopy for rapid evaluation of invasive tumor cellularity of inflammatory breast carcinoma core needle biopsies. Breast Cancer Res Treat 2015; 149(1):303-10.

immediately following specimen acquisition and could indicate the need for additional biopsies at the initial visit.

4.1 Introduction

Inflammatory breast carcinoma (IBC) is a rare, aggressive type of breast cancer that is characterized clinically by tenderness, erythema, and edema involving at least one third of the entire breast [1, 123, 131, 132]. This variant of breast cancer can be clinically mistaken for mastitis and treated with antibiotics resulting in delay in the recognition of malignancy. The redness and edema of the breast is attributed to the frequent involvement of the lymphovascular channels in the breast. Pathologic diagnosis can be made using skin punch biopsy and / or core needle biopsy (CNB) of the affected breast. The presence of lymphovascular tumor emboli in the skin biopsy and invasive mammary carcinoma in the core biopsy can establish the diagnosis and initiate the clinical management of the patients. Tissue sampling can be a particularly problematic issue in IBC, since most cases present with no discrete mass and therefore accurate targeting of the area of breast for image-guided CNBs can be difficult [133, 134]. Shah and colleagues showed that sampling error can lead to inadequate CNB specimens, which have an insufficient amount of tissue to make a diagnosis, in as many as 9.1% of cases [135]. In cases with sampling error, several more days are required to perform repeated biopsies and histologic assessment for additional tissue specimens [135, 136]. Immediate evaluation of CNBs for assessment of tumor cellularity can be extremely valuable to ensure procurement of adequate tissue not just for diagnosis of the invasive carcinoma but also for ancillary studies in one setting. Touch preparation and frozen section are the currently available techniques for rapid evaluation of breast CNB specimen adequacy. While touch preparation of breast CNBs can be useful to ascertain the presence or absence of tumor cells in the CNBs, it cannot indicate the extent of

tumor cellularity in the CNB and whether the malignancy is *in situ*, invasive, or both. In addition, the process of touching and rolling the CNBs on the glass slides may cause distortion, which makes them less than optimal for accurate histopathological examination. Frozen section is generally not preferred for immediate assessment of CNBs because of loss of the precious tissue during the cutting process. A technique is needed to evaluate the adequacy of IBC CNB specimens as soon as they are procured in a clinical setting, without tissue preparation that may compromise the quality of the core. The technique should be able to immediately indicate to the radiologist if the area of interest has been accurately targeted, and if additional biopsies are required [135].

Several studies have established the utility of confocal microscopy for breast tissue assessment [1, 96, 120, 121, 137]. Schiffhauer and colleagues demonstrated the feasibility of confocal reflectance microscopy for identifying the presence of neoplasia in unfixed breast CNB specimens in real time [121]. We recently showed that confocal fluorescence microscopy can be performed in a clinical setting to acquire images of fresh breast tissue with sufficient resolution to identify neoplastic and non-neoplastic breast cytomorphological and architectural features [1].

The objective of this work was to determine the feasibility of using confocal fluorescence microscopy in a clinical setting to evaluate the adequacy of IBC CNB specimens by estimating the amount of invasive tumor cellularity in each specimen. To meet this objective, we performed a proof of concept study to estimate invasive tumor cellularity from grayscale confocal images and confocal images that were false colored to mimic histologic staining; results were compared to the assessment from the gold standard of histologic images obtained from conventional light microscopic examination of formalin fixed and paraffin embedded tissue sections of the core biopsies stained by hematoxylin and eosin.

4.2 Materials and Methods

Core needle biopsy specimens were obtained from patients with clinical signs and symptoms of IBC. The protocol for tissue acquisition was reviewed and approved by the Institutional Review Boards at The University of Texas MD Anderson Cancer Center and Rice University. Ultrasound-guided CNBs were performed per standard clinical protocol. Single cores were prepared for confocal imaging within 5 minutes of the core needle biopsy procedure; each core was typically 1 x 4 x 12 mm^3 in size. Cores were kept moist in phosphate buffered saline (PBS) (pH = 7.4) prior to imaging. A solution of 0.01% proflavine in sterile PBS was applied topically to the core for approximately 1 minute; proflavine is a fluorescent dye that preferentially stains nuclei in confocal fluorescence images [100, 102, 122, 138].

The procedure for imaging cores with confocal fluorescence microscopy has been described previously [1]. Prior to imaging, a core was positioned on the microscope stage. Each core was imaged using a scanning confocal microscope (Vivascope 2500®; Caliber Imaging and Diagnostics Inc., Rochester, New York) at 488 nm excitation with a 550 ± 44 nm bandpass filter with a 30x water immersion lens (numerical aperture = 0.8). At the center of the 750 x 750 μm^2 region of interest (ROI), lateral resolution of the confocal microscope is 1.0 μm and axial resolution is 5.0 μm. Initially, illumination power was set to 2.1 mW (± 0.4 mW) and adjusted to maximize signal and avoid saturation. To create a composite image of the core at a single axial depth, the microscope stage was scanned in a grid pattern (maximum area: 12.2 x 12.2 mm^2); composite images of cores were typically 4 x 12.2 mm^2. After imaging, the cores were stored in PBS and submitted to the IBC tissue registry for processing, including standard histologic preparation, fixation, and staining with hematoxylin and eosin (H&E).

Grayscale fluorescence images of cores were acquired with the confocal microscope. The grayscale confocal fluorescence images were false colored to resemble histologic staining by combining the experimentally-determined color values for hematoxylin and eosin reported by Gareau [139] into a single set of color values: H = [1.3 0.75 1.88], where [red (k=1) green (k=2) and blue (k=3)]. False color was applied to each pixel of confocal images (C) as follows:

$$C_{x,y,k} = 1 - F_{x,y}(2 - H_k)$$

where F is the grayscale confocal fluorescence image with each pixel normalized to the maximum [139]. The individual grayscale confocal images were automatically stitched together immediately following acquisition by the confocal microscope to form a composite grayscale image of each core. False colored confocal images were manually stitched together, using the grayscale confocal image as a guide, to form a composite false colored image of each core.

A board-certified, dedicated breast pathologist (author S. Krishnamurthy) assessed H&E-stained slides with a 10X objective lens and evaluated confocal images at comparable magnification. Invasive tumor cellularity was estimated in three images for each core: one histologic image prepared with standard fixation in neutral buffered formalin, routinely processed, embedded in paraffin followed by H&E staining, one composite grayscale confocal image, and one false colored confocal image - using standard histologic criteria [15]. Tumor cellularity was defined as the percentage of the core comprised of invasive breast carcinoma [140].

A kappa coefficient was calculated for each combination of confocal and histologic image types (histologic vs. grayscale confocal images and histologic vs. false colored confocal images), in order to compare the agreement between invasive tumor cellularity estimated from

histologic, grayscale confocal, and false colored confocal images. In this calculation of inter-rater agreement, each image type was considered to be one "rater".

4.3 Results

A total of 23 cores were collected from 23 patients with untreated, clinically suspected IBC [123] (Table 4-1). Twenty of the cores contained neoplastic tissue, identified by standard histologic criteria in histologic images. The average time to acquire a composite confocal image was 1 minute, 54 seconds (Table 4-1). False coloring produced confocal images that visually resembled tissue sections stained with hematoxylin and eosin.

Table 4-1: Percent invasive tumor cellularity in IBC cores estimated in histologic, grayscale confocal, and false colored confocal images. Histologic slides were stained with hematoxylin and eosin (H&E). Imaging time indicates the time to acquire a composite grayscale confocal image. The average imaging time was 01:54 mm:ss.

Adequacy for Tumor Diagnosis	Core #	Estimated Invasive Tumor Cellularity in Images of Core Needle Biopsy Specimens			Imaging Time (MM:SS)	Histologic IBC type	Tumor grade
		Histology (H&E*)	Confocal (Grayscale)	Confocal (False Coloring)			
Adequate	1	90%	75-80%	80%	00:53	Invasive ductal carcinoma	2
	2	5%	5%	5%	00:53	Invasive ductal carcinoma with mucinous carcinoma	3
	3	10%	25%	20%	02:41	Invasive ductal carcinoma	3
	4	20%	5%	20%	01:47	Invasive ductal carcinoma	2
	5	75%	75%	20%	02:51	Invasive ductal carcinoma	3
	6	25%	20%	20%	02:07	Invasive ductal carcinoma	3
	7	20%	20%	20%	02:54	Invasive ductal carcinoma	3
	8	100%	100%	30%	02:51	Invasive ductal carcinoma	3
	9	5%	5-10%	5%	02:51	Invasive ductal carcinoma	3
	10	25-30%	25%	40%	01:46	Invasive ductal carcinoma	2
	11	95%	80-95%	90%	02:33	Invasive ductal carcinoma	3
	12	30%	30%	30%	02:09	Invasive ductal carcinoma	3
	13	30%	20%	50%	01:01	Invasive ductal carcinoma	3
	14	95%	70%	90%	01:04	Invasive ductal carcinoma	3
	15	80%	75%	90%	01:04	Invasive ductal carcinoma with micropapillary features	2
	16	70%	90-95%	95%	01:04	Invasive ductal carcinoma	3
	17	20%	10%	10%	01:04	Invasive ductal and lobular carcinoma	1
	18	50%	10-15%	15%	02:51	Invasive lobular carcinoma	3
	19	25%	30%	25%	01:47	Invasive ductal carcinoma	2
	20	30-40%	40%	20%	01:25	Invasive ductal carcinoma	3
Inadequate	21	0%	0%	5%	02:51	Invasive ductal carcinoma	3
	22	0%	0%	0%	01:04	Invasive ductal carcinoma	3
	23	0%	0%	0%	01:47	Invasive ductal carcinoma	2

Representative histologic, grayscale confocal, and false colored confocal images of cores that contain IBC tissue are shown in Figure 4-1 and Figure 4-2. Figure 4-1 shows a core that contains both neoplastic and non-neoplastic tissue, with an estimated 25% cellularity in the histologic image; cellularity was estimated as 30% and 25% in grayscale confocal and false

colored confocal images, respectively. Figure 4-2 shows a core with 80% cellularity estimated in the histologic image, 75% cellularity estimated in the grayscale confocal image, and 90% cellularity estimated in the false colored confocal image.

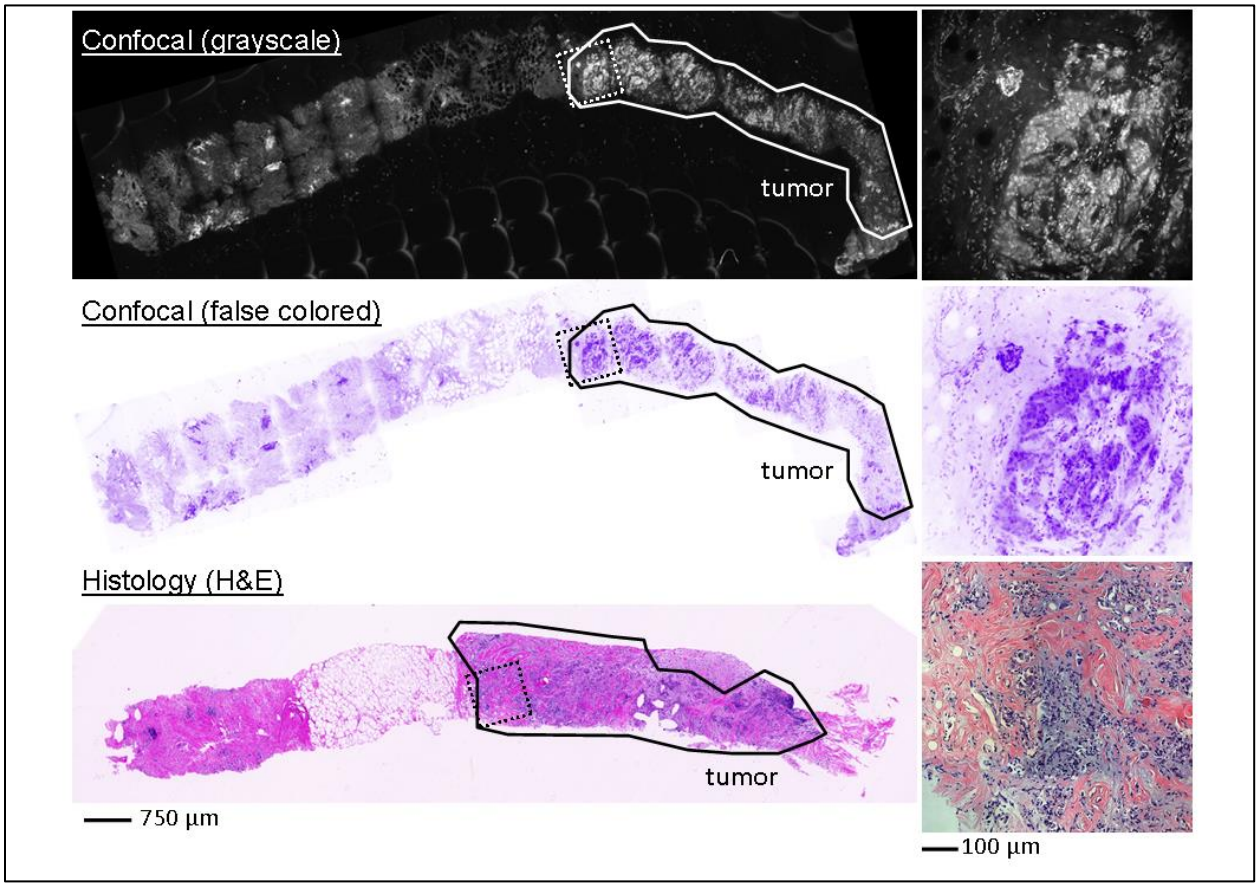

Figure 4-1: Representative core with invasive tumor and non-neoplastic tissue (core 19); 25% cellularity estimated by author S.K. in histologic image (standard H&E staining), 30% cellularity estimated in grayscale confocal fluorescence image (0.01% proflavine staining), 25% cellularity estimated in false colored confocal fluorescence image derived from grayscale image (0.01% proflavine staining). The solid outlined region indicates areas of the CNB specimen that contain invasive tumor. The scale bar at left is 750 µm. The insets at right show the border between neoplastic and non-neoplastic tissue in the CNB specimen. The locations of the insets are indicated in each core by a square with dashed lines. The scale bar at right is 100 µm.

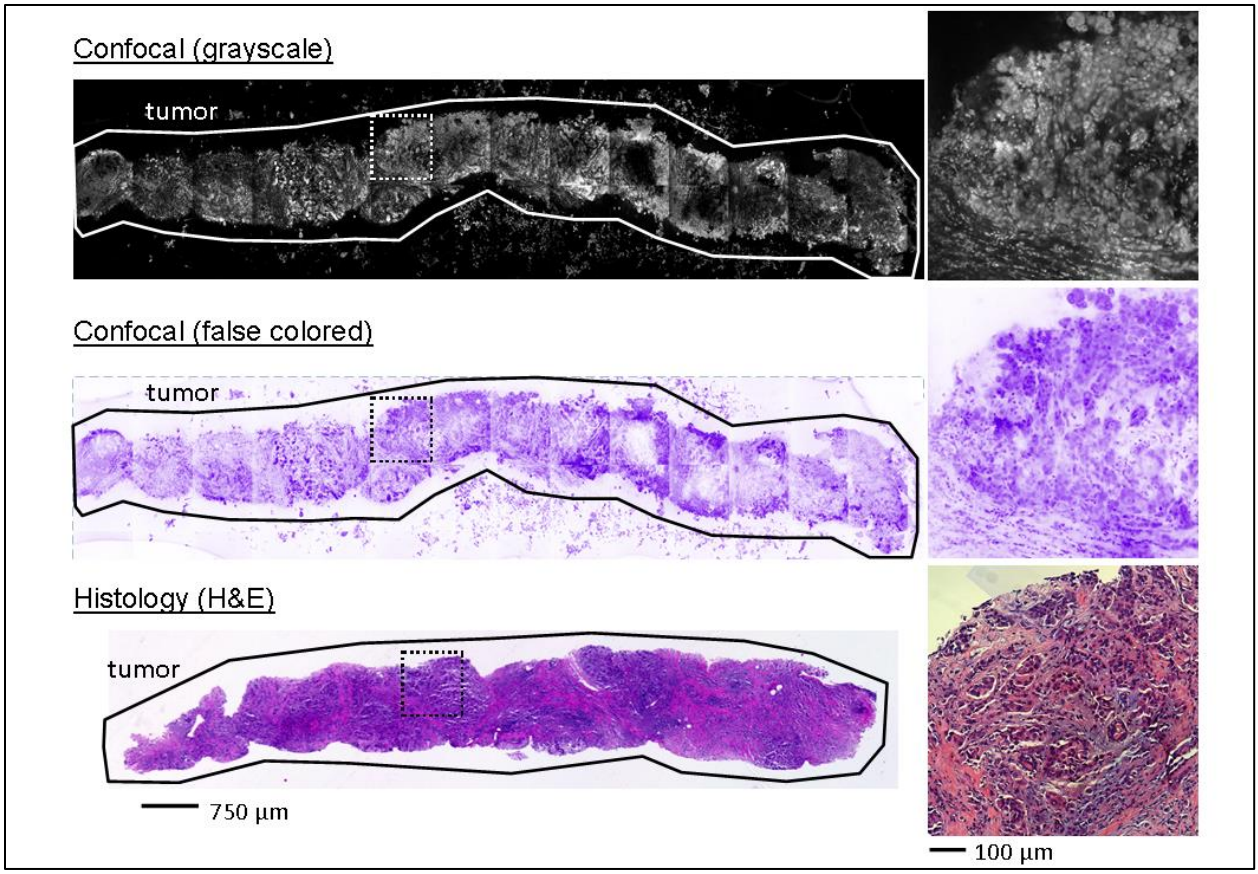

Figure 4-2: Representative core with invasive tumor (core 15); 80% cellularity estimated by author S.K. in histologic image (standard H&E staining), 75% cellularity estimated in grayscale confocal fluorescence image (0.01% proflavine staining), 90% cellularity estimated in false colored confocal fluorescence image derived from grayscale image (0.01% proflavine staining). The solid outlined region indicates areas of the CNB specimen that contain neoplastic tissue. The scale bar at left is 750 µm. The insets at right show a region of neoplastic tissue in the CNB specimen. The locations of the insets are indicated in each core by a square with dashed lines. The scale bar at right is 100 µm.

Three cores acquired from patients diagnosed with IBC were considered to be inadequate as a result of sampling error; the histologic image contained no neoplastic tissue despite a clinical diagnosis of IBC. Representative images of an inadequate core consisting of adipose tissue and no neoplastic tissue, based on assessment of the histologic image, are shown in Figure 4-3. All three images of the core estimated cellularity as 0%.

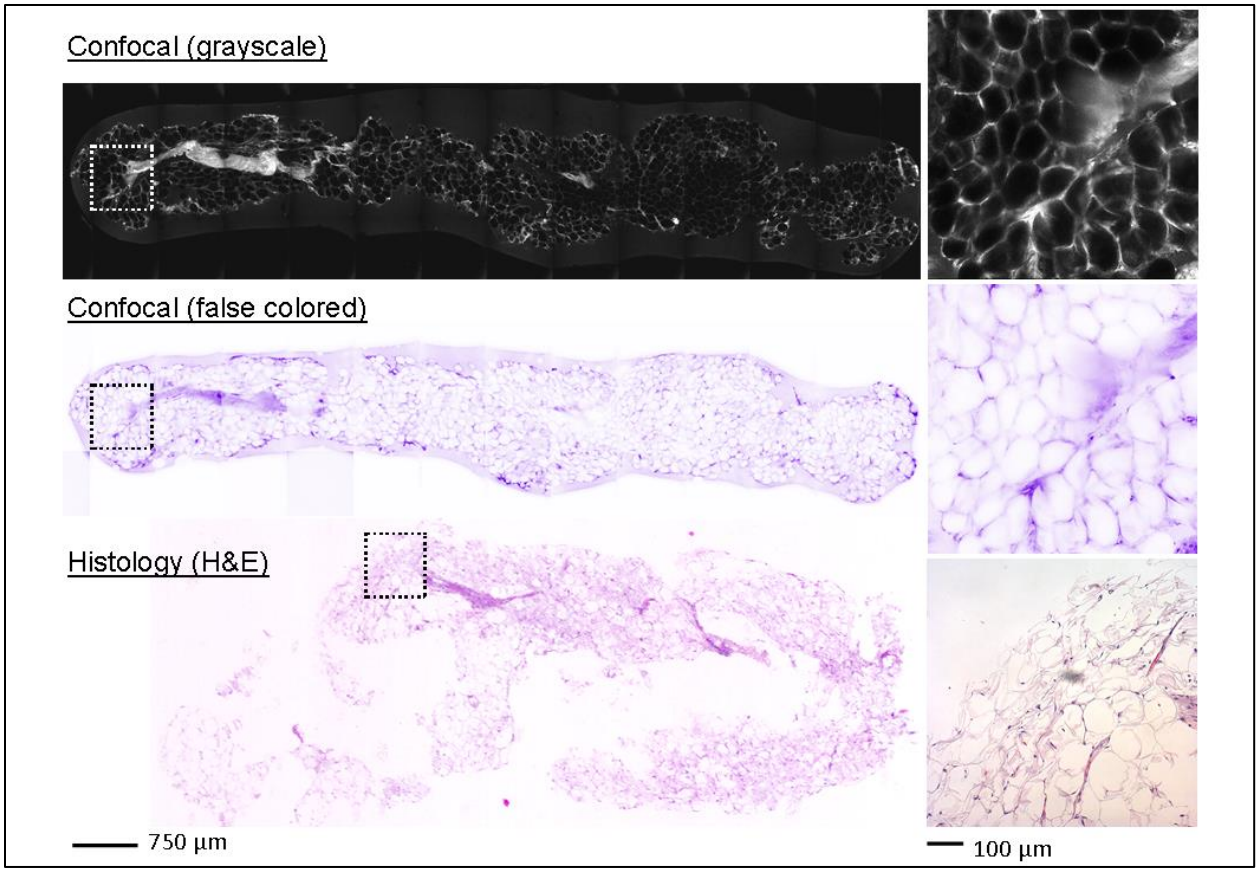

Figure 4-3: Representative core with no invasive tumor (core 22); 0% cellularity estimated by author S.K. in histologic image (standard H&E staining), 0% cellularity estimated in grayscale confocal fluorescence image (0.01% proflavine staining), 0% cellularity estimated in false colored confocal fluorescence image derived from grayscale image (0.01% proflavine staining). This core is considered inadequate due to sampling error; no invasive tumor is visible despite a clinical indication of IBC. The scale bar at left is 750 µm. The insets at right show a region of non-neoplastic tissue in the CNB specimen. The locations of the insets are indicated in each core by a square with dashed lines. The scale bar at right is 100 µm.

Estimates of tumor cellularity based on histologic, grayscale confocal, and false colored confocal images for all specimens are summarized in **Error! Reference source not found.**. Figure 4-4 illustrates the agreement between tumor cellularity estimated in histologic and grayscale confocal images (Figure 4-4A) and in histologic and false colored confocal images (Figure 4-4B). Each data point represents a core needle biopsy specimen from which tumor cellularity was estimated. Dashed lines indicate the linear fit for each set of data points and Pearson coefficient (R^2) values quantify the linear fit of the data. Tumor cellularity estimates

were more consistent between histologic and grayscale confocal images ($R^2 = 0.88$) than between histologic and false colored confocal images ($R^2 = 0.61$).

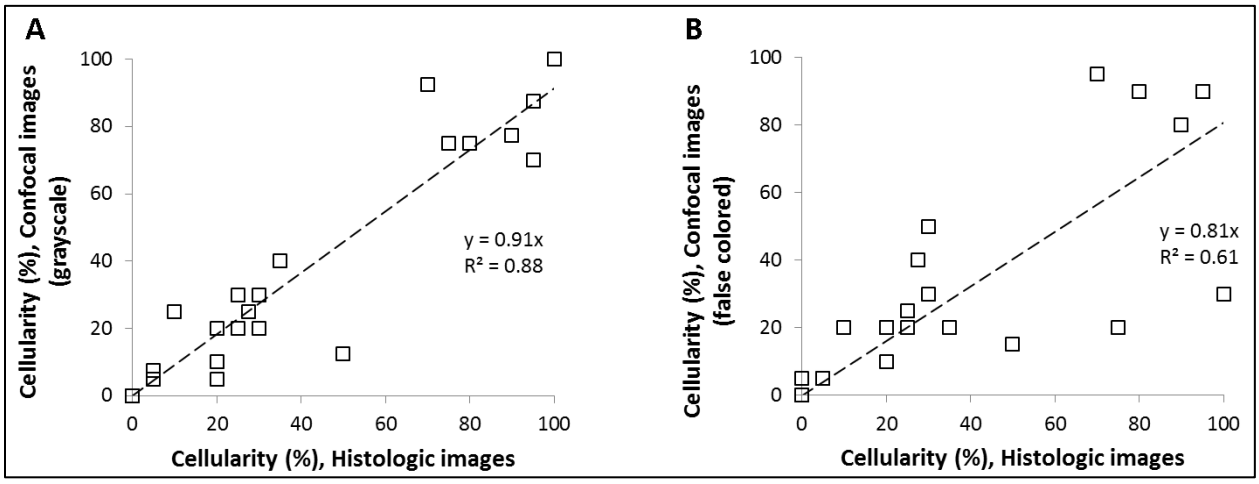

Figure 4-4: Scatterplots illustrating agreement on estimated invasive tumor cellularity between image types. Each data point represents a CNB specimen. Dashed lines represent the linear fit of the data. Pearson coefficients (R^2) quantify the linear fit of invasive tumor cellularity data. A: Invasive tumor cellularity estimates from grayscale confocal images and histologic images. B: Invasive tumor cellularity estimates from false colored confocal images and histologic images.

A kappa coefficient was calculated [125, 141] to quantify the agreement between histologic images and either grayscale or false colored images. Standard error and *p* values for kappa were also quantified (Table 4-2). The kappa value calculated for agreement between histologic and grayscale confocal images indicate moderate agreement based on defined categories for kappa values [126, 141]; $\kappa = 0.48 \pm 0.09$ ($p < 0.001$). Agreement between histologic and false colored confocal images was fair and not statistically significant; $\kappa = 0.28 \pm 0.26$ ($p = 0.14$).

Table 4-2: Inter-rater agreement of estimated invasive tumor cellularity between the types of images, quantified by the kappa coefficient and standard error [125]. Level of agreement is based on categories described by Viera and Garrett [141]. P value was calculated using a normal distribution.

Image types	Interrater Agreement – Two Techniques			
	Kappa Coefficient	Standard Error	Level of Agreement	*P* value
Histologic vs. Grayscale Confocal	0.477	0.088	Moderate	3.43E-08
Histologic vs. False Colored Confocal	0.280	0.258	Fair	0.139

4.4 Discussion

The objective of this work was to determine the feasibility of using confocal fluorescence microscopy for immediate assessment of invasive tumor cellularity of CNBs in patients with IBC. Composite grayscale confocal images of CNB specimens were acquired in an average time of 2 minutes. Statistical analysis shows that there is moderate agreement between tumor cellularity estimated from histologic images and grayscale confocal images. False coloring the confocal images using a single analog for histologic staining does not improve agreement. These findings demonstrate that confocal fluorescence microscopy could be used to assess adequacy of IBC CNB specimens. This technique may be useful to ensure procurement of high quality CNBs not only for routine histopathological diagnosis but also for ancillary studies including immunohistochemistry and molecular testing.

Of the 3 CNB specimens that were determined to be inadequate by histologic assessment, one had benign lobules and fibrous tissue (core #21) and two consisted completely of adipose tissue (cores #22, 23). These cores were identified as inadequate based on tumor cellularity estimated as 0-5% in histologic, grayscale confocal, and false colored confocal images (Table 4-1). Of the 20 CNB specimens that were determined to be adequate by histologic assessment, 20 were diagnosed as invasive carcinoma; morphological features of invasive carcinoma were also

recognized in grayscale confocal and false colored confocal images. One CNB specimen was diagnosed as mucinous carcinoma (core #2) based on standard histologic criteria [15] and was also recognized as such on the confocal images.

IBC is an aggressive type of breast cancer, which is known to metastasize through the lymphatic system and typically presents as a non-palpable lesion [123, 131, 132]. To obtain a rapid and accurate diagnosis of IBC, there must be a reliable method to sample tissue. Although inter-rater agreement is typically high for histologic diagnosis [142-145], the rate of inadequate samples is a limitation of CNB as a sampling technique for breast cancer diagnosis [135, 136, 142, 143, 146]. Shah and colleagues showed that the rate of sampling error leading to inadequate CNB specimens can be as high as 9.1% [135]. Therefore, there is a need for a technique that can evaluate specimen adequacy [135] with a relatively high sensitivity and specificity.

Previous studies have illustrated the feasibility of evaluating breast tissue specimens with confocal microscopy [1, 96, 120, 121, 137]. Schiffhauer and colleagues evaluated confocal reflectance microscopy for screening unfixed breast CNB specimens with a range of neoplastic and non-neoplastic histologic features. Their study showed that there were adequate morphologic and cellular features in confocal reflectance images to allow correlation to histologic images [121]. In this study, we chose to focus on inflammatory breast cancer, because we wanted to determine if assessment of confocal fluorescence microscopy images of fresh cores would show which cores had insufficient tumor tissue for diagnosis and therefore identify cases for which a repeat biopsy was needed. Our previous work showed that confocal fluorescence microscopy images provide sufficient detail to distinguish between neoplastic such as ductal carcinoma in situ and invasive ductal and lobular carcinoma and non-neoplastic breast features, including benign ducts, lobules, and hyperplasia [1]. We characterized inter-rater agreement between

pathologists who assessed confocal fluorescence with a kappa coefficient for multiple ratings per subject. The kappa coefficient described in our previous work (0.51, $p < 0.001$) between pathologists assessing confocal images indicated moderate agreement based on defined categories of kappa coefficients [126, 141]. This level of agreement is similar to the moderate agreement between a single rater's assessment of grayscale confocal and histologic images shown in Table 4-2 (0.477, $p < 0.001$). The findings of these two studies suggest that confocal fluorescence images could potentially be used to assess adequacy of breast core needle biopsies with many histologic features.

False coloring to mimic histologic staining in confocal images of breast tissue has been demonstrated in two studies [139, 147]. Gareau showed that the false coloring technique using confocal reflectance and fluorescence microscopy to mimic hematoxylin and eosin staining, respectively, produced multimodal confocal images mimicking the appearance of corresponding histologic images [139]. Bini and colleagues used false coloring for tissue obtained from Mohs skin excisions and demonstrated correlation between confocal mosaics and histologic images [147]. Previous studies showed that false coloring improved correlation between confocal and histologic images [126, 141]. However, in contrast to the previous studies which used both reflectance and fluorescence images to mimic hematoxylin and eosin staining, we used only fluorescence images to mimic histologic staining of the tissue section. It was not possible to use multimodal confocal images because reflectance images were not collected for every CNB specimen, and because some confocal reflectance images were not aligned laterally or axially with the confocal fluorescence images of the corresponding core needle biopsy specimen.

In conclusion, we present the results of a proof of concept study comparing estimated invasive tumor cellularity between grayscale confocal, false colored confocal, and histologic

images of 23 IBC CNB specimens. Grayscale confocal images require an average of only 2 minutes for acquisition and allow immediate evaluation of invasive tumor cellularity in IBC CNB specimens; agreement with histologic images is moderate. We show that confocal fluorescence microscopy could be used for immediate assessment of CNB specimen adequacy, so that additional biopsies for diagnosis, bio-banking, or genetic sequencing studies can be performed on site without need for a repeat visit. Additional larger prospective studies are warranted to validate our findings for the potential utilization of confocal fluorescence microscopy in routine pathology practice as a robust technique for immediate assessment of specimen adequacy of IBC CNBs.

5 CHAPTER 5: Confocal fluorescence microscopy compared to histologic slides for breast cancer diagnosis and grading

ABSTRACT: Histologic assessment is the current standard for diagnosis of breast cancer. Optical imaging techniques are evolving which allow rapid examination of tissues without extensive preparation or loss of tissue. We performed a preliminary study to evaluate the potential of assigning diagnosis and grade to images of breast tumors acquired with confocal fluorescence microscopy. A total of 30 breast tissue specimens were acquired from 30 patients, stained with proflavine and imaged with a confocal fluorescence microscope. The tissues were then fixed in formalin and routinely processed to generate tissue sections, which were stained with hematoxylin and eosin. An expert pathologist performed two reviews of all confocal and histologic images and assigned a diagnosis and grade to each. Overall, 29 of 30 specimens were correctly classified as neoplasia in confocal images. Diagnosis and grade assigned to confocal and histologic images agreed for 24/30 specimens and 21/30 specimens, respectively. The kappa coefficient to characterize agreement between two reviews of histologic images was perfect for assignment of diagnosis ($\kappa = 1.00 \pm 0.15$) and substantial for tumor grade ($\kappa = 0.75 \pm 0.18$). Agreement between two reviews of confocal images was fair for assignment of both diagnosis and grade ($\kappa = 0.36 \pm 0.14$ and $\kappa = 0.30 \pm 0.15$, respectively). These findings indicate that confocal microscopy has potential as a technique for rapid diagnosis of breast tissue, but improved lateral resolution and additional contrast agents targeting markers associated with tumor type and grade may be needed to improve breast cancer diagnosis and grading.

5.1 Introduction

The standard of care for the evaluation of breast tissues procured by image-guided biopsies or surgical excision is conventional cytopathological and histopathological examination. Immediate assessment of tissue procured by fine needle aspiration biopsy and core needle biopsy can be performed by cytopathological examination of aspirated smears [113, 133, 144, 148] or touch preparation of the needle cores [113, 134, 142, 144, 149-151]. While touch preparation can be used for immediate evaluation of core needle biopsies or larger tissue specimens acquired from surgical resections, the lack of availability of tissue architecture can lower the sensitivity and specificity of interpretation with this technique [133, 144]. The most commonly used procedure for the intraoperative assessment of tissues obtained by surgical resections in pathology laboratories is frozen section analysis [152-154]. Frozen section analysis entails embedding the tissue in a mounting medium such as optimal cutting medium to create frozen tissue blocks that are sectioned in a cryotome to generate 5 μm thick frozen tissue sections, which are fixed in alcohol, stained by hematoxylin and eosin (H&E), and immediately interpreted by a pathologist. The technique of rapidly freezing, cutting and staining the tissue allows rapid evaluation of the tissue, but is associated with limitations, such as loss of tissue in the cryostat while preparing the tissue, introduction of freezing artifacts, and difficulty in cutting tissues that contain adipose tissue or bone [113, 155].

In light of these limitations, several imaging techniques to rapidly assess breast tissue specimens are being investigated, including optical coherence tomography (OCT), radiofrequency spectroscopy, and high-frequency ultrasound [91, 93, 94, 156]. A recent study by Zysk et al. reported on the use of a handheld OCT probe to evaluate surgical margins following breast-conserving surgery. Their findings indicate that intraoperative assessment with OCT could

potentially reduce the rate of reoperations following breast-conserving surgery by identifying positive tumor margins at the point-of-care [94].

Confocal microscopy is a high resolution optical imaging technique that has been evaluated in several studies for its potential role in rapid breast tissue assessment. A previous study demonstrated that confocal images of fresh, surgically excised breast tissue contain sufficient detail to identify neoplasia with comparable accuracy to histologic assessment [1]. Other studies assessed the potential of using confocal fluorescence microscopy to evaluate core needle biopsy specimens [121] and assess their adequacy based on estimated tumor cellularity [2]. However, previous studies have not shown whether images acquired with confocal microscopy contain sufficient detail to make a primary diagnosis of the tissue including categorization of the tissue as benign or malignant and for assessing the type and grade of malignant tumors.

In this preliminary study, our objective was to compare the diagnosis of breast masses made using confocal fluorescence images with conventional histopathological examination of the same tissue. We investigated utilization of confocal fluorescence images for initial categorization of the breast mass as benign or malignant, subsequent classification of the latter category of tumors as carcinoma in situ or as invasive carcinoma, and grading of the tumors.

5.2 Materials and Methods

Human breast tissue specimens were acquired through a protocol approved by the institutional review boards at the University of Texas M.D. Anderson Cancer Center and Rice University. Patients were eligible to participate in the study if they provided informed consent and were undergoing primary surgical resection for the management of biopsy-proven breast cancer. Breast tissue specimens measuring approximately 15 x 15 x 8 mm were sampled from

the area of interest in the surgical specimen within 30 minutes of resection. Prior to imaging, all breast tissue specimens were stained with proflavine, a fluorescent contrast agent that stains cell nuclei in optical images [1, 102, 122], which was topically applied as a 0.01% solution in 1x phosphate-buffered saline (PBS) for 1 minute followed by a wash with 1x PBS.

Confocal fluorescence images were acquired from all breast specimens using a scanning confocal microscope (Vivascope 2500®; Caliber Imaging and Diagnostics Inc., Rochester, New York) as described previously [2-4]. The proflavine-stained breast tissue specimen was positioned on the confocal microscope stage and imaged at 2.1 ± 0.4 mW at 488 nm laser excitation with a 550 ± 44 nm bandpass filter through a 30X water immersion lens (numerical aperture, N.A. = 0.8). At the center of each 750 x 750 μm confocal field of view, the lateral resolution is 2.0 μm and axial resolution is 5.0 μm, as reported by the manufacturer. The microscope acquired images in a grid pattern and images were assembled into a 12.2 x 12.2 mm composite image. After image acquisition, breast tissue specimens were submitted for standard fixation in 10% neutral buffered formalin, processing, embedding in paraffin wax and cut to generate 5 μm tissue sections which were stained by hematoxylin and eosin (H&E).

Composite confocal images and histologic slides were reviewed in random order by a board-certified breast pathologist (author S.K.) who was blinded to patient identification and the surgical pathology accession number. Histologic images of approximately 5 -10 μm thick tissue sections were reviewed on a light microscope (Olympus) at 10X (N.A. = 0.25), 20X (N.A. = 0.40), and 40X (N.A. = 0.65), and evaluated using conventional histopathological criteria for categorization of the breast masses as benign or malignant. Malignant tumors were classified as carcinoma in situ or invasive carcinoma, which were further categorized as ductal or lobular in phenotype. Invasive tumors were graded based on the Nottingham histologic grading system as

low, intermediate and high [15]. Ductal carcinoma in situ was graded based on nuclear size as low, intermediate, or high grade.

All confocal images were reviewed by viewing on a computer monitor at low magnification (5X) to view the entire specimen and at higher magnification (30X). The theoretical lateral resolution at the settings used for visualizing the confocal images, assuming a wavelength of 550 nm, was 1.1 μm, 0.7 μm, and 0.45 μm, respectively. Since confocal images have lower lateral resolution than standard histologic slides, it was not possible to identify some features commonly used to assign tumor grade in H&E sections, such as mitotic figures and presence of nucleoli, in confocal images. Thus, confocal images were visually assessed and invasive tumor was graded based on modified criteria taking into consideration nuclear size, nuclear pleomorphism and gland formation by the tumor cells comprising the invasive tumor [1]. Invasive tumors with gland formation in >75% of the tumor with low to intermediate sized nuclei were graded as low grade and those with absence of glands, large nuclear size with nuclear pleomorphism were graded as high grade. Tumors with features in between these characteristics were categorized as intermediate in grade.

Each confocal and histologic image was reviewed twice, during separate sessions in which the reviewing pathologist assigned a diagnosis and tumor grade to each confocal and histologic image. Diagnoses assigned to specimens included ductal carcinoma *in situ* (DCIS), invasive ductal carcinoma (IDC), invasive lobular carcinoma (ILC), and "negative for tumor." For the purposes of data analysis we categorized ductal carcinoma *in situ* and invasive tumors as either low and intermediate grade or high grade. Diagnoses and grades assigned to confocal images were compared to those assigned during review of the corresponding histologic images. A kappa coefficient [125, 126, 141] was calculated to quantify the agreement between tumor

diagnosis and grade assigned in the first and second reviews of confocal images and histologic images. In this calculation, each review of either confocal or histologic images was considered to be one "rater." Standard error was estimated for each kappa coefficient. The critical ratio, *z*, the ratio between each kappa coefficient and the estimated value of standard error, was calculated for each kappa coefficient. A *p* value was estimated by referring the critical ratio to tables of the standard normal distribution in order to test the hypothesis that each kappa coefficient was significantly larger than zero [125, 126].

5.3 Results

A total of 30 tissue specimens collected from breast tumor masses were imaged to obtain gray scale images using confocal fluorescence microscope after staining with proflavine. Hematoxylin and eosin stained tissue sections of the same tissue were available for conventional histopathologic examination.

Figure 5-1 illustrates representative confocal and histologic images of breast tissue specimens, which were assigned the same diagnosis and grade in confocal images and on histologic examination. The top row (Figure 5-1: A-D) shows a lesion identified as low/intermediate grade DCIS in the corresponding histologic slide and confocal image based on the presence of ductal spaces filled with cells with enlarged nuclei, and no visible stromal invasion. The middle row (Figure 5-1: E-H) shows a lesion identified as low/intermediate grade IDC based on the presence of enlarged nuclei with moderate pleomorphism, disorganized proliferation invading into stromal tissue, and widespread gland formation. The bottom row (Figure 5-1: I-L) shows a lesion identified as high grade IDC based on the presence of clusters of cells with enlarged nuclei invading into stromal tissue with minimal gland formation and nuclear pleomorphism.

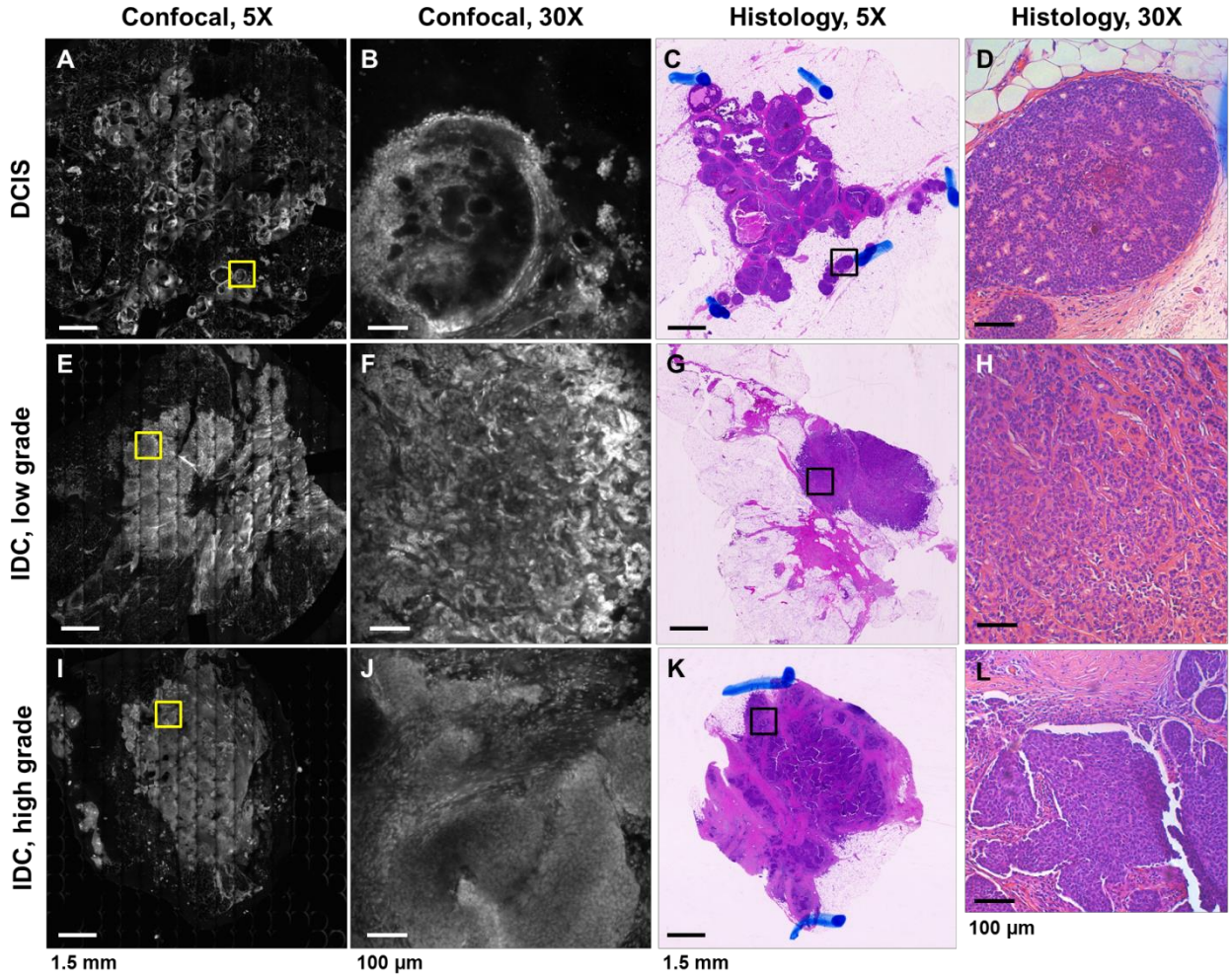

Figure 5-1: Representative confocal images and H&E-stained histologic slides of human breast tissue specimens assigned the same diagnosis and grade based on visual assessment. A-D: low/intermediate grade DCIS. E-H: low grade IDC. I-L: high grade IDC. Low magnification images show the lesion sections assessed. Yellow and black boxes on low magnification images indicate the areas shown in high magnification images. Scale bars represent 1.5 mm for low magnification images or 100 μm for high magnification images.

Table 5-1: Results of tumor diagnosis based on visual assessment of confocal and histologic images

		Confocal microscopy				
		Negative for tumor	DCIS	IDC	ILC	Total
Histology	Negative for tumor	0	0	0	0	0
	DCIS	1	3	2	0	6
	IDC	0	0	21	0	21
	ILC	0	0	3	0	3
	Total	1	3	26	0	30

Table 5-1 compares the results of tumor diagnosis made from the first reading of the histologic diagnosis to that of the first reading of confocal fluorescence microscopy. Of the 30 specimens evaluated, 29 specimens were classified as neoplastic in both confocal and histologic images. Twenty-one of the specimens were diagnosed as IDC and three specimens were diagnosed as DCIS in both confocal and histologic images. All three specimens diagnosed as ILC in histologic images were misclassified as IDC in confocal images. Half of the DCIS specimens (3/6) diagnosed in histologic images were misclassified as IDC or negative for tumor in confocal images.

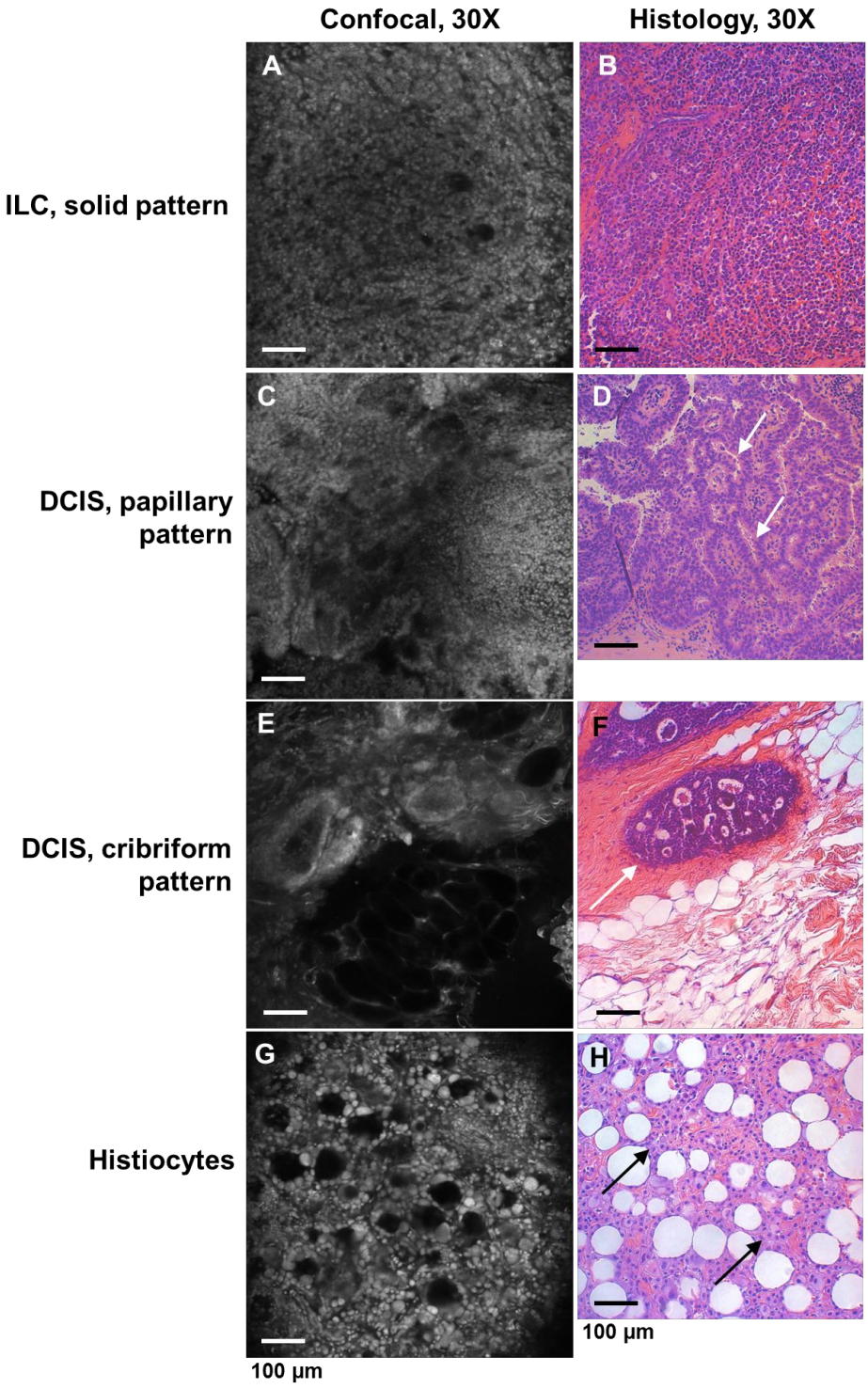

Figure 5-2: Representative confocal images and H&E-stained histologic slides of human breast tissue specimens assigned different diagnoses based on visual assessment. A,B: solid pattern ILC called IDC in confocal image. C,D: papillary pattern DCIS called IDC in confocal image. D: Arrows indicate folds of carcinoma cells characteristic of papillary pattern DCIS. E,F: cribriform pattern DCIS called negative for tumor in confocal image. F: Arrows indicate myoepithelial cells surrounding duct with DCIS. G,H: Histiocytes called IDC in confocal image. H: Arrows indicate benign histiocytes. Scale bars represent 100 μm for all images.

Figure 5-2 illustrates four specimens that were assigned incorrect diagnoses in confocal images. Each row illustrates a different cause of misdiagnosis in confocal images. In the top row (Figure 5-2: A,B) solid pattern ILC was misdiagnosed as IDC in the composite confocal image. The sheets of invasive tumor cells of solid pattern invasive lobular carcinoma invasion resembled IDC. Unlike the characteristic single-file invasion pattern of classic ILC, the solid pattern of ILC is a well-recognized cause of misdiagnosis even on conventional histopathological examination [157]. In the second row (Figure 5-2: C,D) DCIS with papillary pattern was misdiagnosed as IDC in the confocal image. The fibrovascular cores in the lesion were not well recognized in the confocal images. The tumor cells surrounding the fibrovascular cores alone were highlighted in the confocal images resulting in misdiagnosis as invasive carcinoma (indicated by arrows in Figure 5-2 D). The third row (Figure 5-2: E,F) shows cribriform pattern DCIS diagnosed on H&E section that was interpreted as negative for tumor on confocal images. Visual comparison of these images suggested that the histologic slide and the corresponding composite confocal image were acquired from different axial sections of this specimen, because the features of the lesion differed between the two images; in the confocal image the lesion showed inflammation and reactive changes adjacent to the previous biopsy site, while the histologic image showed several ductal spaces involved by DCIS. The bottom row (Figure 5-2: G,H) shows histiocytes (indicated by arrows in Figure 5-2 H) that were misdiagnosed as IDC in the confocal image.

Table 5-2: Summary of grades assigned in one review of confocal and histologic images

		Confocal microscopy			
		Low / intermediate grade	High grade	Undetermined grade	Total
Histology	Low / intermediate grade	19	1	1	21
	High grade	6	2	1	9
	Undetermined grade	0	0	0	0
	Total	25	3	2	30

illustrates four specimens that were assigned incorrect diagnoses in confocal images. Each row illustrates a different cause of misdiagnosis in confocal images. In the top row (Figure 5-2: A,B) solid pattern ILC was misdiagnosed as IDC in the composite confocal image. The sheets of invasive tumor cells of solid pattern invasive lobular carcinoma invasion resembled IDC. Unlike the characteristic single-file invasion pattern of classic ILC, the solid pattern of ILC is a well-recognized cause of misdiagnosis even on conventional histopathological examination [157]. In the second row (Figure 5-2: C,D) DCIS with papillary pattern was misdiagnosed as IDC in the confocal image. The fibrovascular cores in the lesion were not well recognized in the confocal images. The tumor cells surrounding the fibrovascular cores alone were highlighted in the confocal images resulting in misdiagnosis as invasive carcinoma (indicated by arrows in Figure 5-2 D). The third row (Figure 5-2: E,F) shows cribriform pattern DCIS diagnosed on H&E section that was interpreted as negative for tumor on confocal images. Visual comparison of these images suggested that the histologic slide and the corresponding composite confocal image were acquired from different axial sections of this specimen, because the features of the lesion differed between the two images; in the confocal image the lesion showed inflammation and reactive changes adjacent to the previous biopsy site, while the histologic image showed several ductal spaces involved by DCIS. The bottom row (Figure 5-2: G,H) shows histiocytes (indicated by arrows in Figure 5-2 H) that were misdiagnosed as IDC in the confocal image.

Table 5-2 illustrates the results of tumor grade classification in the first review of images acquired by histology with H&E staining and confocal fluorescence microscopy. Of the 30 specimens evaluated, 19 specimens were classified as “low/intermediate grade” and two specimens were classified as “high grade” in both confocal and histologic images. Six specimens that were identified as high grade in histologic images were misclassified as low/intermediate grade in confocal images, and one specimen identified as low/intermediate grade in the histologic image was classified as high grade in the corresponding confocal image. Two specimens, one classified as low/intermediate grade and one classified as high grade in histologic images, could not be classified as either high or low/intermediate grade in confocal images, because poor contrast and resolution precluded interpretation.

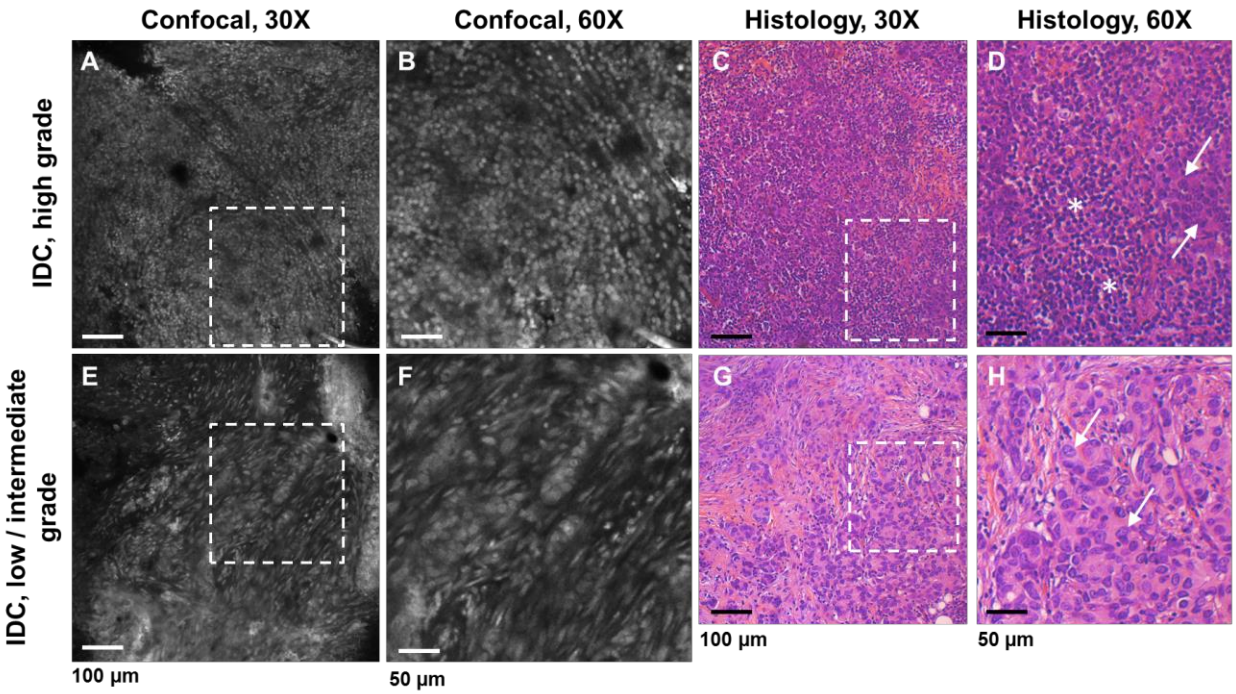

Figure 5-3: Representative confocal images and H&E-stained histologic slides of human breast tissue specimens assigned different grades based on visual assessment. A-D: High grade IDC called low/intermediate grade IDC in confocal images. A, C: Square regions indicated by white dashed line indicate areas shown at higher magnification in B and D. D: Carcinoma cells with marked nuclear pleomorphism are indicated by arrows and areas with lymphocytic infiltration are indicated by asterisks. E-H: Low/intermediate grade IDC called high grade IDC in confocal images. E, G: Square regions indicated by white dashed line indicate areas shown at higher magnification in F and H. H: Carcinoma cells with prominent nucleoli are indicated by arrows. Scale bars represent 100 μm for A, C, E, and G, and 50 μm for B, D, E, and H.

Figure 5-3 illustrates two specimens that were assigned different grades based on visual assessment of corresponding histologic and confocal images. The top row (Figure 5-3: A-D) shows high grade IDC that was misclassified as low/intermediate grade, because the presence of inflammation indicated by infiltrating lymphocytes (indicated by asterisks in Figure 5-3 D) resembled low grade disease and carcinoma cells with marked nuclear pleomorphism (indicated by arrows in Figure 5-3 D) were not well-recognized in the confocal image. The bottom row (Figure 5-3: E-H) shows low/intermediate grade IDC that was misclassified as high grade in the confocal image. Very focal areas showed larger nuclei which were misinterpreted as high grade for the overall tumor grade which comprised of sheets of tumor cells without gland formation but

with intermediate sized tumor nuclei. The carcinoma cells with prominent nucleoli in a focal area of the tumor are shown in the histologic image (indicated by arrows in Figure 5-3 H). The corresponding area in the confocal image that led to the misinterpretation is shown in Figure 5-3.

Table 5-3: Kappa coefficient characterizing agreement between two reviews of diagnosis and grade for each set of histologic and confocal images

Evaluation	Image Types	Kappa Coefficient	Standard Error	Level of Agreement	Critical Ratio	*p* value
Diagnosis	Histology review 1 versus histology review 2	1.00	0.15	Perfect	6.7	8.5E-12
	Confocal review 1 versus confocal review 2	0.36	0.14	Fair	2.5	0.01
Tumor Grade	Histology review 1 versus histology review 2	0.75	0.18	Substantial	4.1	1.8E-05
	Confocal review 1 versus confocal review 2	0.30	0.15	Fair	2.0	0.02

A kappa coefficient was calculated [125, 126] to quantify the agreement between two reviews of diagnosis and grade assigned to breast specimens in histologic and confocal images. There was perfect agreement between assigned diagnoses and substantial agreement between assigned grades in the two reviews of histologic images. Two reviews assessing diagnosis and grade in confocal images showed only fair agreement based on defined categories for kappa values [126, 141]. The estimated *p* values show that all kappa coefficients are significantly larger than zero, which indicates that each kappa coefficient represents higher agreement than would occur by chance.

5.4 Discussion

The objective of this study was to evaluate the feasibility of assessing tumor type and grade in images of neoplastic breast tissue specimens acquired with confocal fluorescence microscopy. A total of 29 out of 30 specimens (97%) were correctly classified as neoplasia based on assessment of confocal images. Reactive changes at previous biopsy site without any residual

tumor but including abundant histiocytes which was not correctly recognized on confocal fluorescence images accounted for the discordance and lowered sensitivity. Based on review of confocal and histologic images, 24 of 30 specimens (80%) were assigned the same diagnosis of tumor type and 21 of 30 specimens (70%) were assigned the same tumor grade. The agreement between tumor type and tumor grade assigned in two reviews of histologic images was perfect and substantial, respectively, based on calculated values of kappa coefficient [141]. However, the agreement between tumor type and tumor grade assigned in two reviews of confocal images was only fair.

Several previous studies have evaluated the feasibility of visual assessment of confocal microscopy for rapid analysis of core needle biopsy specimens and surgical margins. Schiffhauer et al., Tilli et al., and Parrish et al. demonstrated the feasibility of using reflectance confocal microscopy to evaluate neoplasia in human breast and murine mammary tissue specimens in comparison to histologic assessment, but these studies did not classify specimens shown in confocal images by tumor type or grade [96, 120, 121]. We previously demonstrated the feasibility of visual assessment of confocal fluorescence images to distinguish between neoplastic and non-neoplastic breast tissue with comparable sensitivity and specificity to histologic assessment [1]. Here we performed a preliminary evaluation to investigate if confocal images contain sufficient detail to determine tumor type and grade following the initial categorization of the tumor as benign or malignant in nature. The results of this study show that the accuracy of tumor type and grade determined from confocal images (80% and 70%, respectively) is lower than the accuracy of simply identifying whether tissue is neoplastic or not (over 90%).

The major limitation of confocal microscopy platform used in the study was the poor lateral resolution compared to conventional light microscopic histopathological examination, which precludes optimal visualization of cytologic and architectural details leading to misclassification of tumor type and grade. The theoretical resolution of the light microscope with the 40X objective is 0.45 μm, while the lateral resolution of the confocal fluorescence microscope is 2.0 μm (30X objective). All 3 cases of ILC and 2 cases of DCIS were misclassified as IDC, because the small, round cells in ILC tumors (Figure 5-2B), the characteristic folds of papillary pattern DCIS (indicated by arrows in Figure 5-2D), and myoepithelial cells that surround cribriform pattern DCIS (indicated by arrows in Figure 5-2F) were not visible in confocal images. Poor lateral resolution in confocal images also limited recognition of characteristic features of different tumor grades, including nucleoli, nuclear pleomorphism, and lymphocytic infiltration (indicated by arrows in Figure 5-3 D and H, and asterisks in Figure 5-3 D, respectively). In addition, as shown in Figure 5-2 G and H, low resolution can cause some benign cells, such as infiltration of histiocytes, to be misclassified as neoplasia. Improvements in the confocal microscope are needed to improve the lateral resolution, which could improve the concordance of the diagnosis, typing, and grading of the breast tumors made using confocal fluorescence microscopy with conventional histopathologic examination. Future studies will provide valuable information regarding the extent of improvement of sensitivity and specificity of making a primary diagnosis using confocal fluorescence images.

Classification of tumor type and grade in confocal fluorescence images could potentially also be improved by staining tissue specimens with additional fluorescent dyes conjugated to antibodies targeting markers [158, 159]. A variety of potential biomarkers could be targeted; for example, the loss of E-cadherin is commonly used to recognize lobular neoplasia by

immunohistochemistry [160-162]. E-cadherin is a transmembrane protein that mediates intercellular adhesion and is highly expressed in DCIS and IDC [163], but is poorly expressed in ILC [160, 162]. A previous study demonstrated staining MCF-7 breast cancer cells *in vitro* by conjugation of an anti-E-cadherin antibody (ab15148; Abcam®) to Alexa 555 Goat anti-rabbit (Invitrogen) [164]; this technique could potentially be optimized to target E-cadherin in intact tissue specimens. Similarly, calponin is a contractile protein that is expressed in contractile and cytoskeletal areas in smooth muscle cells, including in benign myoepithelial cells surrounding breast ducts [165, 166] and could be targeted to improve recognition of DCIS based on the presence of peripheral myoepithelial cells. P-cadherin is a transmembrane protein that mediates intercellular adhesion and is differentially expressed in high grade DCIS and low grade DCIS as well as high grade IDC and low grade IDC [159, 167, 168].

Another potential source of error occurs when the optical section imaged by confocal microscopy is axially separated from the section of tissue prepared as a histologic slide, which likely occurred in the case shown in Figure 5-2 E,F. In this case, the architecture between the two sections of the same specimen differed such that DCIS was interpreted negative for tumor in the confocal image. However, this source of error would be difficult to overcome in future studies, since it is not always feasible to prepare histologic slides from sections within 20 μm of the surface, the approximate location of confocal image acquisition.

Finally, in this study only one reader reviewed the confocal and histologic images. Future studies are needed to measure inter-observer agreement for assignment of diagnosis and grade to confocal and histologic images of breast neoplasia.

In conclusion, this preliminary study evaluated the feasibility of making a primary histologic diagnosis and assigning a type and grade to malignant breast tissue specimens in confocal images. All 21 cases of IDC and 19 of 21 cases with low / intermediate grade tumor were accurately classified in confocal images. Ultimately, the findings of this study show that poor lateral resolution of the confocal microscopy platform used in our study limits differentiation of ILC and DCIS from IDC and classification of high grade lesions. Improved lateral resolution in the confocal microscope is needed to improve recognition of features that indicate tumor grade, such as nucleoli, nuclear pleomorphism, and lymphocytic infiltration. Fluorescent contrast agents targeting markers associated with tumor type and grade could also potentially be developed to improve classification of tumor type in confocal images.

6 CHAPTER 6: Micro-anatomical quantitative optical imaging: automated assessment of breast tissues using nuclear and ductal parameters[3]

ABSTRACT: Pathologists currently diagnose breast lesions through histologic assessment, which requires fixation and tissue preparation. The diagnostic criteria used to classify breast lesions are qualitative and subjective, and inter-observer discordance has been shown to be a significant challenge in the diagnosis of selected breast lesions, particularly for borderline proliferative lesions. Thus, there is an opportunity to develop tools to rapidly visualize and quantitatively interpret breast tissue morphology for a variety of clinical applications. Toward this end, we acquired images of freshly excised breast tissue specimens using confocal fluorescence microscopy and proflavine as a topical stain. We developed computerized algorithms to segment and quantify nuclear and ductal parameters that characterize breast architectural features. A total of 33 parameters were evaluated and used as input to develop a decision tree model to classify benign and malignant breast tissue. The decision tree model that achieved the highest accuracy for distinguishing between benign and malignant breast features used the following parameters: standard deviation of inter-nuclear distance and number of duct lumens. The model achieved 81% sensitivity and 93% specificity, corresponding to an area under the curve of 0.93 and an overall accuracy of 90%. The model classified IDC and DCIS with 92% and 96% accuracy, respectively. The cross-validated model achieved 75% sensitivity and 93% specificity and an overall accuracy of 88%. These results suggest that proflavine

[3] The contents of this chapter have been published with no changes in the following journal article: Dobbs JL, Mueller JL, Krishnamurthy S, Shin D, Kuerer H, Yang W, Richards-Kortum R. Micro-anatomical quantitative optical imaging: towards automated assessment of breast tissues. Breast Cancer Res 2015; 17(105) DOI 10.1186/s13058-015-0617-9.

staining and confocal fluorescence microscopy combined with image analysis strategies to segment morphological features could potentially be used to quantitatively diagnose freshly obtained breast tissue at the point of care without the need for tissue preparation.

6.1 Introduction

Breast cancer diagnosis is an intricate process, which requires tissue procurement, rigorous tissue preparation and histologic assessment whether it is in the context of core needle biopsy diagnosis or surgical excision. Fixed tissue samples are processed after harvesting and are evaluated for presence and type of malignant breast tissue based on standardized histologic criteria [15, 79, 80, 169], which employ cytological and qualitative architectural features. Breast tumors that are diagnosed as malignant in nature are graded using different types of grading systems to categorize the tumors into groups to reflect their biology of progression. One of the most widely-used grading systems was developed by Bloom and Richardson in 1957, which used only qualitative criteria to evaluate breast lesions [169]. In 1991, Elston and Ellis published the Nottigham modification to the Bloom and Richardson grading system, which incorporated semi-quantitative criteria to evaluate tubule formation, nuclear pleomorphism, and mitotic count [80]. Extensive research has been done to evaluate the rate of inter- and intra-observer discordance using these grading systems for histologic assessment of fixed breast tissue. While some studies have shown that inter-observer agreement is high in the majority of cases [81], other studies have shown that subjective criteria can lead to inter-observer variation for margin assessment and poor reproducibility in evaluation of borderline and *in situ* lesions [82-87]. The availability of techniques that use quantitative criteria that can be applied without subjecting the tissue to processing can overcome the subjectivity of interpretation and may reduce the inter- and intra-observer variability in the histological evaluation of breast tissue [170]. Such techniques could

also be potentially useful in settings lacking the human resources and equipment necessary to perform standard histologic assessment, which can be a challenge in many parts of the world [130].

In order to characterize quantitative criteria to classify breast architecture, several studies have described segmentation algorithms based on nuclear [171-175] and ductal [176-178] morphometry in images of fixed tissue stained with hematoxylin and eosin (H&E) staining. Additionally, some recent studies evaluated nuclear morphometric parameters using wide-field fluorescence microscopy [179] and micro-optical computed tomography [180] to acquire images of breast tissue. Specifically, wide field fluorescence microscopy combined with watershed segmentation to quantify nuclei found that area fraction could distinguish between tumor and normal regions in excised rat mammary tissue with 97% accuracy [179]. Micro-optical computed tomography and nuclear morphometry was used to compare variations between human breast cell lines and found that nuclear volumes increased from normal to metastatic breast cells and that nuclei of abnormal cells contained more nucleoli [180].

The idea of establishing quantitative criteria on fixed tissue can be taken one step further to be applied directly to intact specimens using other imaging modalities, which can obviate the need for extensive tissue processing. Several studies have already described the feasibility of imaging breast tissue with confocal microscopy in a clinical setting [1, 2, 96, 120, 121, 137]. Schiffhauer and colleagues showed that confocal reflectance microscopy could be used to image benign and malignant breast features and provide visual similarity to H&E micrographs [121]. Abeytunge and colleagues demonstrated that confocal fluorescence microscopy can be used to rapidly acquire images of fresh tissue specimens between 1-2.5 cm^2 in size [137]. Our group recently showed that confocal fluorescence microscopy yields images with sufficient detail to

identify benign and malignant breast architecture in freshly-excised tissue [1]. In another recent study, we demonstrated that confocal fluorescence images can be used to estimate percent tumor cellularity in core needle biopsy specimens and can indicate the adequacy of procured tissue for diagnosis and ancillary molecular and immunophnenotypic studies [2].

The goal of this work is to combine both quantitative image processing techniques with optical microscopy of intact breast tissue specimens for interpretation of breast tissue at the point of care. The benefits of this approach are minimal tissue processing, rapid diagnosis, and quantitative criteria that could potentially reduce the subjectivity with intra- and inter-observer variation in the evaluation of breast histology. In this study, we combine clinical confocal microscopy with a computerized image processing algorithm to quantify both nuclear and ductal morphology of breast tissue; we develop an algorithm using these parameters to classify breast tissue as benign - negative for tumor - or malignant - tumor tissue present. Although previous studies have described evaluation of breast architecture in histologic images [171-178], these studies only considered either nuclear or ductal parameters. We show that combining both yields improved diagnostic performance, particularly in the diagnosis of invasive ductal cancer (IDC) and ductal carcinoma in situ (DCIS). The nuclear and ductal parameters described in this study could potentially be used for objective categorization of breast lesions.

6.2 Methods

6.2.1 Breast tissue acquisition and preparation

Fresh human breast tissue specimens were acquired through a protocol approved by The University of Texas MD Anderson Cancer Center and Rice University Institutional Review Boards, and each participant gave written informed consent. Fresh breast tissue was acquired from patients undergoing surgery to excise a clinically abnormal lesion. The procedure for tissue

preparation has been described previously [1]. In brief, two tissue specimens - one grossly abnormal and one grossly normal in appearance were acquired from each patient for image acquisition and evaluation; each specimen measured approximately 15 x 15 mm^2 in size, with thickness varying from 2-7 mm. Within 30 minutes of surgical excision, breast tissue specimens were stained for one minute in a solution of 0.01% proflavine in 1X phosphate buffed saline (PBS). Proflavine is a nuclear contrast agent [122, 124], which has been used to stain breast tissue, oral mucosa, Barrett's esophagus, cervical tissue, and sarcoma in previous studies [1, 2, 102, 181-185]. Following topical application of proflavine, specimens were washed with 1X PBS and then immediately imaged.

6.2.2 Image acquisition and evaluation

Confocal fluorescence images were acquired from multiple sites within each specimen using a multi-wavelength scanning confocal microscope (Vivascope 2500®, Caliber Imaging and Diagnostics) as described previously [1, 2, 186]. Following topical application of proflavine and the PBS wash, each tissue specimen was positioned on the microscope stage and imaged using 2.1 ± 0.4 mW power at 488 nm laser excitation, and the fluorescence was detected in a band pass of 550 ± 44 nm with a 30x water immersion lens. At these settings, the lateral and axial resolution was 1.0 μm and 5.0 μm, respectively, in the center of the 750 x 750 μm^2 field of view. A 12 x 12 mm^2 composite image was created for both sides of each tissue specimen. To create the composite image, images were acquired from contiguous sites in a grid pattern (maximum area 12.2 x 12.2 mm^2) over the surface of the specimen at an approximate depth of 20 μm. Following image acquisition, specimens were kept moist in 1X PBS and were submitted for routine histologic preparation and fixation. Samples were stained with H&E and fixed on microscope slides for histologic assessment.

A board-certified, breast pathologist (author S. Krishnamurthy) viewed composite confocal images and fixed tissue specimens stained with H&E using a conventional light microscope to identify sites that corresponded to the same approximate location in the specimen based on similar image morphology. Specifically we selected in-focus confocal microscope fields of view that contain representative examples of characteristic benign and malignant breast features. Thus, at each site, a corresponding pair of confocal and H&E images were available from a 750 μm x 750 μm field of view. At each site, the H&E images of fixed tissue specimens were used as a reference standard to identify breast architectural features that should be present in corresponding confocal images [1, 15]. Benign breast features identified in reference H&E images included adipose and fibrous tissue, lobules, non-hyperplastic ducts, and ductal hyperplasia. Malignant breast features identified in reference H&E images included: ductal carcinoma *in situ* (DCIS), invasive ductal carcinoma (IDC), and invasive lobular carcinoma (ILC).

6.2.3 Nuclear segmentation and connected components algorithm for identifying nuclei

A technique called maximally stable extremal regions (MSER) was used to segment nuclei from confocal images of proflavine stained breast tissue. MSER has been used previously in the image processing community for automatic reconstruction of 3D scenes; here we have adapted it to segment nuclei from high resolution fluorescence confocal microscopy images [187]. MSER employs intensity thresholding; however, no global or optimal threshold is sought; rather all thresholds are tested and the stability of the isolated connected components (i.e. nuclei) is evaluated. All possible thresholds from 0 to 255 are applied to an image and the sets of connected components (as well as their area) are stored (Figure 6-1:A-D). This yields a data structure in which the area of each connected component is stored as a function of the intensity

threshold. Finally, the intensity thresholds which correspond to local minima in the rate of change of the area function are selected as thresholds producing MSER.

In order to apply MSER to our images, five tuning parameters associated with MSER had to be selected. The first two parameters, which included the minimum area (MinArea) and maximum area (MaxArea) of the connected components, are related to the expected size of nuclei. These parameters were selected based on the biologically expected range of nuclear diameters. Specifically, other groups have found nuclear volume to range from approximately 200 to 1500 μm^3, which corresponds to 7 to 14 μm in diameter [180]. Therefore, MaxArea was set to 500 pixels, which corresponds to 19 μm in diameter, which is larger than the expected nuclear size for our images. MinArea was set to 35 pixels, which corresponds to 5 μm in diameter, which is smaller than the expected nuclear size for our images. The next set of parameters is related to the intensity thresholds and includes maximum variation (MaxVariation), minimum diversity (MinDiversity), and Delta. MaxVariation is the maximum variation allowed within a region that corresponds to a potential nucleus. MinDiversity is employed if there are two nested maximally stable regions. Specifically, if the diversity between the two nested regions is less than MinDiversity, then the nested region is removed. Lastly, Delta is the stability threshold. The stability of a region is defined as the relative variation of the region area when the intensity is changed by delta/2. These intensity parameters were systematically tuned through applying a range of values to representative images in order to select the best value for each parameter. Specifically, one input parameter was varied over a wide range while other input parameters were held constant. For each iteration, the area fraction (AF) from representative images of tumor and normal tissue was calculated and overlays of the features isolated with that particular setting were displayed.

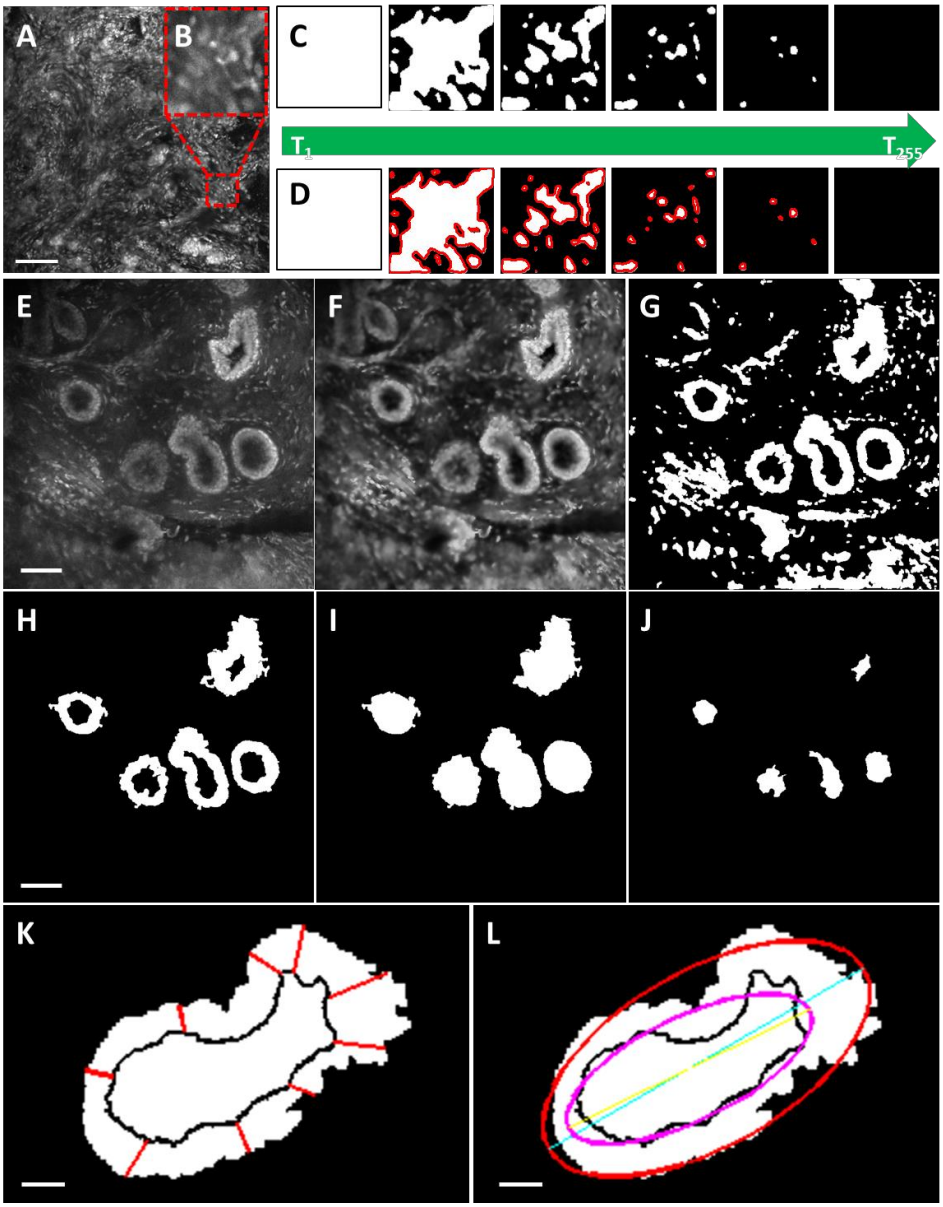

Figure 6-1: Algorithms for nuclear (A-D) and ductal (E-L) segmentation. Nuclear segmentation: A: Raw image acquired from confocal fluorescence microscope with 750 x 750 μm^2 field of view. B: Region of interest selected in confocal fluorescence image with 75 x 75 μm^2 field of view. C: The maximally stable extremal regions (MSER) algorithm applies thresholds from 0 to 255 to B. D: At each threshold, the MSER algorithm identifies nuclei as connected components and selects "maximally stable" components with the lowest size variation. Ductal segmentation: E: Raw image acquired from confocal fluorescence microscope with 750 x 750 μm^2 field of view. F: Wiener low pass filter and adaptive histogram equalization applied to E. G: The algorithm converts E to a binary image using an interactive threshold tool. H: Objects below range of nuclear area are removed and then user selects a region of interest (ROI) around ducts with an interactive polygon selection tool. I: The algorithm fills boundaries of ducts identified in H to segment the outer boundaries of the duct. J: The algorithm selects the complement of H to segment the inner boundaries of the duct (lumen). K: Duct wall width is measured by selecting the shortest distance from the outer to the inner duct boundaries (red lines). L: Ellipses are fitted to outer and inner duct boundaries. E-J: scale bar is 100 μm. K,L: scale bar is 25 μm.

The values that led to the largest differences in AF between tumor and normal tissues, while isolating features that approximately corresponded to nuclei or nucleoli, were selected. An illustration of this tuning approach can be found in Figure 6-2. Specifically, MaxVariation was set equal to 2.5, MinDiversity to 0.5, and Delta to 6. These parameter values are in terms of relative intensity, which for our 8 bit images ranges from 0 to 255.

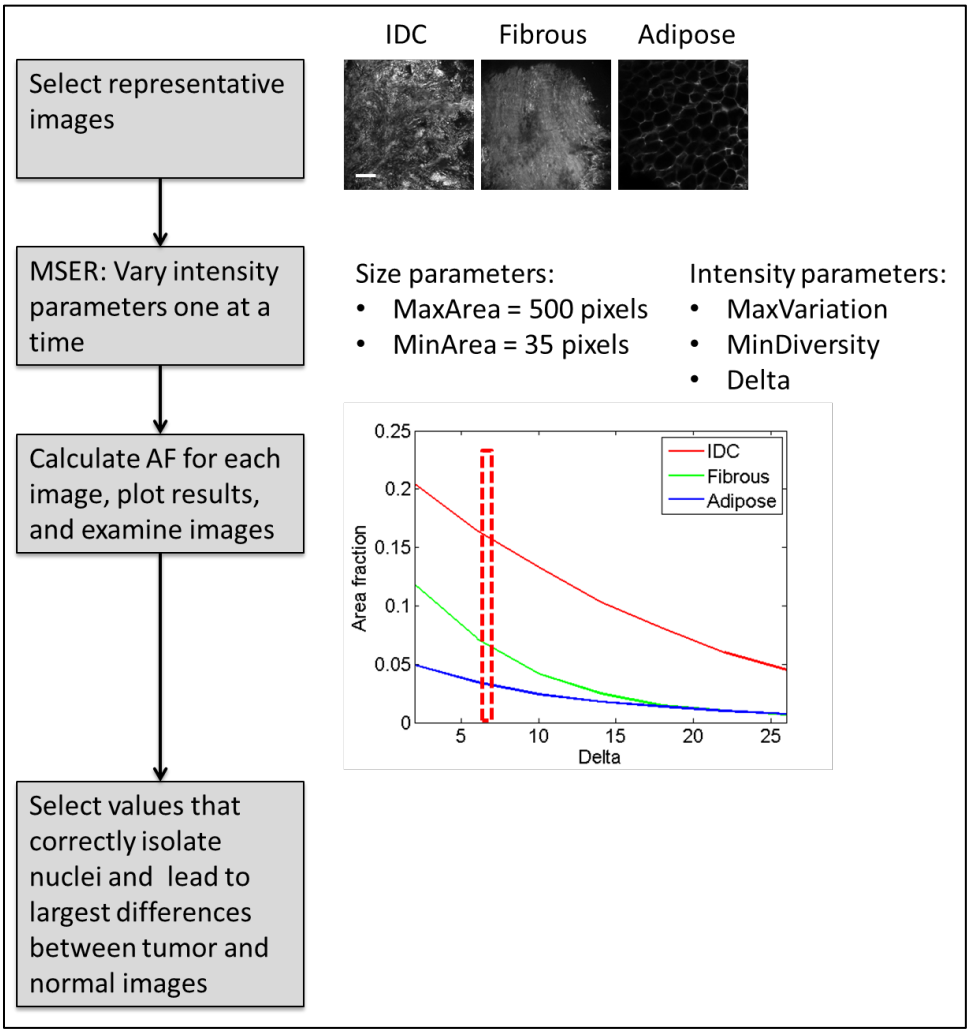

Figure 6-2: Illustration of methodology used to select MSER intensity parameters. The intensity parameters MaxVariation, MinDiversity, and Delta were selected by varying each parameter one at a time. The area fraction (AF) was calculated for each representative image after each iteration of MSER. Each intensity parameter was plotted as a function of AF. Values for the intensity parameters were selected based on which values correctly isolated nuclei from the representative images and which values led to the largest differences between tumor and benign images. Scale bar 100 μm.

After nuclei were isolated with MSER, a connected components algorithm was applied in order to calculate parameters such as nuclear density and diameter. In the connected components algorithm, all touching or connected pixels are assumed to belong to the same cell nucleus. Parameters include nuclear density (the number of nuclei in a unit area), area fraction (the total nuclear area divided by the total area), minimum internuclear distance (the distance from a nucleus center to the next closest nucleus center), and nuclear diameter (the length of the major axis of each nucleus). Nuclear density and area fraction (AF) represent scalar variables – only one value is returned for each image, while the minimum internuclear distance (IND) and nuclear diameter represent vector variables – a value is calculated for each nucleus in the image. In order to consolidate the vector variables into a scalar value, several summary statistics were evaluated, including mean, median, mode, interquartile range, and standard deviation.

6.2.4 Ductal segmentation algorithm and quantification of ductal parameters

An algorithm was developed to measure ductal parameters, which segments non-hyperplastic ducts, ductal hyperplasia, and DCIS lesions based on the intensity of proflavine staining (Figure 6-1:E-L). To reduce noise and increase image contrast, a Wiener lowpass filter was first applied (Figure 6-1:E) followed by contrast-limited adaptive histogram equalization (CLAHE, Figure 6-1:F). Images were converted from grayscale to binary using a user-defined threshold based on relative intensity. The mean threshold used to segment ducts was 107 ± 27 (range: 52-168) on a scale of 0 to 255 for 8 bit images (Figure 6-1:G). It was not possible to select a universal threshold, because in order to accurately segment ducts from surrounding tissue, it is necessary to isolate both nuclei in the duct walls and inter-nuclear space between them. The relative intensity of these features differed between images due to the variation in illumination power used for image acquisition and the variation in proflavine staining. Areas smaller than the upper threshold for cell nuclei (approximately equivalent to 280 μm^2 or 500 pixels, with a

diameter of 19 μm [188]) were removed to avoid segmenting individual nuclei outside of the duct walls. Individual ducts were manually segmented using a user-defined polygon selection tool to define architectural features corresponding to breast ducts (Figure 6-1:H). After application of the ductal segmentation algorithm, the binary confocal image showed the segmented duct walls (Figure 6-1:H) and the outer and inner boundaries (Figure 6-1:I,J) of the duct used to measure ductal parameters.

Following segmentation of ducts, a number of ductal parameters were measured based on the properties of the inner and outer duct boundaries. The outer boundary defines the outer edge of the duct wall and the inner boundary defines the inner edge of the duct wall; the lumen. The width of the duct wall was measured at every pixel on the outer edge of the duct wall. This was done by finding the shortest distance between every point on the outer boundary and the nearest point on the inner boundary (Figure 6-1:K). Duct wall width was measured for each non-hyperplastic duct, ductal hyperplasia, and DCIS lesion and the vector of values were summarized by calculating the mean, median, mode, interquartile range, and standard deviation. Other scalar parameters measured include the area of the duct wall, area of the lumen, area of an ellipse approximating the duct wall, area of an ellipse approximating the lumen, lengths of the major and minor axes for the duct and the lumen, solidity of the duct and the lumen, and eccentricity of the duct and the lumen (Figure 6-1:L).

6.2.5 Statistical analysis and model building

Nuclear parameters were calculated for all sites (n = 259) and ductal parameters were calculated for all sites that contained ducts (n=50), and the diagnostic performance of each image parameter was individually assessed by determining the classification accuracy. Two-class linear discriminant analysis was performed to classify malignant from benign breast architectural

features based on each individual nuclear or ductal parameter; receiver operator characteristic (ROC) curves were constructed and area under the curve (AUC) was calculated for each ROC curve. Sensitivity and specificity values were determined at the optimal cutpoint. Parameters were sorted by accuracy for classification of neoplasia based on AUC values. Boxplots were created for the parameters with the highest AUCs. A Student t-test for samples with unequal variances was used to identify statistically significant differences between mean parameter values measured in benign and malignant tissues. This analysis was performed to evaluate individual nuclear and ductal parameters to incorporate into a classification model.

Next we sought to develop a multivariate model to yield optimal separation between benign and malignant tissues. Towards that end, all 33 nuclear and ductal variables were used as input for a classification and regression tree (CART) function in Matlab. Decision trees were constructed using the automated Matlab function classregtree, which selects parameters and cutpoints that lead to the optimal classification of benign and malignant breast architectural features. Decision trees were pruned to prevent a single nuclear or ductal from being used at more than one node within the tree. Pruning was also performed to prevent the number of categories for classification of malignant breast features from exceeding 3: the number of malignant tissue types (IDC, ILC, and DCIS). After construction, decision tree nodes were pruned by finding the next higher node whose decision point led to two categories, one with a majority of neoplastic sites, and one with a majority of benign sites. A custom leave one out cross-validation algorithm was also developed in order to calculate the cross-validated sensitivity and specificity. Specifically, 258 of the 259 data points were used to build a CART model, which contained the same two variables at the first and second decision points as is seen in Figure 6-6. Specifically the standard deviation of IND (StdIND) was the first decision point and the number

of lumens was the second decision point. However, with each iteration of leave one out cross-validation, the cutoff value of StdIND could vary. The cutoff value associated with the number of lumens (number of lumens >1) was held constant because biologically normal ducts are expected to only contain a single lumen; therefore, this was considered to be the optimal and only logical cutoff value and therefore was held constant. Then the model was applied to the remaining data point, which was classified as either benign or malignant. This process was repeated for all 259 data points, and the calculated diagnosis for each image was compared to the known diagnosis in order to calculate sensitivity and specificity for the cross-validated model. The performance of the decision tree was characterized by computing sensitivity and specificity for classification of malignant breast architectural features. Additionally, sensitivity and specificity were calculated for each individual histologic type of malignant tissue in order to determine the relative classification accuracy for IDC, ILC, and DCIS sites. For example, in order to calculate sensitivity for IDC, true positives were defined as IDC sites that had been classifed as malignant by the decision tree, and false negatives were defined as IDC sites that had been classified as benign. Specificity was calculated by defining true negatives as benign sites that were correctly classified in the decision tree and false positives were defined as benign sites that were incorrectly classified. An ROC curve was constructed for the decision tree model in Figure 6-6. All sites were sorted in order of ascending StdIND value and then sensitivity and specificity for classification of neoplasia were calculated at every StdIND value. The cutoff value for number of lumens was held constant at 1 lumen because biologically normal ducts are expected to only contain a single lumen. AUC was calculated based on the resulting ROC curve.

6.3 Results

A total of 259 sites from 36 patients were identified in composite confocal fluorescence images. A summary of patients, sites, and diagnoses are included in Table 6-1. In total there were 179 benign sites, which included adipose tissue, fibrous tissue, lobules, and benign ducts, and 80 malignant sites, which included DCIS, IDC, and ILC.

Table 6-1: Summary of patients from which tissue specimens were acquired, sites analyzed with segmentation algorithms, and histologic diagnoses for each site

Diagnosis	Patients	Sites
Benign		
Adipose tissue	18	42
Fibrous tissue	16	31
Lobules	12	82
Non-hyperplastic ducts	9	20
Hyperplastic ducts	4	4
Malignant		
Ductal carcinoma in situ (DCIS)	6	26
Invasive ductal carcinoma (IDC)	15	37
Invasive lobular carcinoma (ILC)	3	17
Total	36	259

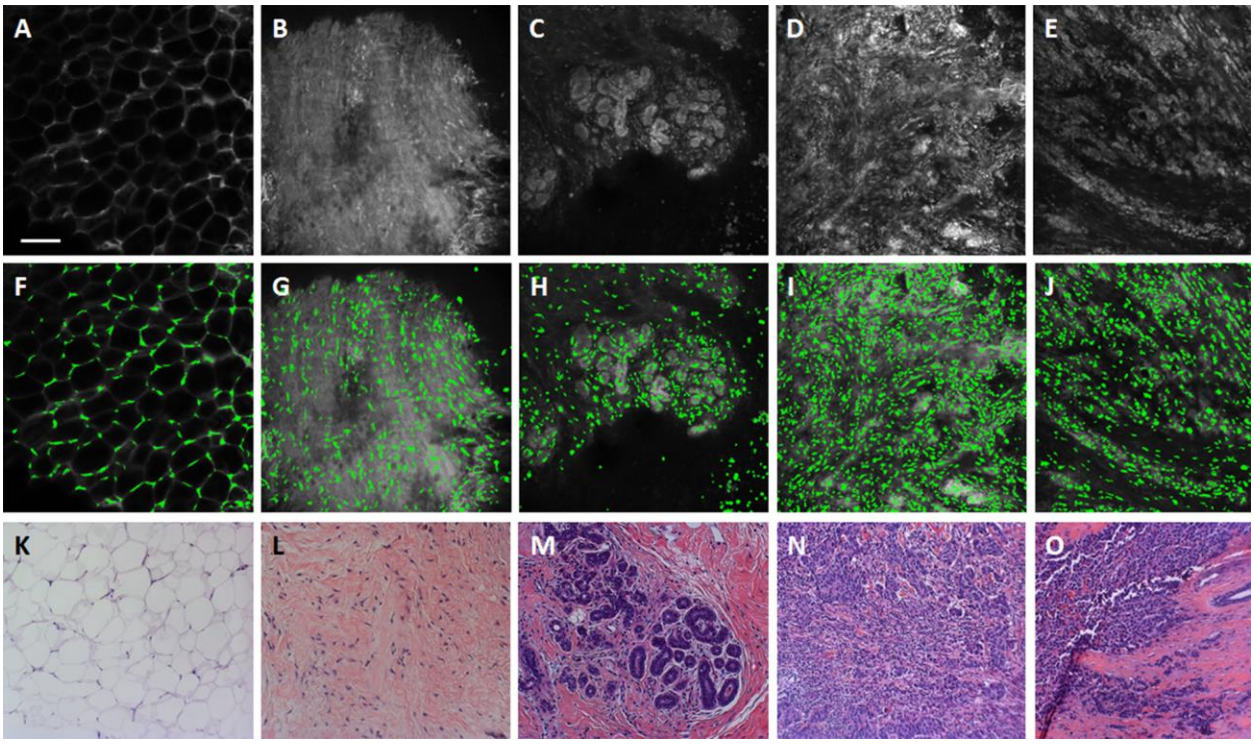

Figure 6-3: Representative raw confocal fluorescence images of adipose tissue, fibrous tissue, lobules, invasive ductal carcinoma, and invasive lobular carcinoma are shown in A through E, respectively. F-J: Nuclei segmented by identifying maximally stable extremal regions (MSER) are false colored green and overlaid onto the raw confocal fluorescence image. K-O: Histologic slides with H&E staining show similar histology to confocal images in A-E. Slides were prepared with the same specimens from which confocal images were acquired. Scale bar is 100 μm.

Figure 6-3 shows representative confocal images of sites without ducts acquired by confocal fluorescence microscopy in row 1 and nuclei isolated with MSER at those sites in row 2. Row 3 of Figure 6-3 shows sites in the corresponding histologic slide with H&E staining that have similar histology to the confocal sites. Nuclei were false-colored green and overlaid onto the original images for visualization. As seen, nuclei are isolated at the periphery of adipose cells in Figure 6-3F and are dispersed throughout the fibrous tissue image in Figure 6-3G. Denser clusters of nuclei are isolated in and around lobules in Figure 6-3H. Nuclei are the most dense at sites with malignant tissue, including IDC and ILC (Figure 6-3:I,J).

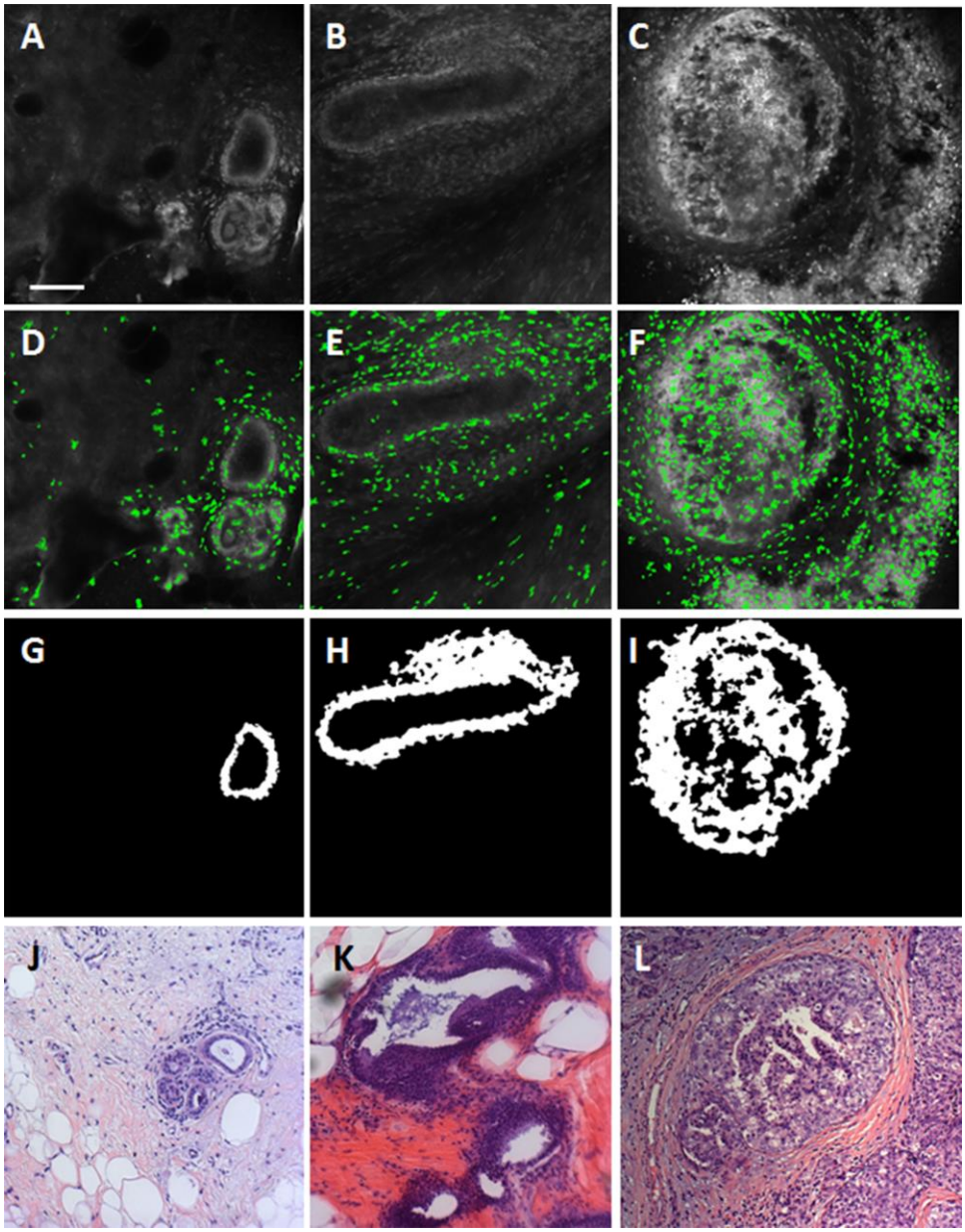

Figure 6-4: Representative confocal images of normal, non-hyperplastic ducts (A), hyperplastic ducts (B), and ductal carcinoma in situ (C) analyzed with the nuclear segmentation algorithm (middle row) and with the ductal segmentation algorithm (bottom row). D-F: Nuclei segmented by identifying maximally stable extremal regions (MSER) are false colored green and overlaid onto the raw confocal fluorescence image. G-I: Breast ducts segmented using the ductal segmentation algorithm. J-L: Histologic slides with H&E staining show similar histology to confocal images in A-E. Slides were prepared with the same specimens from which confocal images were acquired. Scale bar is 100 μm.

Figure 6-4 shows representative images of breast ducts acquired with confocal fluorescence microscopy in row 1, nuclei that were isolated at sites with breast ducts using

MSER in row 2, and ducts that were segmented with the ductal segmentation algorithm in row 3. Row 4 of Figure 6-4 shows sites in the corresponding histologic slide with H&E staining that have similar histology to the confocal sites. Nuclear density in and around the ducts increases from the non-hyperplastic duct, to the hyperplastic duct, to DCIS (Figure 6-4: D, E, F). However, relatively few nuclei are successfully isolated using MSER within the non-hyperplastic and hyperplastic ducts, which is most likely due to the fact that the borders of individual nuclei are difficult to visually discern in confocal fluorescence images. The images of sites isolated with the ductal segmentation algorithm show well-defined lumens in both the non-hyperplastic duct and hyperplastic duct (Figure 6-4G and H). Conversely, the image of DCIS shows bridges of cells crossing the lumen to create a cribriform pattern with several lumens.

The parameters that yielded the highest performance for distinguishing between benign and malignant sites are shown in Table 6-2. We evaluated the performance of nuclear parameters for classification of benign and malignant features in all sites and in sub-groups of sites that did or did not contain ducts to determine the groups for which nuclear parameters had the highest classification accuracy. We only evaluated the classification accuracy of ductal parameters at sites that contained ducts. Nuclear parameters measured at non-duct sites achieve higher performance (AUC = 0.93) than nuclear parameter measured at duct sites (AUC = 0.69). Conversely, ductal parameters achieve higher performance (AUC = 0.92) than nuclear parameters for classification of duct sites (AUC = 0.69). These findings suggest that a combination of nuclear parameters measured at non-duct sites and ductal parameters measured at duct sites may yield improved separation between all benign and malignant sites.

Table 6-2: Summary of top performing parameters for distinguishing between benign and malignant sites measured using the nuclear and ductal segmentation algorithms. A: Nuclear parameters measured at all sites using the nuclear segmentation algorithm. B: Nuclear parameters measured at all sites except those with breast ducts (normal ducts, hyperplastic ducts, and ductal carcinoma in situ) using the nuclear segmentation algorithm. C: Nuclear parameters measured at sites with breast ducts using the nuclear segmentation algorithm. D: Ductal parameters measured at sites with breast ducts using the ductal segmentation algorithm.

Group	Performance metric	Standard deviation of inter-nuclear distance	Area fraction	Range of inter-nuclear distance
A. Classification by Nuclear Parameter – All Sites	AUC	0.87	0.86	0.87
	Sensitivity	78	76	76
	Specificity	82	79	85
B. Classification by Nuclear Parameter – Non-duct Sites	AUC	0.93	0.92	0.91
	Sensitivity	85	80	81
	Specificity	88	87	88
C. Classification by Nuclear Parameter – Duct Sites	AUC	0.68	0.72	0.74
	Sensitivity	46	65	62
	Specificity	100	70	96
Group	Performance metric	Number of lumens	Minor dimension of outer ellipse	Area of outer ellipse
D. Classification by Duct Parameter – Duct Sites	AUC	0.92	0.83	0.82
	Sensitivity	88	73	81
	Specificity	88	79	75

Boxplots showing the mean and interquartile range of the top three performing nuclear parameters are shown in Figure 6-5A-C. Both Std IND and Range IND decrease from adipose to fibrous to lobules to ILC to IDC (Figure 6-5A and C), while AF increases from adipose to fibrous to lobules to ILC to IDC (Figure 6-5B). This trend suggests that the number of clusters of nuclei increases from adipose tissue, which has the fewest, to IDC, which has the greatest number of clusters of nuclei. All comparisons between benign (adipose, fibrous, lobules) and malignant (IDC, ILC) sites were significant. Similarly, AF increases from adipose to fibrous to lobules to IDC (Figure 6-5B), which suggests increasing nuclear density.

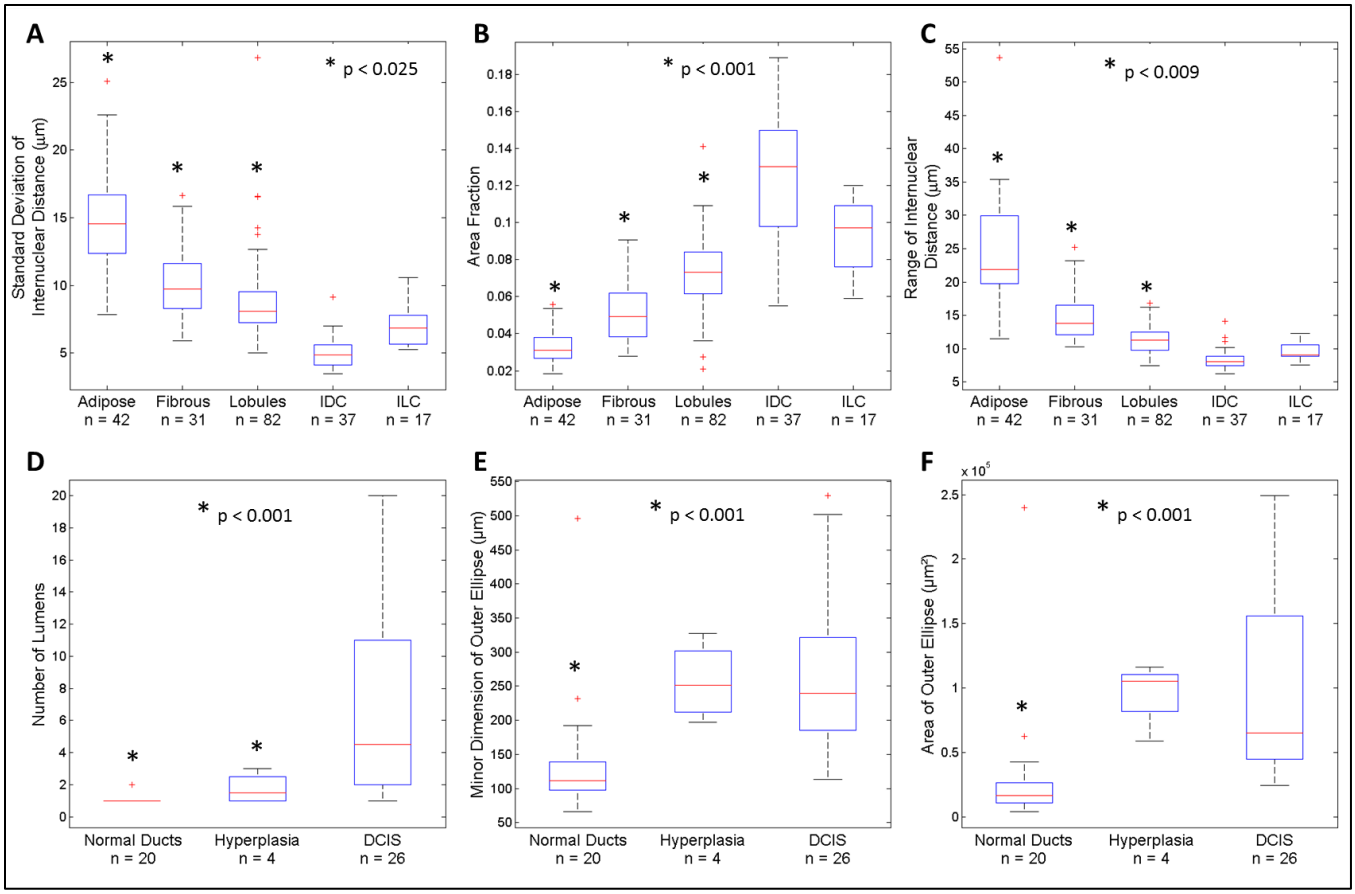

Figure 6-5: Mean value of parameters used to separate malignant from benign sites. Nuclear parameters calculated with the nuclear segmentation algorithm are shown for all adipose, fibrous, lobules, invasive ductal carcinoma (IDC), and invasive lobular carcinoma (ILC) sites; A: standard deviation of inter-nuclear distance; B: area fraction; C: range of inter-nuclear distance. Ductal parameters calculated with the duct-based segmentation algorithm are shown for all normal, non-hyperplastic ducts, hyperplastic ducts (Hyperplasia), and ductal carcinoma in situ (DCIS); D: number of lumens; E: minor dimension of outer ellipse; F: area of outer ellipse. The number of sites represented in each box is represented by n. Significant differences between mean values of parameters measured at benign and malignant sites are indicated by asterisks (*).

Boxplots showing the mean and interquartile range of the top three performing ductal parameters for duct sites are shown in Figure 6-5D-F. DCIS lesions have a significantly higher number of lumens than hyperplastic and non-hyperplastic ducts ($p < 0.001$), which is consistent with the cribriform pattern that occurs when abnormally high cellular proliferation causes the luminal space to be filled with epithelial cells (Figure 6-5 D). Figure 6-5E shows that the minor dimension of the outer ellipse approximating the duct is significantly smaller in normal, non-

hyperplastic ducts than in DCIS lesions ($p < 0.001$). There is no significant difference in the minor dimension between ellipses approximating hyperplastic ducts and DCIS lesions (Figure 6-5E). Figure 6-5F shows that the area of the outer ellipse approximating duct area was significantly smaller in normal, non-hyperplastic ducts than in DCIS lesions ($p < 0.001$). There is no significant difference between the average area of outer ellipses approximating hyperplastic ducts and DCIS lesions (Figure 6-5F).

All 33 nuclear and ductal parameters were used as input for a classification and regression tree (CART) algorithm to automate selection of parameters to discriminate benign and malignant sites. The CART algorithm was pruned to remove redundancies and over-fitting to the data set. The classification tree generated through this process is shown in Figure 6-6. Std IND with a cutoff value of 6.83 μm is the first decision point selected for classification by the decision tree, followed by number of lumens with a cutoff value of 1. Std IND < 6.83 μm separates out 52 true positives composed of IDC, DCIS, and ILC sties and 9 false positives composed of fibrous and lobule sites. The remaining sites enter the second node – Number of lumens > 1– which separates out 13 true positive DCIS sites and 3 false positive hyperplasia and normal duct sites. The remaining sites are classified as benign and are composed of 167 true negative adipose, fibrous, lobule, normal duct, and hyperplasia sites and 15 false positive IDC, DCIS, and ILC sites.

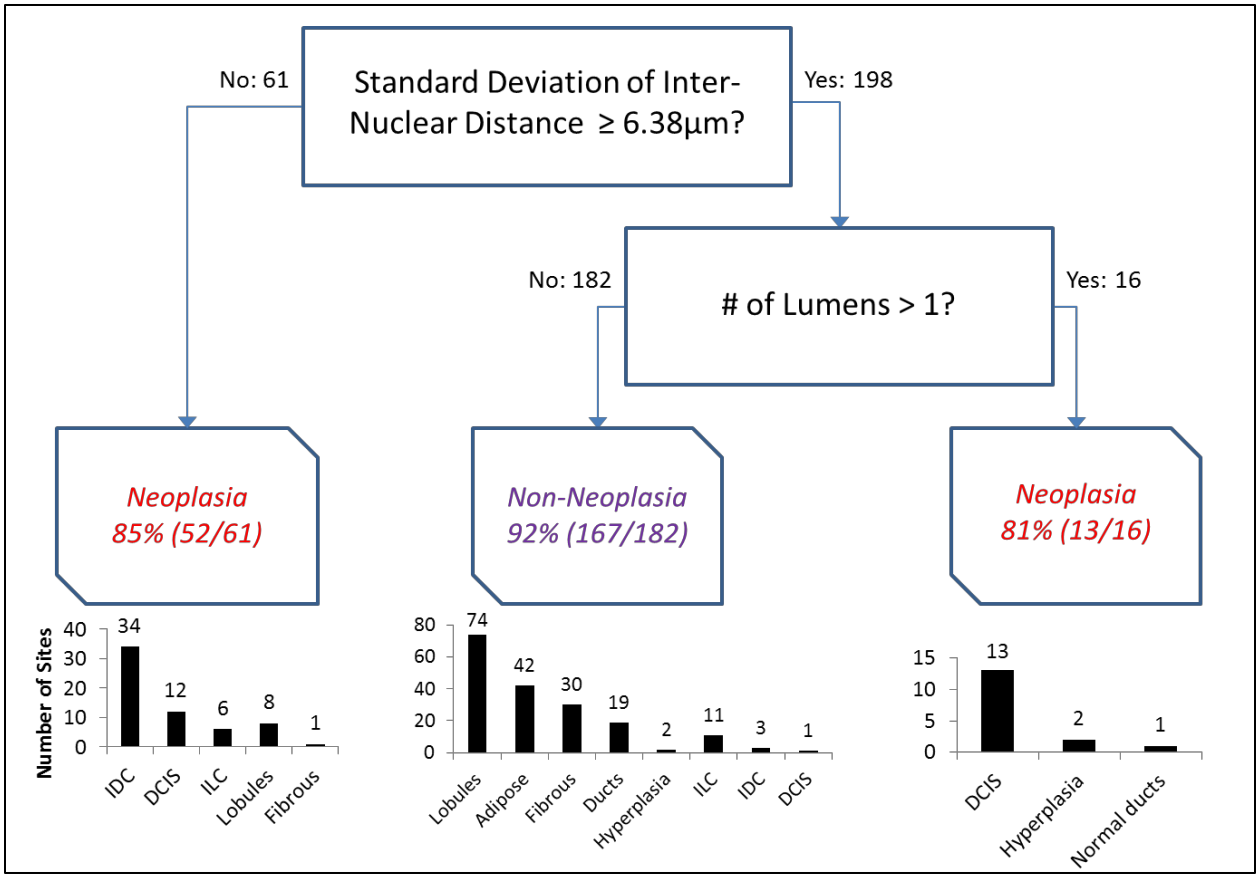

Figure 6-6: Classification tree automatically generated when all nuclei and duct data was used. Duct- and nuclei-based parameters selected by classification regression tree analysis to optimize separation between benign and malignant sites. Bar graphs show the diagnoses of sites sorted into each classification category.

Overall, the model achieved a sensitivity and specificity of 81% and 93% respectively, corresponding to an area under the curve of 0.93 and 90% overall classification accuracy, as shown in Table 6-3. If the model is evaluated based on classification of individual histologic types of neoplasia, 92% of IDC sites and 96% of DCIS sites were classified correctly. However, the model correctly classified only 35% of ILC sites. Additionally, leave one out cross-validation was performed, which yielded a cross-validated sensitivity of 75% and specificity of 93% (Table 6-3).

Table 6-3: Performance of classification tree model for classification of neoplasia, non-neoplasia, and individual histologic types of breast neoplasia in confocal fluorescence images.

	Sensitivity	Specificity
Classification Tree Model	81% (65/80)	93% (167/179)
Cross-validated Model	75% (60/80)	93% (167/179)
	Correctly Classified	
All Sites	90% (232/259)	
DCIS	96% (25/26)	
IDC	92% (34/37)	
ILC	35% (6/17)	

Specifically, cross-validation resulted in a 6% drop in sensitivity (from 81% to 75%) due to the fact that 5 additional IDC images were incorrectly classified during cross-validation. When each of these 5 cases was left out of the original cohort of data used to form the model (in other words during the leave one out cross-validation exercise), the cutoff value associated with StdIND dropped. This resulted in each of the 5 cases being classified as a false negative. For the remainder of the images, the cutoff value associated with StdIND remained the same as it is in Figure 6-6, resulting in the same specificity of 93%.

As seen in the histograms in Figure 6-6, ILC sites account for the largest number of false negative (n = 11 out of 17 sites) while lobule sites account for the largest number of false positives (n = 8 out of 82 sites). Figure 6-7 shows representative confocal images of a true positive ILC, false negative ILC, true negative lobules, and false positive lobules sites in row 1 and nuclei isolated with MSER at those sites in row 2. Row 3 of Figure 6-7 shows sites in the corresponding histologic slide with H&E staining that have similar histology to the confocal sites. As seen, there are large differences in the density and clustering of nuclei between the true positive ILC site (Figure 6-7E) and true negative lobules site (Figure 6-7G). In comparison to Figure 6-7E, the false negative ILC site in Figure 6-7F has relatively few nuclei, which appear to

be predominately clustered in the upper left region of the image. Conversely, the false positive lobules site in Figure 6-7H contains more nuclei than Figure 6-7G, particularly in stromal tissue located in between lobules.

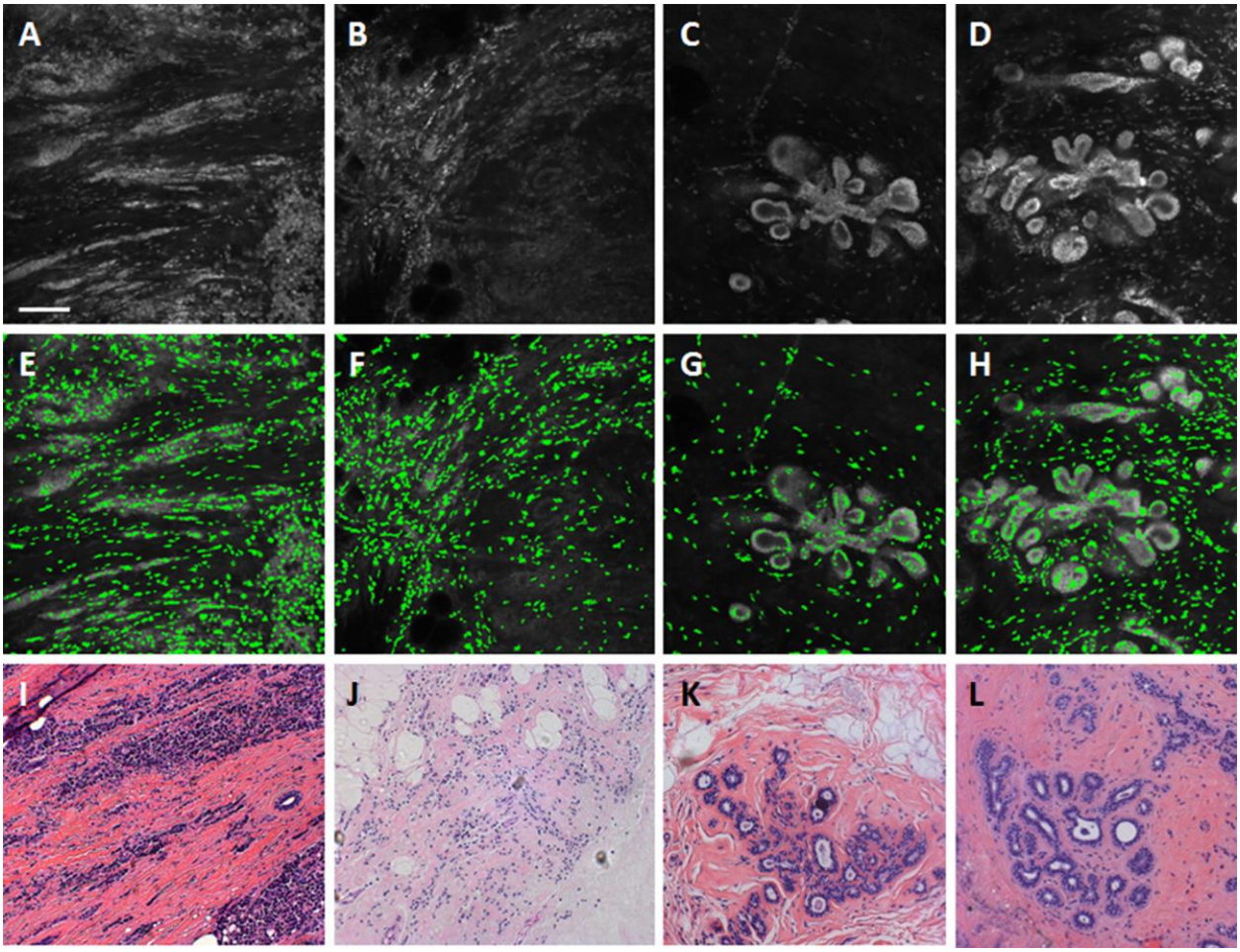

Figure 6-7: Representative images of sites with lowest classification accuracy in the decision tree model. A-D: invasive lobular carcinoma and lobules in confocal fluorescence images. E-H: Nuclei segmented by identifying maximally stable extremal regions (MSER) are false colored green and overlaid onto the raw confocal fluorescence image. I-L: Histologic slides with H&E staining show similar histology to confocal images in A-E. Slides were prepared with the same specimens from which confocal images were acquired. A, E: a true positive invasive lobular carcinoma (ILC) site; B, F: false negative ILC site; C, G: true negative lobules; and D, H: false positive lobules. Scale bar is 100 μm.

6.4 Discussion

In this study, we performed quantitative analysis of breast histology in confocal fluorescence images by designing algorithms to segment and measure nuclear and ductal parameters. We combined nuclear and ductal parameters to develop a classification tree model to classify malignant from benign changes in the breast parenchyma with 81% sensitivity and 93% specificity, which corresponded to an AUC of 0.93 and an overall accuracy of 90%. The cross-validated model classified the same sites with 75% sensitivity, 93% specificity, and 88% overall accuracy.

Several groups have used automated morphometric evaluation of nuclei in H&E stained sections of breast tissue [171-174], cytological smears of breast tissue [175], and fluorescence microscopy images of mouse tissue [179, 185] to classify benign and malignant breast features. While these groups demonstrate that quantitative nuclear parameters can be used to classify benign and malignant breast features, some lesions are more difficult to distinguish. For example, Rajesh et al used automated nuclear morphometry to classify ILC, IDC, and borderline lesions [173]. While significant differences were found between parameters measured for ILC and IDC, no significant difference was found between parameters measured for ILC and benign borderline lesions [173]. We found similar results to the other studies – namely that ILC is difficult to distinguish from non-neoplasia based on nuclear features alone. Additionally, several studies have demonstrated the feasibility of computerized image analysis to distinguish between non-hyperplastic ducts, hyperplastic ducts, and DCIS. Mayr et al used computerized image analysis to quantify ductal parameters in H&E-stained slides of breast biopsies and found that the most significant parameters for differentiation between normal ducts and DCIS were duct mean diameter and the presence of necrosis [176]. Anderson et al used a computerized segmentation

algorithm to measure parameters of ductal hyperplasia and DCIS in tissue sections stained with the antibody cocktail AE 1/3, and showed that the highest classification accuracy for DCIS was achieved by combining parameters of ducts and lumina [177]. The findings from our work agree with previous studies, which showed that quantitative ductal parameters can be used to classify benign and malignant ducts [176, 177].

The strengths of our study are that we demonstrate that nuclear and ductal parameters can be measured in confocal fluorescence images of clinical samples acquired at the point of care. We perform quantitative analysis of breast tissue architecture without requiring tissue fixation, cutting, and staining and achieve comparable classification accuracy to studies that performed computerized analysis on fixed breast tissue stained with H&E. The model classified IDC and DCIS with greater than 90% accuracy using parameters that were based on the morphological characteristics of each malignant tissue type. Specifically, IDC was classified with 92% accuracy using standard deviation in inter-nuclear distance as a parameter, which identifies dense clusters of nuclei. DCIS was classified with 96% accuracy based on the presence of more than one lumen, which is consistent with the cribriform pattern. Overall we achieve high performance (AUC = 0.93) on a large number of sites (n = 259).

There are several limitations associated with this study. While our initial data set contains a large number of sites (n = 259), the data was acquired at a single center (The University of Texas M.D. Anderson Cancer Center), and some individual categories, such as ILC contain relatively few sites (n = 17); therefore, additional work is needed with a large, independent data set composed of data from more than one center to validate the feasibility and reproducibility of these parameters. However, our initial results indicate that leave one out cross-validation of the CART model yields similar performance to the original model suggesting that our model may

generalize to an independent data set. Another limitation to the study are the large variances observed for the nuclear parameters that reflect the high degree of heterogeneity in nuclear size and spacing in benign and malignant breast epithelia. Changes in nuclear area and spacing in breast epithelia occur frequently in both ductal and lobular nuclei and can be due to a number of clinical features, including sexual maturity, pregnancy, menopausal status, use of hormonal contraceptives, and presence of mammary carcinoma [15, 188]. The presence of heterogeneity in nuclear area and distribution within benign breast tissue is a potential source of variance for the nuclear parameters measured in this study. Similarly, IDC and ILC typically contain irregular nuclear sizes and an irregular distribution of nuclei [15, 189], which is another potential source of variance within nuclear parameters. In addition, the algorithm designed for ductal segmentation uses an interactive threshold to convert images from grayscale to binary and a user-defined selection tool to isolate ducts from surrounding nuclei. The ductal segmentation process is a potential source of variability between users, particularly for parameters that could be impacted by a user's visual assessment of the duct wall boundaries, such as duct wall width. However, the ductal parameter that was ultimately selected for the decision tree model was the number of lumens, which is unlikely to vary at the decision point (number of lumens greater than 1) based on slight variations to the threshold value or by excluding surrounding nuclei. This is because it is readily apparent if a duct has one or more lumens based on visual assessment, however the segmentation algorithm could assist in identifying ducts with more than 1 lumen. Lastly, examination of the breakdown of false negatives and false positives reveals that our algorithm does most poorly at distinguishing ILC and lobule sites. Specifically 65% (n = 11 out of 17 sites) of ILC sites and 10% of lobule sites (n = 8 out of 82 sites) are incorrectly classified. Figure 6-7 reveals that there are differences in quantity and clustering of nuclei between the true

positive and false negative ILC sites. In particular, nuclei in the false negative ILC site appear to be predominately located in the upper left region of the image, suggesting that only the upper left region of the image contains ILC while the remainder of the image may contain other benign tissue. Therefore, the fraction of the image that consists of a malignant tissue type may correlate with the likelihood that it is correctly classified as a true positive site. Conversely, the false positive lobules site contains more nuclei than the true negative lobule site, particularly in stromal tissue located in between lobules. This indicates that the stromal tissue that lobules or other features are embedded within may lead to incorrect classification as a false positive site. In future studies, additional parameters are needed in order to classify lobules as benign and ILC as malignant with greater accuracy.

It is to be noted that while confocal microscopy provides high resolution high quality images, currently its cost, footprint, and maintenance requirements limit the ability to translate this imaging platform to routine usage in patient care. However, this study lays the groundwork for how quantitative analysis could be combined with proflavine staining and fluorescence microscopy. Several applications of fluorescence confocal microscopy can certainly evolve in pathology practice with the potential availability of a user friendly and affordable platform that can be an alternate to currently used modalities for immediate evaluation of fresh tissue. In addition, there could be an opportunity to use a low cost fluorescence confocal microscope to obtain similar images that may be useful to evaluate fresh tissues in clinical practices with limited resources of professional pathology expertise and laboratory infrastructure to obtain information from the biopsied tissue to guide clinical management [186, 190].

6.5 Conclusions

We measured quantitative nuclear and ductal parameter in confocal fluorescence images of proflavine stained fresh breast tissue and developed a classification algorithm that distinguished between 259 benign and malignant sites with an accuracy of 88%. Ultimately, the nuclear and ductal parameters described in this study could be used to develop criteria to automate breast lesion diagnosis for immediate evaluation of fresh tissue at the point of care obviating the need for extensive tissue preparation. Quantitative diagnostic criteria developed on fluorescence confocal images in our study have the potential to enable automated assessment of breast tissue.

7 CHAPTER 7: Confocal fluorescence microscopy to evaluate changes in adipocytes in the tumor micro-environment associated with invasive ductal carcinoma and ductal carcinoma *in situ*[4]

ABSTRACT: Adipose tissue is a dynamic organ that provides endocrine, inflammatory, and angiogenic factors, which can assist breast carcinoma cells with invasion and metastasis. Previous studies have shown that adipocytes adjacent to carcinoma, known as cancer associated adipocytes (CAAs), undergo extensive changes that correspond to an "activated phenotype," such as reduced size relative to adipocytes in non-neoplastic breast tissue. Optical imaging provides a tool that can be used to characterize adipocyte morphology and other features of the tumor microenvironment. In this study, we used confocal fluorescence microscopy to acquire images of freshly excised breast tissue stained topically with proflavine. We developed a computerized algorithm to identify and quantitatively measure phenotypic properties of adipocytes located adjacent to and far from normal collagen, ductal carcinoma *in situ* (DCIS), and invasive ductal carcinoma (IDC). Adipocytes were measured in confocal fluorescence images of fresh breast tissue collected from 22 patients. Results show that adipocytes adjacent to neoplastic tissue margins have significantly smaller area compared to adipocytes far from the margins of neoplastic lesions and compared to adipocytes adjacent to non-neoplastic collagenous stroma. These findings suggest that confocal microscopic images can be utilized to evaluate phenotypic properties of adipocytes in breast stroma, which may be useful in defining alterations in microenvironment that may aid in the development and progression of neoplastic lesions.

[4] The contents of this chapter have been submitted for peer review to the International Journal of Cancer

7.1 Introduction

The development of breast cancer is a complex process that primarily occurs in ductal and lobular epithelial tissue [22, 23]. However, many recent studies have suggested that breast stromal tissue also plays a dynamic and influential role in breast tumor development and progression [42-45], and that stromal cell proliferation is a major contributor to increased breast cancer risk [52]. Stromal collagen and adipose tissue in particular are of interest for their role in breast disease progression [46-51]. It was recently reported that high mammographic density (associated with a 4-to-6-fold increase in breast cancer risk) is associated with high collagen density [52], which has been shown to directly promote proliferation of mammary epithelial cells *in vitro* and in murine models [47].

Adipose tissue, the predominant component of benign breast tissue, also functions as a dynamic organ that assists breast carcinoma cells with invasion and metastasis by providing endocrine, inflammatory, and angiogenic factors [50, 191-193]. Previous studies have shown that co-culturing adipocytes and cancer cells results in a decrease in adipocyte markers and an overexpression of matrix metalloproteinase-11 (MMP-11), an extracellular matrix-remodeling proteinase associated with tumor invasion, and interleukin-6 (IL-6), a cytokine associated with inflammation [50]. These studies characterize the relationship between invading carcinoma cells and adipocytes surrounding carcinoma, commonly referred to as cancer-associated adipocytes (CAAs), as a crosstalk cycle, in which adipocytes undergo de-differentiation and contribute to abnormal proliferation of tumor cells, which leads to tumor growth and increased invasive potential [49, 53, 194].

Previous research on the role of CAAs and tumor progression also shows that CAAs adjacent to neoplastic tissue undergo extensive phenotypic changes, particularly reduced size relative to adipocytes in non-neoplastic breast tissue [50, 53]. Tan et al. found that adipocytes

near the invasive front of breast tumors tend to be smaller in size than those located further from the tumor [49]. Adipocytes co-cultured with breast cancer cells underwent lipolysis and developed a fibroblast-like phenotype in which the lipid vesicles greatly decreased in size and the cells took on a spindle-shaped appearance [50]. These physical changes observed in adipocytes in the tumor microenvironment correspond to an "activated phenotype" [50], which could indicate adipocytes that are participating in crosstalk with neoplastic cells and confer increased potential for invasion to the tumor microenvironment [49].

The clinical standard for evaluating breast lesions is histologic assessment, which requires extensive tissue preparation and staining with hematoxylin and eosin (H&E). However, the standard histologic preparation is not optimal for evaluation of adipose tissue, because fixation and sectioning tissue specimens can cause adipocyte cell membranes to tear and adipose tissue to slough off or dissolve. Confocal microscopy is an emerging image acquisition technique that could potentially address the current limitations of histologic assessment and has been used in several previous studies to acquire *in vivo* images [195-197] of fresh tissue specimens in real time [1, 2, 121, 137, 185]. Work from Schiffhauer et al. and Abeytunge et al. demonstrated that confocal reflectance microscopy and confocal fluorescence microscopy, can acquire images of fresh, unsectioned breast tissue that are visually similar to histologic slides with H&E staining [121, 137]. Recent studies from our group showed that confocal fluorescence microscopy images of breast tissue acquired in less than ten minutes contain sufficient detail to identify neoplasia and non-neoplasia in unsectioned breast tissue specimens [1] and to estimate tumor cellularity in core needle biopsies [2]. Currently available endomicroscopy platforms for *in vivo* imaging, such Optiscan FIVE1 (Optiscan, Melbourne, Australia) and Cellvizio® (Mauna Kea Technologies,

Paris, France), demonstrate that there is an opportunity to apply confocal microscopy for *in vivo* breast imaging in a clinical setting [195-197].

The objective of this study is to determine if confocal microscopy can identify and characterize changes in adipocyte phenotype near the margins of invasive breast cancer and pre-invasive lesions. Although the reduced size of CAAs adjacent to breast tumors has been qualitatively observed, this phenomenon has not been quantitatively evaluated. In this study we used confocal fluorescence microscopy to acquire images of adipose tissue located near neoplastic tissue as well as adipocytes near non-neoplastic collagenous stroma in fresh, unfixed breast tissue. The findings from this study support further use of confocal microscopy as a point of care tool to image breast tumors and surrounding adipose tissue and to explore whether features of adjacent adipocytes can predict the invasive potential of early breast cancers.

7.2 Materials and Methods

7.2.1 Breast tissue acquisition and preparation

Human breast tissue specimens were acquired through a protocol approved by the institutional review boards at The University of Texas MD Anderson Cancer Center and Rice University. All specimens were acquired from patients who gave informed consent to participate in the study. Patients were eligible for the study if they were undergoing a total or segmental mastectomy for breast cancer. Fresh tissue specimens were acquired from residual resected breast tissues that were not required for clinical diagnosis. Two tissue specimens measuring approximately 15 x 15 x 2-7 mm were acquired from each patient within 30 minutes of resection, including one grossly normal specimen and one grossly abnormal specimen. Each tissue specimen was stained with a solution of 0.01% proflavine in 1X phosphate buffered saline (PBS) for 1 minute, washed in 1X PBS, and then immediately imaged using a confocal fluorescence

microscope. Proflavine has been used in previous studies as a fluorescent contrast agent to stain nuclei in breast tissue, oral mucosa, esophageal tissue, cervical tissue, and sarcoma [1, 2, 102, 122, 183-186, 198, 199]. Proflavine also non-specifically stains the membranes of adipocyte cells [1], which makes it possible to identify adipocytes without using a contrast agent to stain lipid droplets.

7.2.2 Image acquisition and evaluation

Fluorescence confocal images were acquired with a benchtop confocal microscope (Vivascope 2500, Caliber I.D.). Following topical application of proflavine, specimens were positioned on the microscope stage and imaged with 2.1 ± 0.4 mW power at 488 nm laser excitation using a 30X water immersion objective lens with a numerical aperture of 0.8. The confocal microscope has a 750 x 750 μm field of view (FOV) with 1.0 μm lateral resolution and 5.0 μm axial resolution. Images were acquired at a focal plane depth approximately 20 μm beneath the tissue surface from a composite grid of contiguous sites with a total area of 12.2 x 12.2 mm [1]. Composite confocal images required approximately 10 minutes to acquire. After image acquisition, tissue specimens were submitted for routine histologic preparation and fixation with H&E staining.

A breast pathologist reviewed the confocal and H&E stained images to provide a diagnosis for each tissue specimen based on standard histologic criteria [15]. We used images with H&E staining to identify regions with adipose tissue surrounding invasive ductal carcinoma (IDC), ductal carcinoma *in situ* (DCIS), and stromal collagen with no neoplastic cells (collagen), and located the same regions in confocal images. During the pathologist's review of composite confocal images and corresponding H&E stained sections we verified that the images were acquired from the same approximate location within the specimen if they contained similar morphology. It was not possible to image the identical section of tissue with the confocal

microscope that was stained with H&E, because the specimens imaged with the confocal microscope were not sectioned; specimens were sectioned during routine histologic preparation. In confocal images, we defined regions of interest (ROIs) in confocal images consisting of two to four contiguous FOVs, originating at the margin of IDC, DCIS, or collagen without neoplasia and extending 2 - 3 mm into adipose tissue (Figure 7-1); 2 -3 mm is a narrow tumor resection margin typically used in breast-conserving surgeries [200].

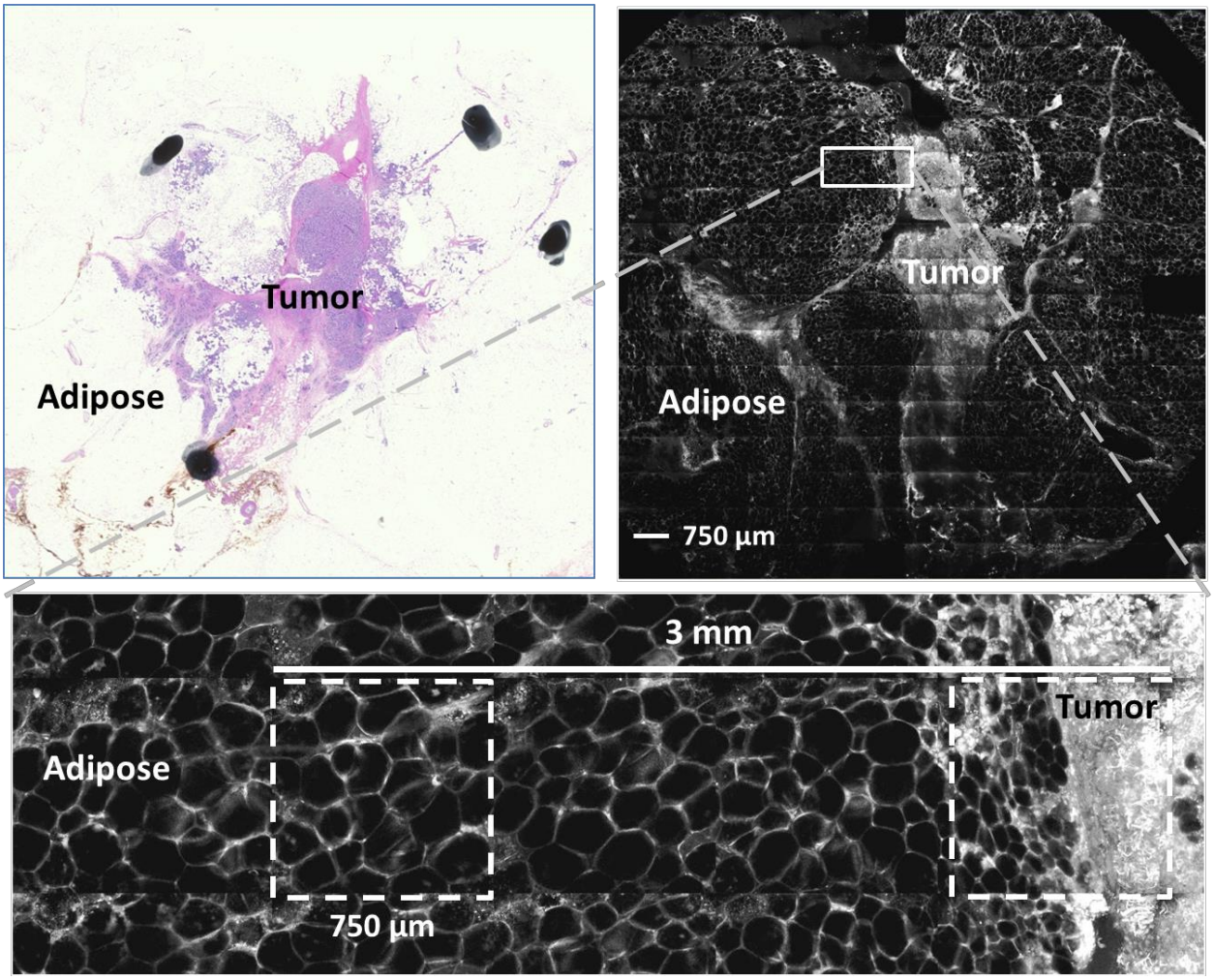

Figure 7-1: Schematic of the procedure used to identify regions of interest (ROIs) within adipose tissue at the margin of invasive tumors. Regions with adipose tissue adjacent to invasive tumors were identified in images of fixed tissue specimens stained with hematoxylin and eosin using standard histologic criteria (top left). The same regions were identified in the corresponding image acquired with confocal fluorescence microscopy (top right). White squares in upper right image indicate 4 contiguous FOVs adjacent to an invasive tumor margin. Scale bar is 750 μm. In the bottom image, boxes with dashed lines indicate four contiguous 750 x 750 μm FOVs next to the invasive tumor margin and extending up to 3 mm into adipose tissue. Scale bar is 3 mm.

7.2.3 Adipocyte segmentation algorithm and measurement of adipocyte nuclei

We developed a computerized algorithm in MATLAB® (R2011b, MathWorks®) to segment adipocytes and characterize adipocyte morphology in confocal images of breast tissue, as shown in Figure 7-2. Adaptive histogram equalization was applied to unprocessed confocal images (Figure 7-2A)to enhance the brightness of the adipocyte cell membranes (Figure 7-2B). Since proflavine preferentially stains nuclear material and does not stain lipid droplets, adipocytes appeared as unstained areas surrounded by non-specifically stained cell membranes in confocal images [1, 122]. Adipocyte membranes were detected and enhanced using a combination of two morphological operations implemented with the "bwmorph" and "imdilate" functions (Figure 7-2C). The contrast-enhanced confocal image (Figure 7-2B) was converted to a binary image with a user-defined threshold based on relative staining intensity of adipocyte cell membranes (Figure 7-2D). The resulting binary image (Figure 7-2D) was overlaid onto the adipocyte cell membranes previously segmented with a combination of morphological operations (Figure 7-2C) using a logical OR operation (Figure 7-2E). A morphological closing function (imclose) was used to dilate and then erode the image with a disk-shaped structuring element to fill the gaps where adipocyte cell membranes were incompletely segmented by the previous operations (Figure 7-2F). In order to identify adipocytes enclosed by adipocyte cell membranes, a complement function reversed the background and segmented areas (colored black and white, respectively) in the binary image (Figure 7-2G). A morphological opening function (imopen) was used to perform erosion followed by dilation with a disk-shaped structuring element to remove objects smaller than adipocytes; the structuring element was designed to remove regions that were smaller than 1.5X the area of a large mammary carcinoma cell; this area was 338 μm , slightly larger than the size of a large epithelial cell within mammary carcinoma [188] (Figure

7-2H). To avoid measuring areas of adipocytes which were cut off by the border of the FOV, an image processing function (imclearborder) was applied to delete objects connected to the borders of the image (Figure 7-2I). Following segmentation of adipocytes, an ellipse was fitted to each adipocyte to approximate its cross-sectional area. The mean ellipse area was calculated for each consecutive FOV in ROIs.

The adipocyte segmentation algorithm was modified to segment adipocytes in histologic images with H&E staining. Unlike in confocal images, in which adipocytes appear as dark, unstained areas, adipocytes in digital images of histologic slides appear as white areas unstained by H&E. Thus, in the modified algorithm adipocytes were identified as areas with higher signal. The complement function described in the first iteration was omitted, because cell membranes stained with H&E already had lower signal than the lipid droplets.

After processing, each FOV was manually reviewed to determine if the algorithm accurately segmented adipocytes compared to visual examination. We developed additional manual interactive functions to improve segmentation of individual adipocytes that were not accurately identified by the algorithm. For example, in FOVs with very weakly-stained cell membranes, clusters of cells were occasionally incorrectly segmented as a single adipocyte. Additionally, out of focus cell membranes in a FOV sometimes caused an individual adipocyte to be separated into multiple fragments. In these cases, the interactive functions were used to separate clusters of cells into individual adipocytes or to connect fragments of a cell into a single adipocyte. All FOVs required manual adjustment to improve segmentation accuracy for at least one adipocyte.

We compared the morphology of adipocytes at the margins of IDC and DCIS to those extending into surrounding stroma. We also compared the morphology of adipocytes at these ROIs to adipocytes surrounding stromal collagen in areas that did not contain neoplasia. Statistical comparisons were made using an ANOVA test with a Bonferroni-Holm post-hoc test.

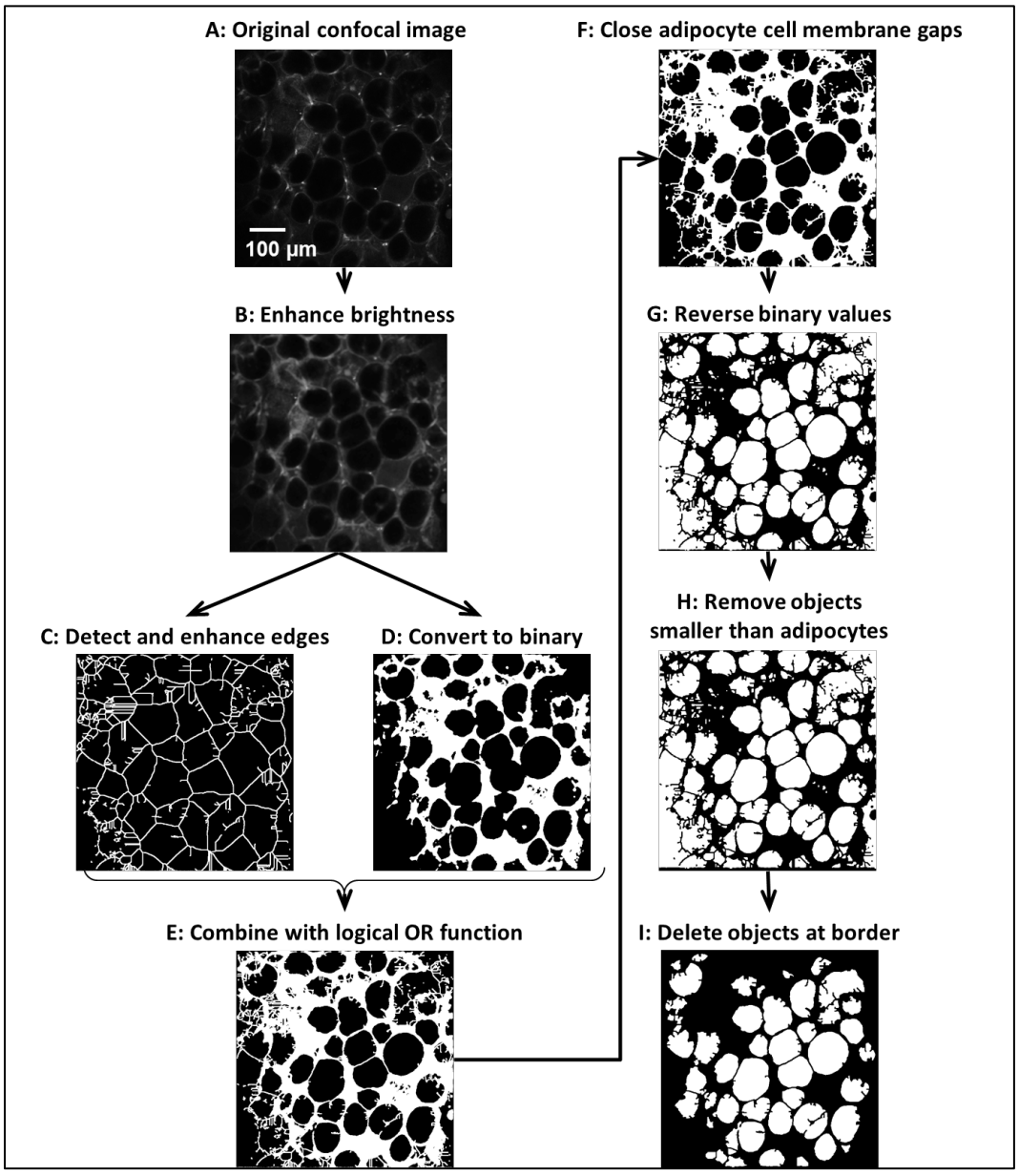

Figure 7-2: Adipocyte segmentation algorithm. A: Original confocal fluorescence image. B: Adaptive histogram equalization to enhance brightness of adipocyte cell membranes. C: Adipocyte cell membrane edges detected and enhanced. D: Image A is converted to binary. E: Binary image D and enhanced edges in image C are combined. F: Closing function is applied to fill gaps in adipocyte cell membranes. G: Background (black) and segmented areas (white)

are reversed to create the complement of F. H: Opening function is applied to remove objects smaller than 1.5X the area of a large mammary carcinoma cell. I: Objects touching the image border are removed. Scale bar is 100 μm.

7.3 Results

Adipocytes were measured in 427 FOVs within 116 ROIs in composite confocal fluorescence images of breast tissue specimens collected from 22 patients. A summary of FOVs, ROIs, patients and diagnoses are shown in Table 7-1. Each FOV required approximately 20 minutes for adipocyte segmentation with the computerized algorithm and manual functions.

Table 7-1: Summary of patients from which tissue specimens were acquired and regions of interest (ROIs) adjacent to lesion margins consisting of 2-4 contiguous FOVs, with corresponding histologic diagnoses.

Diagnosis	Patients	ROIs	FOVs
IDC	22	54	187
DCIS	2	9	31
Collagen	22	53	209
All	22	116	427

Figure 7-3 shows representative ROIs that consist of 4 contiguous FOVs from specimens with IDC (Figure 7-3A), DCIS (Figure 7-3B), and collagen in a non-neoplastic region (Figure 7-3C). FOVs labeled with I are located adjacent to IDC, DCIS, or collagen; the adjacent sets of contiguous FOVs (Figure 7-3A-C: II-IV) extend into adipose tissue. FOVs labeled with IV are located between 2 and 3 mm from the lesion edge (Figure 7-3A-C:I) and represent a theoretical narrow resection margin [200]. Figure 7-3D shows mean adipocyte ellipse area measured in each FOV (Figure 7-3A-C) using the segmentation algorithm. Adipocytes in FOVs adjacent to IDC and DCIS (Figure 7-3A,B: I; Figure 3D) have a mean area of approximately 5,000 μm , while adipocytes in the FOV adjacent to benign collagen (Figure 7-3C) have a mean area of approximately 9,000 μm . Mean adipocyte area increases to over 24,000 μm in FOVs 2-3 mm from the margin of the IDC lesion and to 12,000 μm for the DCIS lesion (Figure 7-3A,B: II-IV;

Figure 7-3D). In contrast, mean adipocyte area stays relatively constant over the distance from the interface with collagen in the non-neoplastic region.

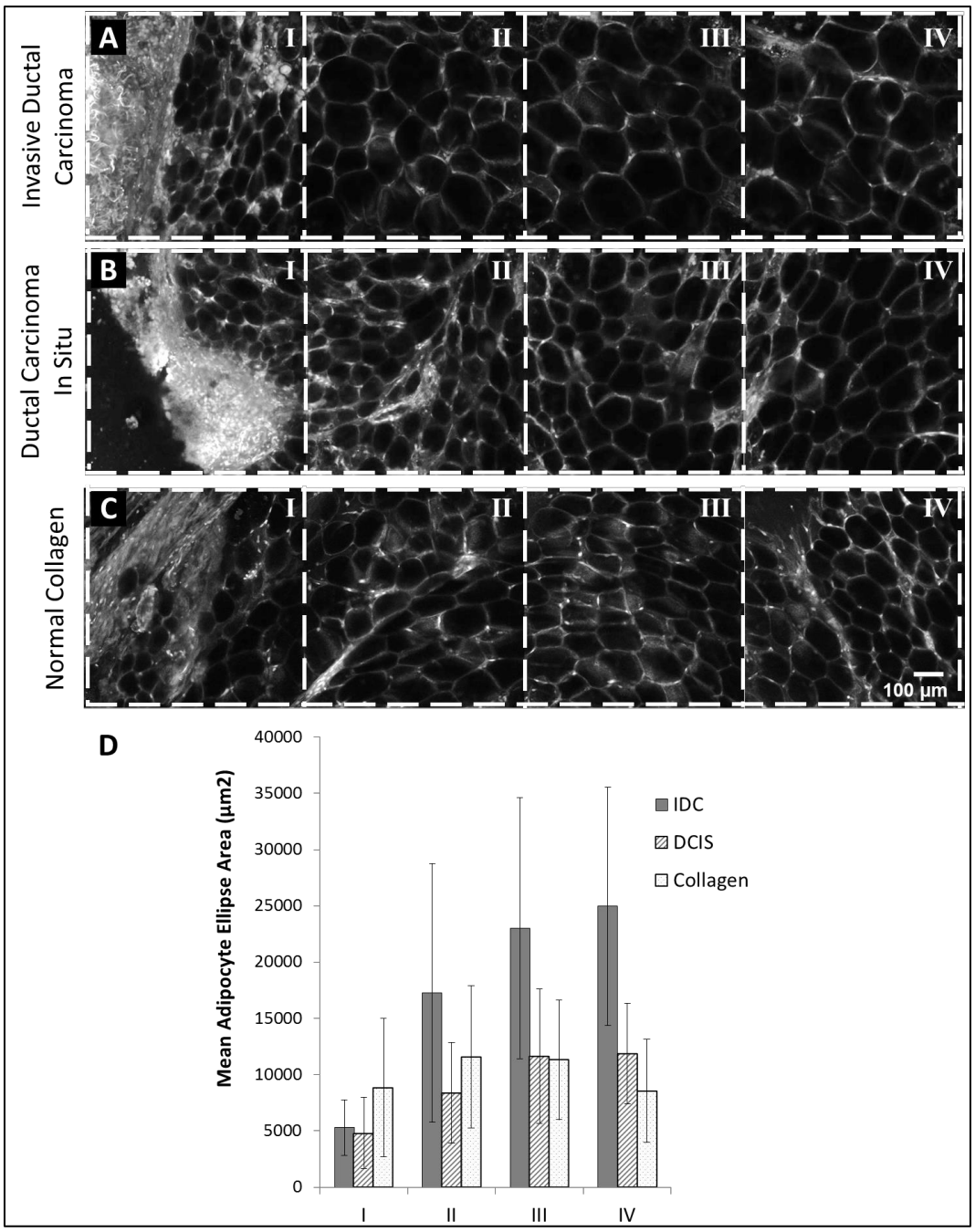

Figure 7-3: Representative regions of interest (ROIs) consisting of 4 contiguous FOVs located adjacent to the margins of invasive ductal carcinoma (A), ductal carcinoma *in situ* (B), and benign collagen (C). I: 750 x 750 *µ*m FOVs located adjacent to non-adipose tissue margins. II-IV: contiguous FOVs extending up to 3 mm into adipose tissue. Scale bar is 100 *µ*m. (D) Mean adipocyte ellipse area measured for each FOV shown above using the adipocyte segmentation algorithm.

Figure 7-4 shows the mean adipocyte area versus distance from the margin for all 427 FOVs. Figure 7-4A shows that on average adipocytes adjacent to the margin of IDC are smaller than those adjacent to benign collagen, whereas the mean size of adipocytes is similar at 2-3 mm from the margin. Although the number of samples is smaller, a similar trend is seen for DCIS, with small adipocytes near the margin, increasing in size at 2-3 mm distant from the margin. Figure 7-4B shows the same mean adipocyte area versus distance from the margins, but data have been normalized by the mean value from the FOV immediately adjacent to IDC, DCIS, and benign collagen. Adipocytes show the greatest increase in mean area in FOVs identified in IDC specimens: adipocytes in contiguous FOVs extending into adipose tissue have an average of 1.8X (range: 0.77-6.4X) the mean area of adipocytes in FOVs adjacent to IDC margins (Figure 7-4B). In tissue with DCIS, adipocytes in FOVs extending into adipose tissue have an average of 1.6X (range: 0.86-2.5X) the mean area of adipocytes in FOVs adjacent to DCIS margins. In benign stroma, adipocytes in FOVs extending into adipose tissue have an average of 1.3X (range: 0.21-3.8X) the mean area of adipocytes in FOVs adjacent to benign collagen.

Figure 7-4C shows box and whiskers plots summarizing the distribution of mean adipocyte ellipse area in FOVs versus distance from the margin. Significant differences in mean area identified with an ANOVA test and a Bonferroni-Holm post-hoc test are identified with asterisks (*) and the dagger symbol (†). Adipocytes in FOVs adjacent to IDC and DCIS have significantly lower mean area than adipocytes in FOVs adjacent to benign collagen ($p < 0.001$ and $p < 0.05$, respectively). There was no significant difference in mean area between adipocytes measured 2-3 mm away from benign collagen and IDC or between adipocytes 2-3 mm from benign collagen and DCIS. In addition, adipocytes in FOVs adjacent to margins of IDC or DCIS have significantly lower mean area than in FOVs located further from the associated lesion

margins (2.2X-fold increase in area corresponding to $p < 0.001$ for IDC, 2.0X-fold increase in area corresponding to $p < 0.001$ for DCIS). Adipocytes in FOVs adjacent to benign collagen also have significantly lower mean area than adipocytes 2-3 mm into adipose tissue (1.2X-fold increase in area corresponding to $p < 0.01$).

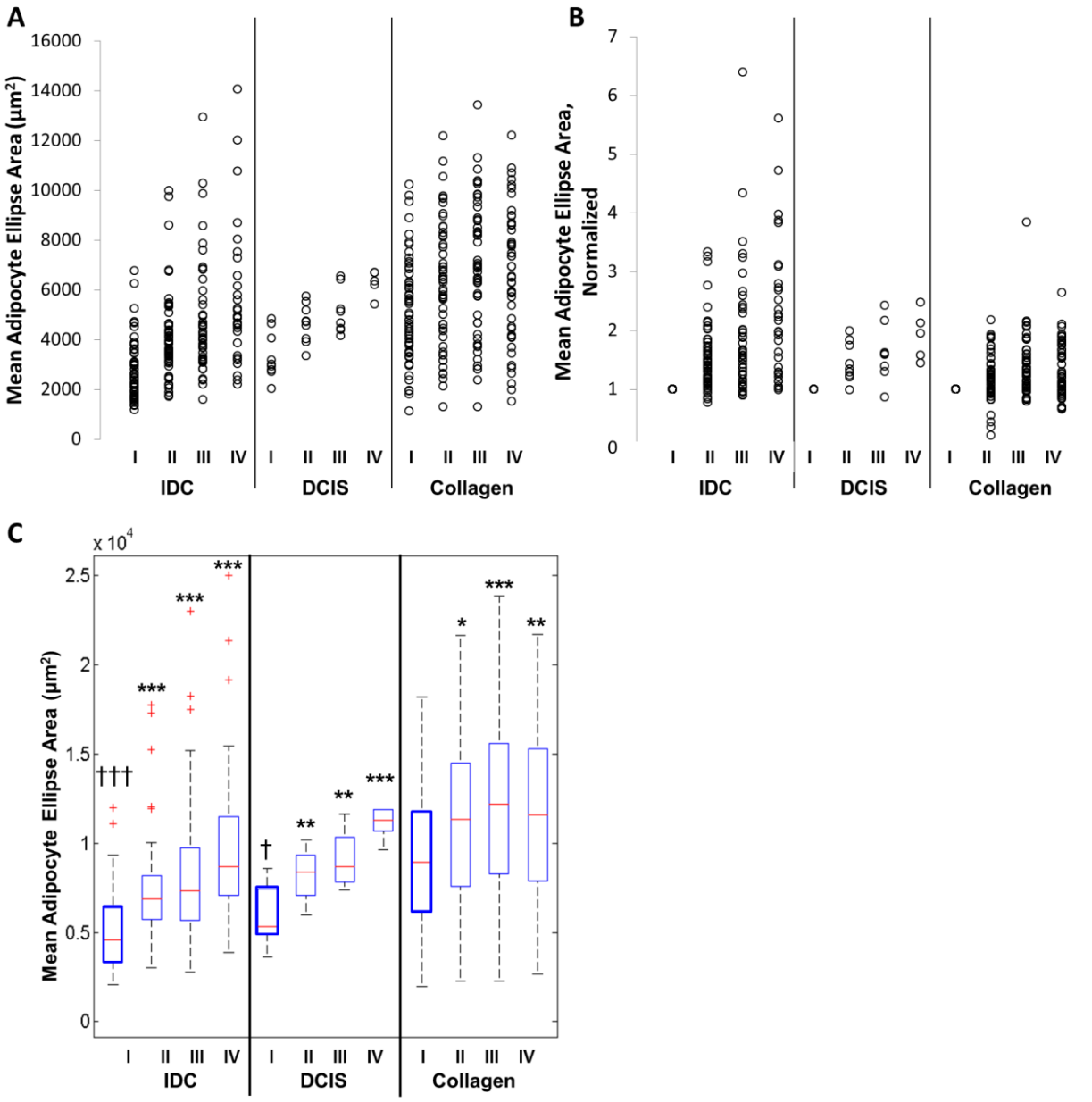

Figure 7-4: A: Mean adipocyte ellipse area measured for each FOV, measured adjacent to the lesion edge (I) and extending into adipose tissue (II-IV) for tissue adjacent to IDC, DCIS and benign collagen. B: Mean adipocyte ellipse area measured for each FOV extending into adipose tissue (II-IV), normalized to the FOV adjacent to the lesion edge (I); ellipse area measured in tissue adjacent to IDC, DCIS and benign collagen. C: Box and whiskers plot showing mean adipocyte ellipse area, measured adjacent to the lesion edge (I) and extending into adipose tissue (II-IV), for ROIs adjacent to IDC, DCIS, and benign collagen. Asterisks (*) above the boxes indicate significant differences between the mean ellipse area measured for the site adjacent to the lesion edge (I) and sites extending into adipose tissue (II-IV); * = $p < 0.05$; ** = $p < 0.01$; *** = $p < 0.001$. The symbols (†) indicate significant differences between the mean ellipse area measured in sites adjacent to collagen compared to sites adjacent to IDC and DCIS (††† = $p < 0.001$).

The segmentation algorithm was adapted to identify and measure parameters of adipocytes in histologic images with H&E staining. Figure 7-5 shows representative FOVs in histologic slides and confocal images identified at the same approximate location within a breast tumor specimen, adjacent to the tumor edge (Figure 7-5 A,C) and 2 mm from the tumor edge (Figure 7-5 B,D). The top row of Figure 5 shows the original histologic and confocal images and the bottom row shows images following application of the segmentation algorithm. The box and whiskers plot (Figure 7-5 E) compares adipocyte ellipse area measured in the FOVs shown in Figure 7-5 A-D. Adipocyte area is not significantly different between the histologic and confocal images adjacent to the tumor center. In both histologic and confocal images adipocyte area is significantly smaller adjacent to the tumor edge than 2 mm from the tumor edge.

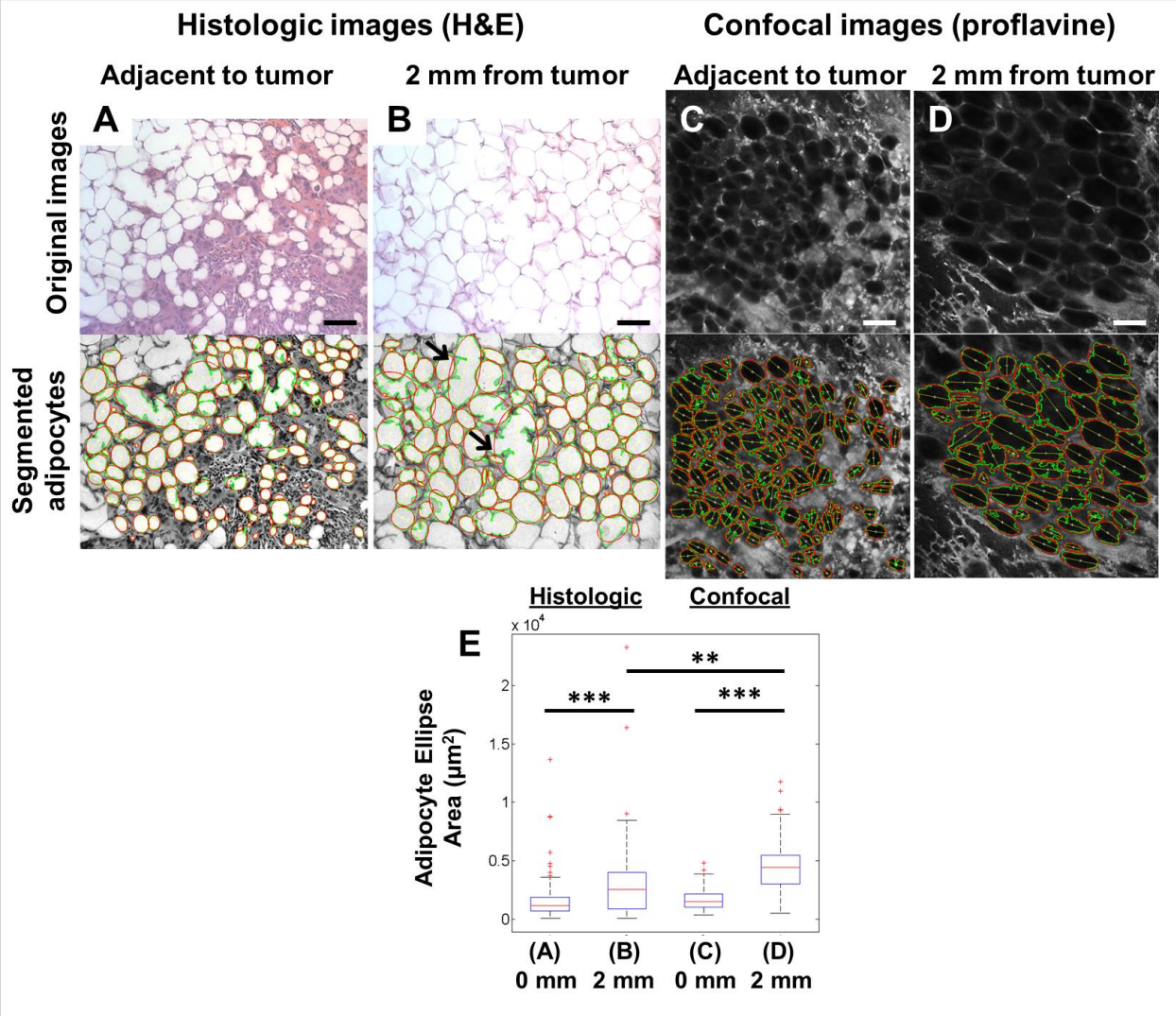

Figure 7-5: Adipocytes segmented in histologic slides with H&E staining (A,B) and confocal images of tissue stained with proflavine (C,D). FOVs in histologic and confocal images were identified at the same approximate locations within a breast tissue specimen. FOVs show adipocytes adjacent to the tumor edge (A,C) and a distance of 2 - 3 mm from the tumor edge (B,D). Arrowheads indicate adipocytes with torn cell membranes. The boxplot shows adipocyte ellipse area measured at FOVs shown in A-D (E). The FOV corresponding to each box and the location of the FOV relative to the tumor edge is indicated below the plot. Scale bars are 100 μm.

7.4 Discussion

In this study, we developed a computerized algorithm to identify and quantitatively characterize adipocytes in confocal fluorescence microscopy images of fresh breast tissue. Images were acquired from fresh breast tissue prior to standard histologic preparation and fixation and the algorithm was used to analyze characteristics of adipocytes at sites adjacent to

and far from lesion margins in neoplastic and non-neoplastic tissue. We found that adipocytes adjacent to neoplastic tissue margins are significantly smaller in area compared to adipocytes far from the margins of neoplastic lesions and compared to adjacent to non-neoplastic collagenous stroma. Applying the segmentation algorithm to representative ROIs in histologic and confocal images shows that there is no significant difference in mean adipocyte area adjacent to the tumor edge, and that the adipocyte size increases significantly 2 mm away from the tumor edge. However, confocal images showed a greater increase in adipocyte size than did H&E stained histologic slide; this could be a result of differential tissue shrinkage following fixation.

Our observations are consistent with previous studies of histologic images of breast lesions by Tan et al. and Dirat et al., which have qualitatively observed that adipocytes adjacent to neoplastic breast lesions show phenotypic changes, such as smaller area [49, 50]. These studies also suggest that adipocytes adjacent to neoplastic breast lesions are elongated in shape; although we measured cell eccentricity as a metric of adipocyte shape, we did not observe significant differences in adipocyte shape adjacent to neoplastic or non-neoplastic lesions.

A strength of our study is that we demonstrate that adipocytes can be evaluated in confocal fluorescence images of fresh tissue specimens. Early computational methods to approximate adipocyte cross-sectional area include manual cell counting and measurements from cell suspensions and H&E stained histologic sections [201, 202]. Additionally some previous studies have demonstrated automated algorithms for adipocyte segmentation in cell suspension and H&E-stained histologic slides [203-205]. Björnheden et al. developed a method to determine human adipocyte size in a cell suspension [203]. Chen et al. and Osman et al. demonstrated automated computerized methods to determine adipocyte size in histologic slides of murine tissue or human tissue. Both studies describe automated algorithms using image processing

software to measure cross-sectional area of adipocytes [204, 205], which used similar functions to those incorporated in the algorithm described in this study. In our study we evaluated adipocyte cross-sectional area in fresh tissues, which did not undergo fixation and preparation that could alter adipocyte phenotype. This algorithm could potentially be used to segment adipocytes in images covering a larger field of view, provided that images had sufficient resolution for adipocyte membranes to be identified. While frozen section and touch preparation are currently used to prepare tissue for evaluation, these techniques can cause distortion of breast tissue specimens with adipose tissue, particularly in cases in which core needle biopsies are obtained. Damage to adipocyte cell membranes can also occur during routine histologic preparation and fixation prior to H&E staining; for example, torn cell membranes are indicated by the arrowheads in Figure 7-5B.

This study has some limitations. The computerized algorithm incorporates a user-defined threshold to convert images to binary in order to segment and measure adipocytes. The variable threshold was needed to account for differences in fluorescence intensity, which are based on several factors, including the variation in illumination power used for image acquisition and the presence of background fluorescence from out of focus signal. Additionally the histologic types of breast malignancies represented in this study only included IDC and DCIS and there were very few tissue specimens acquired from patients with DCIS lesions. Future studies should investigate adipocyte phenotype adjacent to a greater variety of breast malignancies. In this study tissue collection was limited to malignant tissue and specimens consisting of predominantly adipose tissue. Future studies could also be performed with a greater focus on adipocyte phenotype adjacent to benign proliferative lesions, such as sclerosing adenosis and reactive

changes at biopsy sites. Additional work is also needed to elucidate the molecular basis for the changes in adipocyte characteristics associated with IDC and DCIS observed in this study.

Our findings support previous observations that there is a change in adipocyte phenotype at the margins of neoplastic breast lesions, including IDC and DCIS [49, 50]. We demonstrate that adipocyte parameters could potentially characterize the microenvironment of early neoplastic breast cancers and suggest potential for lesion growth and local invasion. However, additional work is needed to analyze adipocyte phenotypes in breast tissue acquired from a larger cohort of patients and in a wider range of neoplastic and non-neoplastic breast lesions.

8 CHAPTER 8: High Resolution Microendoscopy with Structured Illumination and Lugol's Iodine Staining for Evaluation of Breast Cancer

ABSTRACT: Intraoperative margin assessment to evaluate resected tissue margins for neoplastic tissue is performed to prevent reoperations following breast-conserving surgery. High resolution microendoscopy (HRME) can rapidly acquire images of fresh tissue specimens, but is limited by low image contrast in tissues with high optical scattering. In this study we evaluated two techniques to reduce out-of-focus light: HRME image acquisition with structured illumination (SI-HRME) and topical application of Lugol's Iodine. Fresh breast tissue specimens from 19 patients were stained with proflavine alone or Lugol's Iodine and proflavine. Images of tissue specimens were acquired using a confocal microscope and an HRME system with and without structured illumination. Images were evaluated based on visual and quantitative assessment of image contrast. The highest mean contrast was measured in confocal images stained with proflavine. Contrast was significantly lower in HRME images stained with proflavine; however, incorporation of structured illumination significantly increased contrast in HRME images to levels comparable to that in confocal images. The addition of Lugol's Iodine did not increase mean contrast significantly for HRME or SI-HRME images. These findings suggest that structured illumination could potentially be used to increase contrast in HRME images of breast tissue for rapid image acquisition.

8.1 Introduction

The clinical standard to manage early stage breast cancers is surgical excision in breast conserving surgery. After surgical excision, positive margin status is an indicator increased risk of local tumor recurrence [206-208]. Current techniques to intraoperatively evaluate margins of excised specimens include touch preparation cytology and frozen section analysis [152-154, 209]. However, touch preparation does not preserve cell orientation and arrangement relative to the lesion or microenvironment in excised specimens [144]. Frozen section has the potential to lose or damage valuable tissue during rapid freezing and cutting required to prepare slides [113, 155]. The need for new imaging methods to intraoperatively evaluate margins of breast tumors has motivated several studies evaluating potential techniques, including optical coherence tomography (OCT), radiofrequency spectroscopy, and intraoperative ultrasound [91, 93, 94, 155, 156]. Several studies have shown that confocal microscopy could potentially be used to rapidly evaluate breast tissue specimens intraoperatively [1-3, 121, 137]. However, confocal microscopy systems are generally too expensive for breast tissue imaging settings with limited economic or personnel resources.

High resolution microendoscopy (HRME) is a low cost tool that can be used to acquire images of unfixed tissue [138, 181, 182, 184, 210], but it can be limited by high background signal in tissues with high optical scattering [108, 186]. A previous study showed that using structured illumination can be used to reduce background light in images acquired with an HRME system [105]. Several studies have also demonstrated that incorporating structured illumination into the HRME system has the potential to improve image quality and enhance recognition of architectural features in murine mammary glands and in human tissues with cervical cancer [107-109, 186]. Another approach to absorb out-of-focus light is application of

Lugol's Iodine, which is used as a topical antiseptic in clinical cervical cancer imaging [211, 212]. Numerous *in vitro* and *in vivo* studies have shown that Lugol's Iodine can assist with differentiation between neoplastic and non-neoplastic cells in cervical, oral, and esophageal sites [211-219].

The objective of this study was to evaluate microendoscopy with structured illumination and Lugol's Iodine as methods to improve contrast in HRME images of fresh breast tissue. We evaluated images based on visual assessment of breast architectural features and on quantitative measurement of image contrast to determine if image acquisition with structured illumination and topical application of Lugol's Iodine improve image contrast. Our findings indicate that HRME with structured illumination (SI-HRME) yields images with significantly higher contrast relative to images acquired using HRME with standard illumination. Visual assessment of HRME and SI-HRME images of neoplastic tissue indicated that topical application of Lugol's Iodine reduced background fluorescence. However, application of Lugol's Iodine did not significantly increase mean contrast in HRME or SI-HRME images. Additional studies with larger numbers of patients are needed to validate SI-HRME to determine if images acquired with this illumination technique contain sufficient information to identify neoplastic breast lesions.

8.2 Materials and Methods

8.2.1 Tissue acquisition and preparation

Human breast tissue specimens were acquired through a protocol approved by the institutional review boards at M.D. Anderson Cancer Center and Rice University. Patients were eligible to participate in the study if they provided informed consent and were undergoing surgery to remove breast cancer. Breast tissue specimens (approximately 1.5 x 1.5. x 0.8 mm)

were selected from regions of grossly normal- and abnormal-appearing tissue within 30 minutes of resection.

Prior to imaging, all breast tissue specimens were stained with proflavine, a contrast agent that stains cell nuclei, which was topically applied as a 0.01% solution in 1x (phosphate-buffered saline) PBS for 1 minute followed by a wash with 1x PBS. Breast tissue was stained with proflavine alone at 57 sites and with Lugol's Iodine and proflavine at 13 sites. Following application of proflavine, a solution of 2% Lugol's Iodine was applied to human breast specimens through a transfer pipette followed by a wash with 1x PBS. Proflavine was re-applied after staining with Lugol's Iodine to increase the intensity of fluorescence signal from epithelial cell nuclei.

Application of Lugol's Iodine, a topical antiseptic that has been shown to stain non-neoplastic tissues a dark brown color [213], was evaluated as an approach to improve image contrast by reducing transmission of out-of-focus light. In order to determine an appropriate concentration of Lugol's Iodine, we tested different concentrations ranging from 1 to 5% using murine mammary glands. Visual assessment of HRME and SI-HRME images of murine mammary glands stained with proflavine and Lugol's Iodine indicated that a concentration of 2% Lugol's Iodine provided the best balance between improvement in image contrast and reduction in proflavine intensity (data not shown).

8.2.2 Image acquisition: confocal fluorescence microscope, HRME, SI-HRME

At each site, a corresponding set of images was acquired with the confocal microscope and the microendoscopy system with and without structured illumination (SI-HRME and HRME images, respectively). Confocal fluorescence images were acquired of tissue specimens stained with proflavine. Confocal images were used to identify potential sites of interest, to guide fiber

optic probe placement for image acquisition with the combined HRME and SI-HRME system, and as a benchmark for image contrast attainable with the microendoscope system. High resolution microendoscopy (HRME) images and HRME images with structured illumination (SI-HRME) were acquired following confocal image acquisition of proflavine-stained breast specimens and in a subset of samples again after application of Lugol's Iodine. During Lugol's Iodine application and re-application of proflavine, the fiber optic probe was retracted and held stationary above the imaging site, and then the probe was lowered to acquire HRME and SI-HRME images at the same site as the previously acquired pair of images.

Confocal fluorescence images were acquired from all human breast specimens using a scanning confocal microscope (Vivascope 2500®; Caliber Imaging and Diagnostics Inc., Rochester, New York) as described previously [1-3]. After topical application of proflavine, each specimen was positioned on the confocal microscope stage and imaged at 2.1 ± 0.4 mW at 488 nm laser excitation with a 550 ± 44 nm bandpass filter through a 30X water immersion lens (numerical aperture = 0.8). At the center of each 750 x 750 μm field of view, the lateral resolution of confocal images is 1.0 μm and axial resolution is 5.0 μm. The microscope acquired images in a grid pattern, and images were assembled into a 12.2 x 12.2 mm composite image following acquisition.

We used a compact, high resolution microendoscopy system (HRME) that can employ structured illumination (SI-HRME) [107, 108] to acquire HRME and SI-HRME images of sites within tissue specimens. The HRME/SI-HRME system incorporates a 10 lp/mm grid, condenser lens, and motorized translation stage into the previously described HRME system [99-102, 122, 138, 181, 210]. During HRME image acquisition, when the 10 lp/mm grid is outside the optical path, images have 4.0 μm lateral resolution and 120 μm predicted axial response based on an

experiment measuring the decrease in mean signal intensity as a function of the distance between the fiber bundle and fluorescence source [108, 190]. During SI-HRME image acquisition, the stage holding the 10 lp/mm grid is shifted in front of the optical path and a grid is projected onto the fiber bundle in steps of 1/3 period, giving SI-HRME images 4.0 μm lateral resolution and 70 μm predicted axial response [108, 190]. The hardware and software for image acquisition in the HRME/SI-HRME system are synchronized using a custom LabVIEW program, which provides controls for user-defined exposure, gain, and file saving. The speed of image acquisition is reliant on the frame rate of the camera; the maximum frame rate is 11 FPS for HRME images and 3 FPS for SI-HRME images. The fiber optic probe was placed at a selected site and held stationary during HRME and SI-HRME image acquisition. Following image acquisition, breast tissue specimens were submitted for standard fixation and histologic slide preparation with hematoxylin and eosin (H&E) staining to serve as a reference standard for histologic diagnosis.

8.2.3 Evaluation of HRME, SI-HRME, and confocal images

HRME and SI-HRME images were visually compared to confocal images and sites with similar architectural features within histologic images acquired from the same specimens. A board-certified breast pathologist assigned a diagnosis by viewing histologic slides of specimens stained with H&E on a conventional light microscope. The pathologist then verified that images acquired with optical imaging modalities showed similar image morphology to histologic images by viewing composite confocal, HRME, and SI-HRME images on a computer monitor.

To compare contrast in images acquired with HRME and SI-HRME using Lugol's Iodine and proflavine, we calculated image contrast for each image. Confocal fluorescence image were used as a reference standard. HRME and SI-HRME images were cropped to a 560 x 560 μm ROI; the largest maximum square area that could fit within the circular fiber bundle. Confocal

images were also cropped to a 560 x 560 μm ROI. Contrast was calculated from gray-level co-occurrence matrices (GLCMs), a commonly used tool to characterize image texture based on spatial relationships between pairs of pixels [220]. Contrast describes the difference in pixel intensity between neighboring elements:

$$\sum_{i,j=0}^{N-1} P_{ij}(i-j)^2$$

in which *j* and *j* specify location within the GLCM and *Pij* is the intensity level of the element at *i*,*j*. *N* specifies the number of grayscale intensity levels; between 2 to 256 for an 8-bit image. When contrast is equal to 0, the elements within the GLCM have constant intensity. HRME and SI-HRME images were filtered with a Gaussian low pass filter in order to remove the fiber bundle pattern projected onto the images. Pairs of pixels were evaluated over an offset of 14 pixels, which corresponds to 10 μm, the average diameter of a non-neoplastic breast cell nucleus [188]. In order to accurately compare contrast between images that had been acquired with different levels of laser power, the mean intensity for all HRME, SI-HRME, and confocal images was normalized to 50 (on an intensity scale of 0 to 255 for 8-bit images). In order to compare relative values of contrast between imaging modalities and contrast agents applied, GLCM-based contrast measurements were normalized to the maximum value of contrast measured. The same normalization was applied to images acquired with all imaging modalities and contrast agents. ANOVA was performed to evaluate equal variance and a Bonferroni—Holm posthoc test was performed to analyze differences between mean values of GLCM-based contrast for HRME, SI-HRME, and confocal images.

8.3 Results

Human breast tissue samples were collected from a total of 19 patients, and matching histologic features were identified in sets of HRME, SI-HRME, and confocal images acquired at 70 sites (Table 8-1). Non-neoplastic tissue was identified in 47 sites, which included adipose and fibrous tissue, lobules, and benign phyllodes, a benign cytosarcoma lesion. Neoplastic tissue was identified in 23 sites, and diagnoses included ductal carcinoma *in situ* (DCIS) and invasive ductal carcinoma (IDC).

Table 8-1: Summary of sites and proflavine-stained tissue types evaluated in HRME, SI-HRME, and confocal images

Patients	19
Sites	70
proflavine only	57
Lugol's Iodine and proflavine	13
Non-neoplastic tissue	Sites: 47
Adipose tissue	19
Fibrous tissue	17
Lobules	10
Benign phyllodes	1
Neoplastic	Sites: 23
Ductal carcinoma in situ (DCIS)	3
Invasive ductal carcinoma (IDC)	20

Figure 8-1 shows representative neoplastic and non-neoplastic breast features in HRME, SI-HRME, confocal fluorescence images, and conventional histologic slides with H&E staining. The top row of Figure 8-1 shows images of adipose tissue containing a blood vessel; the blood vessel can be recognized in all imaging modalities. The second row of Figure 8-1 shows images of lobules, which are not recognizable in the HRME image, but can be identified in the SI-HRME and confocal images based on relatively small nuclear size and distinct acini [1]. The third row of Figure 8-1 shows images of DCIS. While there is too much out-of-focus light to recognize DCIS in the HRME image, the SI-HRME and confocal images of DCIS show enlarged

nuclei within a circular area, which are indicative of *in situ* carcinoma. The fourth row of Figure 8-1 shows images of IDC. As in the images of DCIS, there is too much out of focus light in the HRME image to recognize IDC, while the SI-HRME and confocal images show enlarged nuclei arranged in disorganized clusters, suggestive of invasive carcinoma [1]. In the SI-HRME images of lobules, DCIS, and IDC there is a visually apparent reduction in background light relative to HRME images, which makes these features visually comparable to the corresponding confocal and histologic images. Incorporating structured illumination improves visual assessment of sites with dense nuclei, such as lobules, DCIS, and IDC.

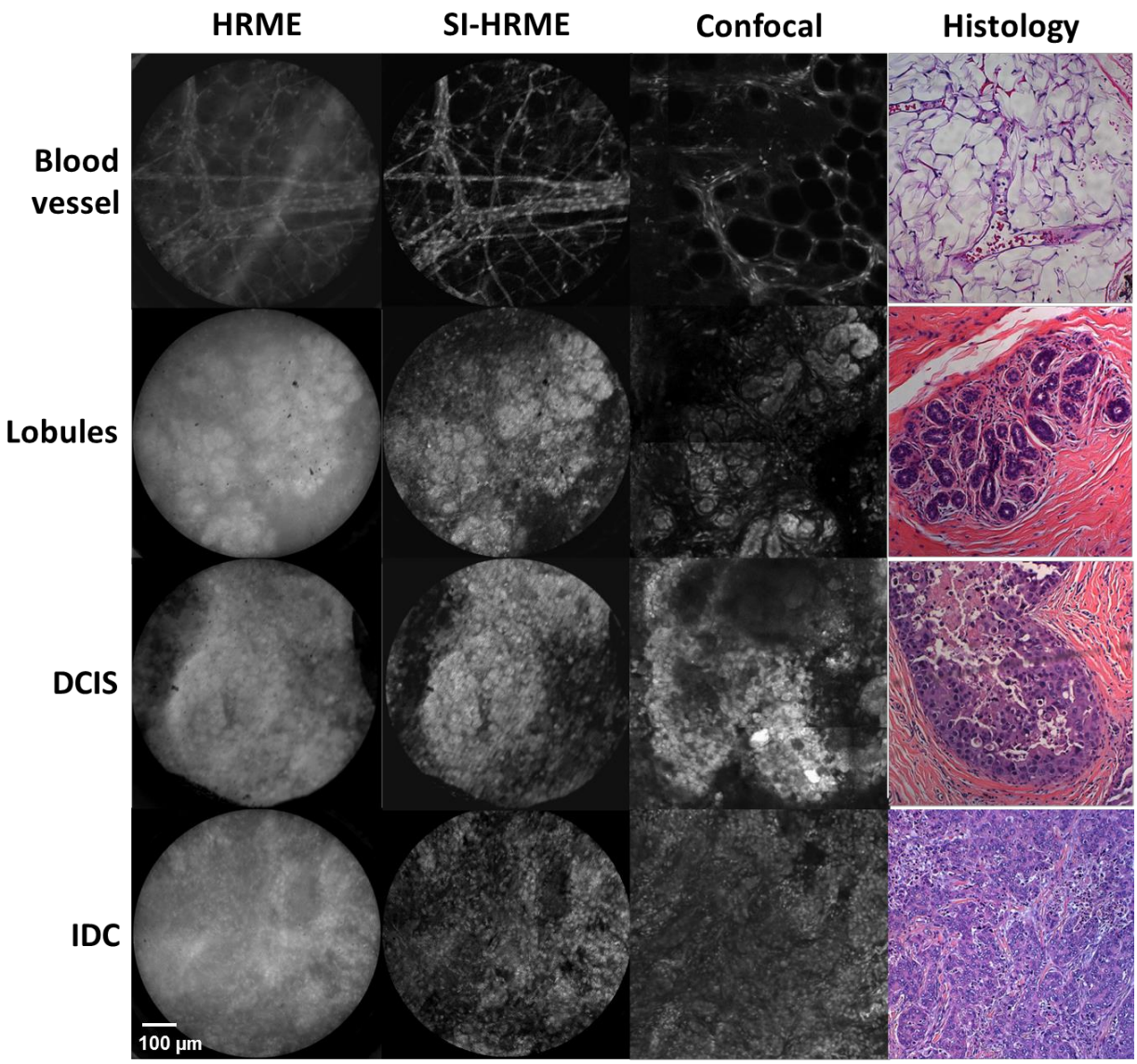

Figure 8-1: Non-neoplastic and neoplastic features imaged with HRME, structured illumination HRME, confocal fluorescence microscopy, and histology with H&E staining. Non-neoplastic features shown are blood vessels (top row) and lobules (second row). Neoplastic features shown are cribriform pattern DCIS (third row) and invasive ductal carcinoma (fourth row). Scale bar is 100 μm for all images.

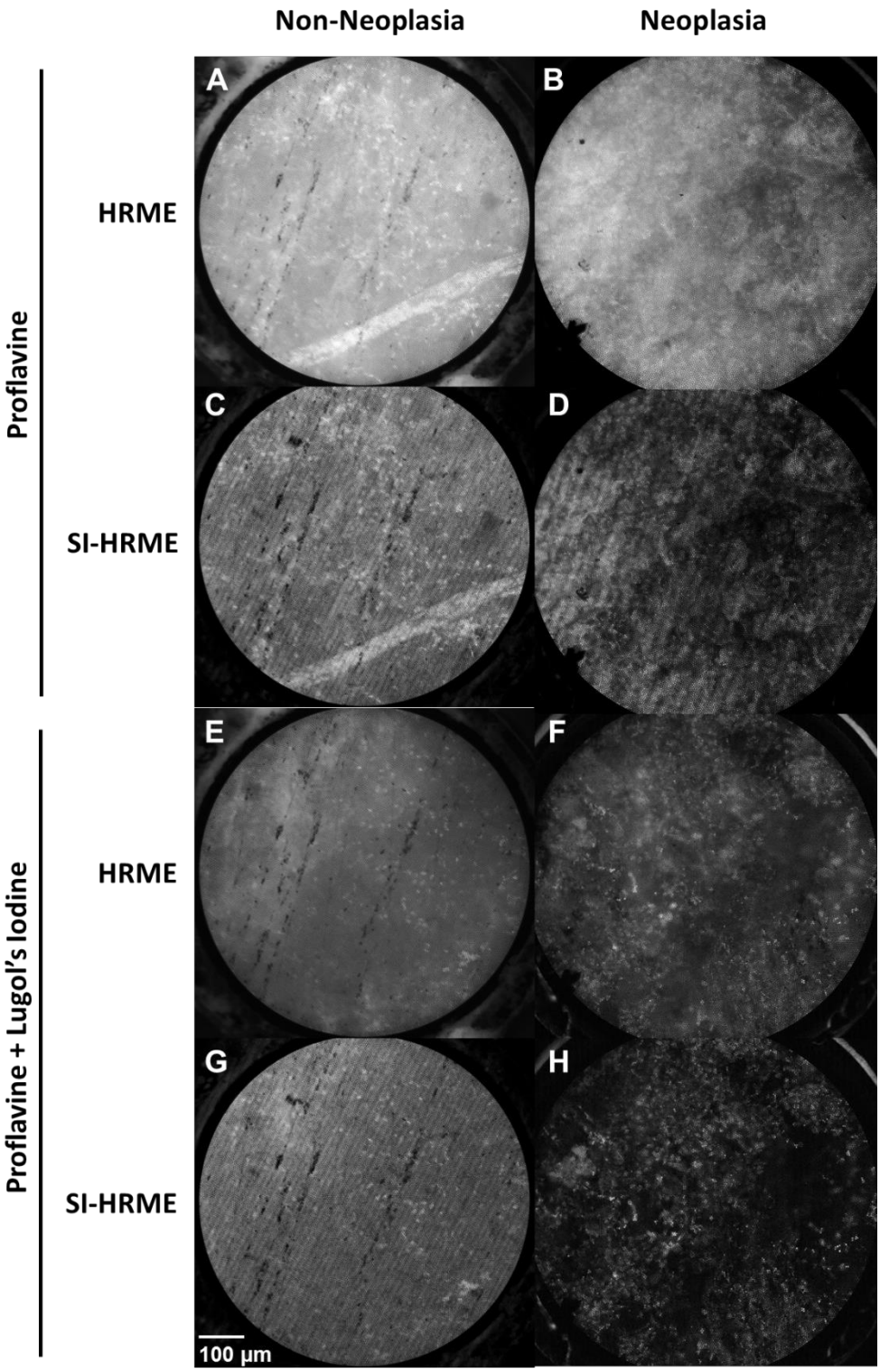

Figure 8-2: Representative HRME and SI-HRME images of a neoplastic site (right) and a non-neoplastic site (left) in human breast tissue specimens stained with Lugol's Iodine. A,B: Breast tissue stained with proflavine and imaged with HRME. C,D: Breast tissue stained with proflavine and imaged with SI-HRME. E,F: Breast tissue stained with Lugol's Iodine and imaged with HRME. G,H: Breast tissue stained with Lugol's Iodine and imaged with SI-HRME. Scale bar is 100 μm for all images.

Figure 8-2 shows representative HRME and SI-HRME images of neoplastic and non-neoplastic sites stained with Lugol's Iodine. The left column of Figure 8-2 shows HRME and SI-HRME images of benign tissue, which is recognizable in both HRME and SI-HRME images based on the presence of sparse nuclei with distribution and size expected in normal breast stroma [15]. The right column of Figure 8-2 shows HRME and SI-HRME images of neoplasia, which is identified based on the presence of large nuclei with crowded and disordered arrangement [15]. Application of Lugol's Iodine reduces background fluorescence in SI-HRME and HRME images.

Figure 8-3 shows contrast measured in confocal images of tissue stained with proflavine and HRME and SI-HRME images of tissue stained with proflavine or Lugol's Iodine and proflavine. Mean contrast is highest in confocal images stained with proflavine. However, mean contrast was not significantly different between confocal and SI-HRME images of tissue stained with proflavine. Incorporating structured illumination significantly increased contrast in HRME images of tissue stained with proflavine ($p < 0.001$). Topical application of Lugol's Iodine significantly increased mean image contrast in HRME images ($p < 0.01$), but not in SI-HRME images. There was no significant difference in contrast between HRME and SI-HRME images of tissue stained with Lugol's Iodine or between SI-HRME images of tissue stained with proflavine or Lugol's Iodine.

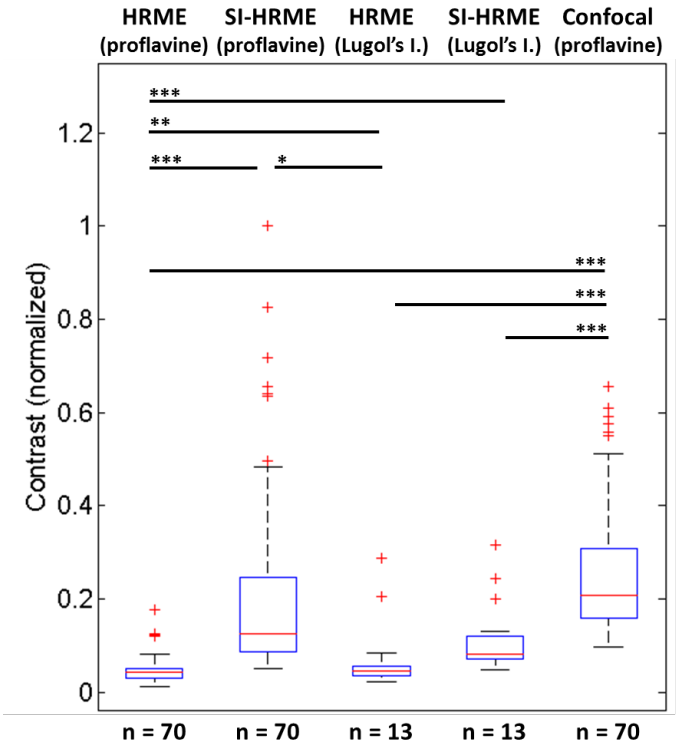

Figure 8-3: Gray level co-occurrence matrix-based contrast measured in confocal, HRME, and SI-HRME images of tissue stained with proflavine or Lugol's Iodine (contrast agent indicated in parentheses). "n" indicates the number of sites represented by each box and whiskers. Statistically significant differences in mean contrast are indicated by asterisks (*); $p < 0.05$ (*), $p < 0.001$ (***).

8.4 Discussion

The objective of this study was to determine if image acquisition with structured illumination and topical application of Lugol's Iodine improve contrast in HRME images of breast tissue. Quantitative evaluation of mean image contrast showed that structured illumination produced images with comparable contrast to confocal images and increased mean contrast in HRME images of tissue stained with proflavine (Figure 8-3). Although visual assessment indicated that Lugol's Iodine application could potentially reduce background fluorescence in HRME and SI-HRME images of neoplasia (Figure 8-2), mean contrast was not significantly

higher in HRME and SI-HRME images of tissue stained with Lugol's Iodine compared to proflavine (Figure 8-3).

There are a few limitations associated with this study. The data were acquired at a single center and visual assessment was performed by one reader. Future studies with multiple readers are needed to verify if neoplasia can be identified in HRME and SI-HRME images of specimens from a larger group of patients.

In conclusion, the findings of this study suggest that structured illumination can be used to increase contrast in HRME images of breast and that SI-HRME could potentially be used to rapidly characterize fresh breast tissue. SI-HRME may have the potential to address the limitations of current techniques for intraoperative tumor margins assessment. However, a future study is needed to evaluate the feasibility of using SI-HRME to identify neoplasia.

9 CHAPTER 9: Conclusion

9.1 Summary and Research Contributions

Breast cancer is the most common form of cancer for women worldwide [6]. Several studies have shown that outcomes are better for women whose disease is detected at an early stage [5, 6, 12]. However, current imaging tools provide limited ability to rapidly diagnose early lesions. There is a crucial need for research to improve rapid lesion diagnosis and assessment of excised tumor margins and sites of surgical resection.

The standard for diagnosis of breast cancer lesions is histologic assessment, which also typically requires immunohistochemistry (IHC) to assess relevant biomarkers. However, both histologic assessment and IHC require extensive preparation and staining and may need to be repeated in cases where lesions are missed due to sampling error [114, 135, 136]. In addition, the standard criteria that are currently used for breast lesion diagnosis are vague and subjective, and there is an unacceptable degree of inter- and intra-observer variability in diagnosis of lesions [81, 83, 86, 221, 222].

Optical imaging has the potential to address the limitations of traditional methods to diagnose breast cancer. Optical imaging systems can provide the ability to image tissue in real time with minimal tissue preparation. Several optical approaches have been used to quickly characterize suspicious breast lesions [90-94, 96, 99, 101, 120, 121, 223, 224]. With the introduction of fiber optic probes, images can be acquired intraoperatively with high spatial resolution to visualize cellular morphology and tumor microenvironment [99-101]. A number of high resolution imaging approaches have been proposed to characterize breast lesions, including optical coherence tomography (OCT), second harmonic generation (SHG) imaging, confocal reflectance and fluorescence microscopy, and high resolution microendoscopy (HRME). The

need for rapid breast lesion diagnosis and tumor margin assessment has motivated investigation of imaging techniques with the potential to inspect tissue in real time, to improve selection of tissue to remove for diagnosis, and to image a greater tissue volume than can be biopsied. There is also a need for quantitative criteria that can be used to objectively evaluate tissue and limit inter- and intra-observer variability in breast lesion diagnosis.

As described in Chapter 3, I performed a study to investigate if confocal fluorescence microscopy, with its proven ability to image intact tissue with diffraction limited spatial resolution [96, 120, 121, 225-227], could yield images with sufficient resolution/quality to enable identification of early neoplasia in the breast. Following topical application of proflavine, a vital fluorescent dye targeting cell nuclei [99, 100, 122], I acquired images of surgically resected breast tissue and core needle biopsy specimens. The images from this study were compiled into a library, which were used to compare the ability of pathologists to visually assess normal, benign, and early neoplastic breast tissue in images acquired using confocal fluorescence microscopy and traditional histopathology. Neoplasia was identified with over 90% sensitivity and specificity in both confocal and histologic images. To further characterize the feasibility of using confocal fluorescence microscopy to evaluate breast tissue, I performed two studies comparing the results of visual assessment of confocal and histologic images. In order to determine if confocal fluorescence microscopy could be used to determine if the biopsy specimens contained adequate tissue for diagnosis and molecular testing, I performed the study described in Chapter 4 to estimate tumor cellularity in grayscale and pseudo-colored confocal images and histologic images of 23 core needle biopsy specimens. The results showed moderate agreement based on a kappa coefficient ($\kappa = 0.477 \pm 0.088$) between assessments of tumor cellularity in histologic and confocal images. As described in Chapter 5, I performed a study to

evaluate agreement between visual assessment of diagnosis and tumor grade in confocal and histologic images of 30 neoplastic breast specimens. Neoplasia was correctly identified in confocal images of 29 of 30 specimens. 24 of 30 specimens were diagnosed as the same type of neoplasia and 21 of 30 specimens were assigned the same grade in confocal and histologic images. The results of these studies demonstrate that images acquired with confocal fluorescence microscopy contain sufficient detail to evaluate neoplastic breast tissue. However, the findings described in Chapter 5 suggest that confocal images are limited in classification of tumor type and grade. This limitation could potentially be addressed by developing fluorescent dyes to identify features that can cause misclassification in confocal images, such as inflammation [228] and necrosis [229].

In order to address the need for quantitative criteria to evaluate breast tissue, I completed two studies to develop and evaluate computerized algorithms for quantitative analysis of breast architecture. I collaborated with researchers at Duke University to develop computerized algorithms to segment and quantitatively evaluate breast cell nuclei and breast ducts. These parameters were used to assemble a decision tree model that classifies images of breast tissue as benign or malignant with an overall accuracy of 90%. To address the second specific aim of this research, I developed a computerized algorithm to segment and measure confocal fluorescence images of adipocytes adjacent to and far from the margins of neoplastic breast lesions and in non-neoplastic tissue, as described in Chapter 7. The results of this study indicate that adipocytes have significantly different phenotypic parameters adjacent to neoplastic lesions versus in non-neoplastic stroma and provide quantitative support for previous studies with similar findings [49, 50, 53, 230]. The findings from the research described in Chapters 6 and 7 indicate that confocal images can be used to rapidly acquire high resolution images of fresh

breast tissue and that quantitative criteria can be used to continue development of objective criteria to evaluate breast neoplasia and the surrounding microenvironment.

The third specific aim of this research was to evaluate a high resolution microendoscope (HRME) system for characterization of breast morphology. Fiber optic tools, including confocal microscopy and HRME, have been developed for high resolution imaging of tissues *in situ* [101, 105, 106, 190]. While HRME offers the advantages of simplicity and low cost, it does not provide sufficient rejection of out-of-focus light to enable successful imaging of breast tissue. As described in Chapter 9, I explored tissue preparation and image acquisition techniques to improve background light rejection, including topical application of Lugol's Iodine [211, 212, 216, 217, 219] and an HRME system with the option to use structured illumination (SI-HRME) [105, 106, 231]. Breast tissue samples were imaged using HRME and SI-HRME and stained with proflavine and Lugol's Iodine. Confocal fluorescence microscopy was used to acquire images of the same specimens to guide image acquisition and as a reference for image contrast. I analyzed images obtained during this study using qualitative criteria of breast architectural features and quantitative metrics of image contrast. The results demonstrated that structured illumination produces images with comparable contrast to confocal images and significantly higher contrast than HRME images acquired with standard illumination. While mean image contrast was elevated in HRME and SI-HRME images of neoplastic tissue compared to non-neoplastic tissue stained with Lugol's Iodine, further study is needed to evaluate the potential of Lugol's Iodine to improve contrast in images of breast tissue.

9.2 Future Research Directions

If the high resolution optical imaging techniques developed and validated with this research prove adequate for evaluation of breast tissue specimens in large, multicenter studies,

these techniques could be useful in a number of clinical scenarios. Initially, high resolution optical imaging could be used to immediately evaluate the adequacy of tissue in core biopsy specimens and then to provide real time diagnostic results. Objective, quantitative criteria for evaluation of breast tissue could potentially be used to assist pathologists in rapid classification of neoplastic and non-neoplastic tissue, including for determining if excised tissue specimens have positive or negative margins. Finally, because images can be obtained in real time without the need for extensive processing, high resolution imaging may be useful to provide histologic diagnosis in low-resource settings where infrastructure for traditional histologic preparation is not available [130].

10 References

1. Dobbs JL, Ding H, Benveniste AP, Kuerer HM, Krishnamurthy S, Yang W, Richards-Kortum R: **Feasibility of confocal fluorescence microscopy for real-time evaluation of neoplasia in fresh human breast tissue**. *Journal of Biomedical Optics* 2013, **18**(10).
2. Dobbs J, Krishnamurthy S, Kyrish M, Benveniste AP, Yang W, Richards-Kortum R: **Confocal fluorescence microscopy for rapid evaluation of invasive tumor cellularity of inflammatory breast carcinoma core needle biopsies**. *Breast Cancer Res Treat* 2014.
3. Dobbs JL, Mueller JL, Krishnamurthy S, Shin D, Kuerer H, Yang W, Ramanujam N, Richards-Kortum R: **Micro-anatomical quantitative optical imaging: toward automated assessment of breast tissues**. *Breast Cancer Res* 2015, **17**:105.
4. Siegel R, Naishadham D, Jemal A: **Cancer Statistics, 2012**. *Ca-a Cancer Journal for Clinicians* 2012, **62**(1):10-29.
5. DeSantis C, Siegel R, Bandi P, Jemal A: **Breast cancer statistics, 2011**. *Ca-a Cancer Journal for Clinicians* 2011, **61**(6):409-418.
6. Jemal A, Bray F, Center MM, Ferlay J, Ward E, Forman D: **Global Cancer Statistics**. *Ca-a Cancer Journal for Clinicians* 2011, **61**(2):69-90.
7. Gethins M: **Breast cancer in men**. *J Natl Cancer Inst* 2012, **104**(6):436-438.
8. McTiernan A: **Behavioral risk factors in breast cancer: Can risk be modified?** *Oncologist* 2003, **8**(4):326-334.
9. Danaei G, Vander Hoorn S, Lopez AD, Murray CJL, Ezzati M, Comparative Risk Assessment C: **Causes of cancer in the world: comparative risk assessment of nine behavioural and environmental risk factors**. *Lancet* 2005, **366**(9499):1784-1793.
10. **NCCN Clinical Practive Guidelines in Oncology (NCCN Guidelines)$^{(R)}$ - Breast Cancer**. In. Edited by Network NCC, Version 2.2012 edn; 2012.
11. Guthrie EW: **The Breast Cancer Pathology Report: What Pharmacists Need to Know**. *US Pharmacist* 2009, **34**(5 (Oncology supplement)):6-12.
12. Siegel RL, Miller KD, Jemal A: **Cancer statistics, 2015**. *CA Cancer J Clin* 2015, **65**(1):5-29.
13. Howlader N, Noone A, Krapcho M, Neyman N, Aminou R, Altekreuse S, Kosary C, Ruhl J, Tatalovich Z, Cho H *et al*: **SEER Cancer Statistics Review, 1975-2009 (Vintage 2009 Populations)**. In. Bethesda, MD, USA: National Cancer Institute; 2011.
14. LH B, MM B, P C, M D, JE D: **Gray's Anatomy**, 38 edn. New York, USA: Churchill Livingstone; 1995.
15. Rosen PP: **Rosen's Breast Pathology**, 3 edn: Lippincott Williams & Wilkins; 2008.
16. Ramsay DT, Kent JC, Hartmann RA, Hartmann PE: **Anatomy of the lactating human breast redefined with ultrasound imaging.** *J Anat* 2005, **206**(6):525-534.
17. Going JJ, Moffat DF: **Escaping from Flatland: clinical and biological aspects of human mammary duct anatomy in three dimensions.** *J Pathol* 2004, **203**(1):538-544.
18. Love SM, Barsky SH: **Anatomy of the nipple and breast ducts revisited.** *Cancer* 2004, **101**(9):1947-1957.
19. Hindle W: **Breast Care**. New York, USA: Springer-Verlag; 1999.
20. Tobon H, Salazar H: **Ultrastructure of the human mammary gland. II. Postpartum lactogenesis.** *J Clin Endocrinol Metab* 1975, **40**(5):834-844.
21. Jamal N, Ng KH, McLean D, Looi LM, Moosa F: **Mammographic breast glandularity in Malaysian women: data derived from radiography.** *AJR Am J Roentgenol* 2004, **182**(3):713-717.

22. Allred DC, Wu Y, Mao S, Nagtegaal ID, Lee S, Perou CM, Mohsin SK, O'Connell P, Tsimelzon A, Medina D: **Ductal carcinoma in situ and the emergence of diversity during breast cancer evolution.** *Clin Cancer Res* 2008, **14**(2):370-378.
23. Wellings SR, Jensen HM: **On the origin and progression of ductal carcinoma in the human breast.** *J Natl Cancer Inst* 1973, **50**(5):1111-1118.
24. Holland JF, Frei III E, Hong WK, Bast Jr. RC, Hait WN, Kufe DW, Pollock RE, Weichselbaum RR: **Holland-Frei Cancer Medicine**, 8 edn. Shelton, CT, USA: People's Medical Publishing House - USA; 2009.
25. Wellings SR, Jensen HM, Marcum RG: **An atlas of subgross pathology of the human breast with special reference to possible precancerous lesions**. *J Natl Cancer Inst* 1975, **55**(2):231-273.
26. Rosen PP: **Frozen section diagnosis of breast lesions. Recent experience with 556 consecutive biopsies**. *Ann Surg* 1978, **187**(1):17-19.
27. Skinner KA, Silverstein MJ: **The management of ductal carcinoma in situ of the breast**. *Endocr Relat Cancer* 2001, **8**(1):33-45.
28. Omer ZB, Hwang ES, Esserman LJ, Howe R, Ozanne EM: **Impact of ductal carcinoma in situ terminology on patient treatment preferences**. *JAMA Intern Med* 2013, **173**(19):1830-1831.
29. Punglia RS, Schnitt SJ, Weeks JC: **Treatment of ductal carcinoma in situ after excision: would a prophylactic paradigm be more appropriate?** *J Natl Cancer Inst* 2013, **105**(20):1527-1533.
30. Narod SA, Iqbal J, Giannakeas V, Sopik V, Sun P: **Breast Cancer Mortality After a Diagnosis of Ductal Carcinoma In Situ**. *JAMA Oncol* 2015, **1**(7):888-896.
31. Rosen PP: **The pathological classification of human mammary carcinoma: past, present and future**. *Ann Clin Lab Sci* 1979, **9**(2):144-156.
32. Newman W: **Lobular carcinoma of the female breast. Report of 73 cases**. *Ann Surg* 1966, **164**(2):305-314.
33. Dixon JM, Anderson TJ, Page DL, Lee D, Duffy SW: **Infiltrating lobular carcinoma of the breast**. *Histopathology* 1982, **6**(2):149-161.
34. Martinez V, Azzopardi JG: **Invasive lobular carcinoma of the breast: incidence and variants**. *Histopathology* 1979, **3**(6):467-488.
35. Tulinius H, Bjarnason O, Sigvaldason H, Bjarnadottir G, Olafsdottir G: **Tumours in Iceland. 10. Malignant tumours of the female breast. A histological classification, laterality, survival and epidemiological considerations**. *APMIS* 1988, **96**(3):229-238.
36. Maier WP, Rosemond GP, Goldman LI, Kaplan GF, Tyson RR: **A ten year study of medullary carcinoma of the breast**. *Surg Gynecol Obstet* 1977, **144**(5):695-698.
37. Bloom HJ, Richardson WW, Field JR: **Host resistance and survival in carcinoma of breast: a study of 104 cases of medullary carcinoma in a series of 1,411 cases of breast cancer followed for 20 years**. *Br Med J* 1970, **3**(5716):181-188.
38. Rasmussen BB, Rose C, Christensen IB: **Prognostic factors in primary mucinous breast carcinoma**. *Am J Clin Pathol* 1987, **87**(2):155-160.
39. Avisar E, Khan MA, Axelrod D, Oza K: **Pure mucinous carcinoma of the breast: a clinicopathologic correlation study**. *Ann Surg Oncol* 1998, **5**(5):447-451.
40. Wingo PA, Jamison PM, Young JL, Gargiullo P: **Population-based statistics for women diagnosed with inflammatory breast cancer (United States)**. *Cancer Causes Control* 2004, **15**(3):321-328.
41. Anderson WF, Chu KC, Chang S: **Inflammatory breast carcinoma and noninflammatory locally advanced breast carcinoma: distinct clinicopathologic entities?** *J Clin Oncol* 2003, **21**(12):2254-2259.
42. Tlsty TD, Hein PW: **Know thy neighbor: stromal cells can contribute oncogenic signals**. *Curr Opin Genet Dev* 2001, **11**(1):54-59.

43. Jodele S, Blavier L, Yoon JM, DeClerck YA: **Modifying the soil to affect the seed: role of stromal-derived matrix metalloproteinases in cancer progression**. *Cancer Metastasis Rev* 2006, **25**(1):35-43.
44. Wiseman BS, Werb Z: **Stromal effects on mammary gland development and breast cancer**. *Science* 2002, **296**(5570):1046-1049.
45. Conklin MW, Keely PJ: **Why the stroma matters in breast cancer: Insights into breast cancer patient outcomes through the examination of stromal biomarkers**. *Cell Adh Migr* 2012, **6**(3):249-260.
46. Conklin MW, Eickhoff JC, Riching KM, Pehlke CA, Eliceiri KW, Provenzano PP, Friedl A, Keely PJ: **Aligned Collagen Is a Prognostic Signature for Survival in Human Breast Carcinoma**. *American Journal of Pathology* 2011, **178**(3):1221-1232.
47. Provenzano PP, Inman DR, Eliceiri KW, Knittel JG, Yan L, Rueden CT, White JG, Keely PJ: **Collagen density promotes mammary tumor initiation and progression**. *Bmc Medicine* 2008, **6**.
48. Provenzano PP, Eliceiri KW, Campbell JM, Inman DR, White JG, Keely PJ: **Collagen reorganization at the tumor-stromal interface facilitates local invasion**. *Bmc Medicine* 2006, **4**.
49. Tan J, Buache E, Chenard M-P, Dali-Youcef N, Rio M-C: **Adipocyte is a non-trivial, dynamic partner of breast cancer cells**. *International Journal of Developmental Biology* 2011, **55**(7-9):851-859.
50. Dirat B, Bochet L, Dabek M, Daviaud D, Dauvillier S, Majed B, Wang YY, Meulle A, Salles B, Le Gonidec S *et al*: **Cancer-Associated Adipocytes Exhibit an Activated Phenotype and Contribute to Breast Cancer Invasion**. *Cancer Research* 2011, **71**(7).
51. Rio M-C: **The Role of Cancer-Associated Adipocytes (CAA) in the Dynamic Interaction Between the Tumor and the Host**. In: *Tumor-Associated Fibroblasts and their Matrix.* edn. Edited by Mueller MM, Fusening NE. Dordrecht, NetherlandsHeidelberg, GermanyLondon, EnglandNew York, USA: Springer; 2011.
52. Li T, Sun LM, Miller N, Nicklee T, Woo J, Hulse-Smith L, Tsao MS, Khokha R, Martin L, Boyd N: **The association of measured breast tissue characteristics with mammographic density and other risk factors for breast cancer**. *Cancer Epidemiology Biomarkers & Prevention* 2005, **14**(2).
53. Rio M-C: **The role of Cancer-Associated Adipocytes (CAA) in the dynamic interaction between the tumor and the host**. *The Tumor Microenvironment* 2011, **4**(2):111-123.
54. Smith RA, Saslow D, Sawyer KA, Burke W, Costanza ME, Evans WP, Foster RS, Hendrick E, Eyre HJ, Sener S: **American cancer society guidelines for breast cancer screening: Update 2003**. *Ca-a Cancer Journal for Clinicians* 2003, **53**(3):141-169.
55. Barton MB, Harris R, Fletcher SW: **The rational clinical examination. Does this patient have breast cancer? The screening clinical breast examination: should it be done? How?** *JAMA* 1999, **282**(13):1270-1280.
56. Saslow D, Hannan J, Osuch J, Alciati MH, Baines C, Barton M, Bobo JK, Coleman C, Dolan M, Gaumer G *et al*: **Clinical breast examination: practical recommendations for optimizing performance and reporting**. *CA Cancer J Clin* 2004, **54**(6):327-344.
57. Bobo JK, Lee NC, Thames SF: **Findings from 752,081 clinical breast examinations reported to a national screening program from 1995 through 1998**. *J Natl Cancer Inst* 2000, **92**(12):971-976.
58. McDonald S, Saslow D, Alciati MH: **Performance and reporting of clinical breast examination: a review of the literature**. *CA Cancer J Clin* 2004, **54**(6):345-361.
59. Bathla L, Harris A, Davey M, Sharma P, Silva E: **High resolution intra-operative two-dimensional specimen mammography and its impact on second operation for re-excision of positive margins at final pathology after breast conservation surgery**. *American Journal of Surgery* 2011, **202**(4):387-394.

60. Bancej C, Decker K, Chiarelli A, Harrison M, Turner D, Brisson J: **Contribution of clinical breast examination to mammography screening in the early detection of breast cancer**. *J Med Screen* 2003, **10**(1):16-21.
61. Berg WA, Gutierrez L, NessAiver MS, Carter WB, Bhargavan M, Lewis RS, Ioffe OB: **Diagnostic accuracy of mammography, clinical examination, US, and MR imaging in preoperative assessment of breast cancer**. *Radiology* 2004, **233**(3):830-849.
62. Kolb TM, Lichy J, Newhouse JH: **Comparison of the performance of screening mammography, physical examination, and breast US and evaluation of factors that influence them: an analysis of 27,825 patient evaluations**. *Radiology* 2002, **225**(1):165-175.
63. Ascunce EN, Moreno-Iribas C, Urtiaga AB, Ardanaz E, Sanz ME, Castilla J, Egues N: **Changes in breast cancer mortality in Navarre (Spain) after introduction of a screening programme**. *Journal of Medical Screening* 2007, **14**(1):14-20.
64. Berry DA, Cronin KA, Plevritis SK, Fryback DG, Clarke L, Zelen M, Mandelblatt JS, Yakovlev AY, Habbema JDF, Feuer EJ *et al*: **Effect of screening and adjuvant therapy on mortality from breast cancer**. *New England Journal of Medicine* 2005, **353**(17):1784-1792.
65. Gabe R, Duffy SW: **Evaluation of service screening mammography in practice: the impact on breast cancer mortality**. *Annals of oncology : official journal of the European Society for Medical Oncology / ESMO* 2005, **16 Suppl 2**:ii153-162.
66. Radiology ACo: **American College of Radiology (ACR) reporting system, in Breast Imaging Reporting and Data System**. In., 2 edn. Reston, VA; 1993: 15-18.
67. Burhenne HJ, Burhenne LW, Goldberg F, Hislop TG, Worth AJ, Rebbeck PM, Kan L: **Interval breast cancers in the Screening Mammography Program of British Columbia: analysis and classification**. *AJR Am J Roentgenol* 1994, **162**(5):1067-1071; discussion 1072-1065.
68. Houssami N, Irwig L, Simpson JM, McKessar M, Blome S, Noakes J: **Sydney Breast Imaging Accuracy Study: Comparative sensitivity and specificity of mammography and sonography in young women with symptoms**. *AJR Am J Roentgenol* 2003, **180**(4):935-940.
69. Kerlikowske K, Grady D, Barclay J, Sickles EA, Ernster V: **Effect of age, breast density, and family history on the sensitivity of first screening mammography**. *JAMA* 1996, **276**(1):33-38.
70. Kuhl CK, Schrading S, Leutner CC, Morakkabati-Spitz N, Wardelmann E, Fimmers R, Kuhn W, Schild HH: **Mammography, breast ultrasound, and magnetic resonance imaging for surveillance of women at high familial risk for breast cancer**. *J Clin Oncol* 2005, **23**(33):8469-8476.
71. Saarenmaa I, Salminen T, Geiger U, Heikkinen P, Hyvärinen S, Isola J, Kataja V, Kokko ML, Kokko R, Kumpulainen E *et al*: **The effect of age and density of the breast on the sensitivity of breast cancer diagnostic by mammography and ultasonography**. *Breast Cancer Res Treat* 2001, **67**(2):117-123.
72. Pijpe A, Andrieu N, Easton DF, Kesminiene A, Cardis E, Noguès C, Gauthier-Villars M, Lasset C, Fricker JP, Peock S *et al*: **Exposure to diagnostic radiation and risk of breast cancer among carriers of BRCA1/2 mutations: retrospective cohort study (GENE-RAD-RISK)**. *BMJ* 2012, **345**:e5660.
73. Stavros AT, Thickman D, Rapp CL, Dennis MA, Parker SH, Sisney GA: **Solid breast nodules: use of sonography to distinguish between benign and malignant lesions**. *Radiology* 1995, **196**(1):123-134.
74. Kuhl CK, Mielcareck P, Klaschik S, Leutner C, Wardelmann E, Gieseke J, Schild HH: **Dynamic breast MR imaging: are signal intensity time course data useful for differential diagnosis of enhancing lesions?** *Radiology* 1999, **211**(1):101-110.
75. Kriege M, Brekelmans CT, Boetes C, Besnard PE, Zonderland HM, Obdeijn IM, Manoliu RA, Kok T, Peterse H, Tilanus-Linthorst MM *et al*: **Efficacy of MRI and mammography for breast-cancer**

screening in women with a familial or genetic predisposition. *N Engl J Med* 2004, **351**(5):427-437.

76. Moore SG, Shenoy PJ, Fanucchi L, Tumeh JW, Flowers CR: **Cost-effectiveness of MRI compared to mammography for breast cancer screening in a high risk population**. *BMC Health Serv Res* 2009, **9**:9.
77. Allred DC, Harvey JM, Berardo M, Clark GM: **Prognostic and predictive factors in breast cancer by immunohistochemical analysis**. *Mod Pathol* 1998, **11**(2):155-168.
78. Bloom HJG, Richardson WW: **HISTOLOGICAL GRADING AND PROGNOSIS IN BREAST CANCER - A STUDY OF 1409 CASES OF WHICH 359 HAVE BEEN FOLLOWED FOR 15 YEARS**. *British Journal of Cancer* 1957, **11**(3):359-&.
79. Silverberg SG: **Atlas of Breast Pathology**. Philadelphia, Pennsylvania, USA: W.B. Saunders Company; 2002.
80. Elston CW, Ellis IO: **Pathological prognostic factors in breast cancer. I. The value of histological grade in breast cancer: experience from a large study with long-term follow-up**. *Histopathology* 1991, **19**(5):403-410.
81. Schnitt SJ, Connolly JL, Tavassoli FA, Fechner RE, Kempson RL, Gelman R, Page DL: **Interobserver reproducibility in the diagnosis of ductal proliferative breast lesions using standardized criteria**. *Am J Surg Pathol* 1992, **16**(12):1133-1143.
82. Delides GS, Garas G, Georgouli G, Jiortziotis D, Lecca J, Liva T, Elemenoglou J: **INTRALABORATORY VARIATIONS IN THE GRADING OF BREAST-CARCINOMA**. *Archives of Pathology & Laboratory Medicine* 1982, **106**(3):126-128.
83. Rosai J: **Borderline epithelial lesions of the breast**. *Am J Surg Pathol* 1991, **15**(3):209-221.
84. Theissig F, Kunze KD, Haroske G, Meyer W: **HISTOLOGICAL GRADING OF BREAST-CANCER - INTEROBSERVER, REPRODUCIBILITY AND PROGNOSTIC-SIGNIFICANCE**. *Pathology Research and Practice* 1990, **186**(6):732-736.
85. Meyer JS, Alvarez C, Milikowski C, Olson N, Russo I, Russo J, Glass A, Zehnbauer BA, Lister K, Parwaresch R *et al*: **Breast carcinoma malignancy grading by Bloom-Richardson system vs proliferation index: reproducibility of grade and advantages of proliferation index**. *Modern Pathology* 2005, **18**(8):1067-1078.
86. Frierson HF, Wolber RA, Berean KW, Franquemont DW, Gaffey MJ, Boyd JC, Wilbur DC: **INTEROBSERVER REPRODUCIBILITY OF THE NOTTINGHAM MODIFICATION OF THE BLOOM AND RICHARDSON HISTOLOGIC GRADING SCHEME FOR INFILTRATING DUCTAL CARCINOMA**. *American Journal of Clinical Pathology* 1995, **103**(2):195-198.
87. Stenkvist B, Westmannaeser S, Vegelius J, Holmquist J, Nordin B, Bengtsson E, Eriksson O: **ANALYSIS OF REPRODUCIBILITY OF SUBJECTIVE GRADING SYSTEMS FOR BREAST-CARCINOMA**. *Journal of Clinical Pathology* 1979, **32**(10):979-985.
88. Bouma B: **Handbook of optical coherence tomography**. New York, USA: Marcel Dekker, Inc.; 2002.
89. Sampson DD, Hillman TR: **Optical coherence tomography**. *Lasers and Current Optical Techniques in Biology* 2004, **4**.
90. McLaughlin RA, Scolaro L, Robbins P, Hamza S, Saunders C, Sampson DD: **Imaging of Human Lymph Nodes Using Optical Coherence Tomography: Potential for Staging Cancer**. *Cancer Research* 2010, **70**(7):2579-2584.
91. Nguyen FT, Zysk AM, Chaney EJ, Kotynek JG, Oliphant UJ, Bellafiore FJ, Rowland KM, Johnson PA, Boppart SA: **Intraoperative Evaluation of Breast Tumor Margins with Optical Coherence Tomography**. *Cancer Research* 2009, **69**(22):8790-8796.

92. Jain M, Shukla N, Manzoor M, Nadolny S, Mukherjee S: **Modified full-field optical coherence tomography: A novel tool for rapid histology of tissues**. *Journal of pathology informatics* 2011, **2**:28.
93. Nguyen FT, Zysk AM, Chaney EJ, Adie SG, Kotynek JG, Oliphant UJ, Bellafiore FJ, Rowland KM, Johnson PA, Boppart SA: **Optical Coherence Tomography The Intraoperative Assessment of Lymph Nodes in Breast Cancer**. *IEEE Engineering in Medicine and Biology Magazine* 2010, **29**(2):63-70.
94. Zysk AM, Chen K, Gabrielson E, Tafra L, May Gonzalez EA, Canner JK, Schneider EB, Cittadine AJ, Scott Carney P, Boppart SA *et al*: **Intraoperative Assessment of Final Margins with a Handheld Optical Imaging Probe During Breast-Conserving Surgery May Reduce the Reoperation Rate: Results of a Multicenter Study**. *Ann Surg Oncol* 2015, **22**(10):3356-3362.
95. Webb RH: **Confocal Optical Microscopy**. *Reports on Progress in Physics* 1996, **59**(3):427-471.
96. Tilli MT, Cabrera MC, Parrish AR, Torre KM, Sidawy MK, Gallagher AL, Makariou E, Polin SA, Liu MC, Furth PA: **Real-time imaging and characterization of human breast tissue by reflectance confocal microscopy**. *Journal of biomedical optics* 2007, **12**(5):051901.
97. Li Y, Gonzalez S, Terwey TH, Wolchok J, Aranda I, Toledo-Crow R, Halpern AC: **Dual mode reflectance and fluorescence confocal laser scanning microscopy for in vivo imaging melanoma progression in murine skin**. *J Invest Dermatol* 2005, **125**(4):798-804.
98. Gareau DS, Jeon H, Nehal KS, Rajadhyaksha M: **Rapid screening of cancer margins in tissue with multimodal confocal microscopy**. *J Surg Res* 2012.
99. Rosbach KJ, Shin D, Muldoon TJ, Quraishi MA, Middleton LP, Hunt KK, Meric-Bernstam F, Yu TK, Richards-Kortum RR, Yang W: **High-resolution fiber optic microscopy with fluorescent contrast enhancement for the identification of axillary lymph node metastases in breast cancer: a pilot study**. *Biomed Opt Express* 2010, **1**(3):911-922.
100. Muldoon TJ, Anandasabapathy S, Maru D, Richards-Kortum R: **High-resolution imaging in Barrett's esophagus: a novel, low-cost endoscopic microscope**. *Gastrointestinal Endoscopy* 2008, **68**(4):737-744.
101. Muldoon TJ, Pierce MC, Nida DL, Williams MD, Gillenwater A, Richards-Kortum R: **Subcellular-resolution molecular imaging within living tissue by fiber microendoscopy**. *Opt Express* 2007, **15**(25):16413-16423.
102. Rosbach KJ, Shin D, Muldoon TJ, Quraishi MA, Middleton LP, Hunt KK, Meric-Bernstam F, Yu TK, Richards-Kortum RR, Yang W: **High-resolution fiber optic microscopy with fluorescent contrast enhancement for the identification of axillary lymph node metastases in breast cancer: a pilot study**. *Biomedical Optics Express* 2010, **1**(3):911-922.
103. Neil MA, Juskaitis R, Wilson T: **Method of obtaining optical sectioning by using structured light in a conventional microscope**. *Opt Lett* 1997, **22**(24):1905-1907.
104. Chasles F, Dubertret B, Boccara AC: **Optimization and characterization of a structured illumination microscope**. *Opt Express* 2007, **15**(24):16130-16140.
105. Bozinovic N, Ventalon C, Ford T, Mertz J: **Fluorescence endomicroscopy with structured illumination**. *Opt Express* 2008, **16**(11):8016-8025.
106. Mertz J: **Optical sectioning microscopy with planar or structured illumination**. *Nature Methods* 2011, **8**(10):811-819.
107. Rahman M, Abd-El-Barr M, Mack V, Tkaczyk T, Sokolov K, Richards-Kortum R, Descour M: **Optical imaging of cervical pre-cancers with structured illumination: an integrated approach**. *Gynecol Oncol* 2005, **99**(3 Suppl 1):S112-115.
108. Keahey PA, Tkaczyk TS, Schmeler KM, Richards-Kortum RR: **Optimizing modulation frequency for structured illumination in a fiber-optic microendoscope to image nuclear morphometry in columnar epithelium**. *Biomed Opt Express* 2015, **6**(3):870-880.

109. Jain S, Wang X, Chang CC, Ibarra-Drendall C, Wang H, Zhang Q, Brady SW, Li P, Zhao H, Dobbs J *et al*: **Src Inhibition Blocks c-Myc Translation and Glucose Metabolism to Prevent the Development of Breast Cancer**. *Cancer Res* 2015.
110. Feuer EJ, Wun LM, Boring CC, Flanders WD, Timmel MJ, Tong T: **The lifetime risk of developing breast cancer**. *Journal of the National Cancer Institute* 1993, **85**(11):892-897.
111. Jemal A: **Cancer Statistics, 2010**. *CA-A Cancer Journal for Clinicians* 2011, **61**(2):277-300.
112. Winther C, Graem N: **Accuracy of frozen section diagnosis: a retrospective analysis of 4785 cases**. *APMIS* 2011, **119**(4-5):259-262.
113. Bauermeister DE: **The role and limitations of frozen section and needle aspiration biopsy in breast cancer diagnosis**. *Cancer* 1980, **46**(4 Suppl):947-949.
114. Cheng L, Al-Kaisi NK, Liu AY, Gordon NH: **The results of intraoperative consultations in 181 ductal carcinomas in situ of the breast**. *Cancer* 1997, **80**(1):75-79.
115. Connolly JL, Fechner RE, Page DL, Silverberg SG: **Immediate Management of Mammographically Detected Breast Lesions**. *American Journal of Surgical Pathology* 1993, **17**(8):850-851.
116. J S: **Quality assurance guidelines for pathology in mammography screening.** . In: *European guidelines for quality assurance in mammography screening* edn. Edited by NM DWCaP. Luxembourg: Office for Official Publications of the European Communities; 1996.
117. Zafrani B, Contesso G, Eusebi V, Holland R, Millis RR, Peterse JL: **Guidelines for the Pathological Management of Mammographically Detected Breast Lesions**. *Breast* 1995, **4**(1):52-56.
118. Scheiden R, Sand J, Tanous AM, Knolle U, Capesius C, Wagnon MC, Faverly D: **Accuracy of frozen section diagnoses of breast lesions after introduction of a national programme in mammographic screening**. *Histopathology* 2001, **39**(1):74-84.
119. Campo-Ruiz V, Ochoa ER, Lauwers GY, Gonzalez S: **Evaluation of hepatic histology by near-infrared confocal microscopy: A pilot study**. *Human Pathology* 2002, **33**(10):975-982.
120. Parrish A, Halama E, Tilli MT, Freedman M, Furth PA: **Reflectance confocal microscopy for characterization of mammary ductal structures and development of neoplasia in genetically engineered mouse models of breast cancer**. *Journal of Biomedical Optics* 2005, **10**(5).
121. Schiffhauer LM, Boger JN, Bonfiglio TA, Zavislan JM, Zuley M, Fox CA: **Confocal Microscopy of Unfixed Breast Needle Core Biopsies: A Comparison to Fixed and Stained Sections**. *BMC Cancer* 2009, **9**.
122. Pierce MC, Javier DJ, Richards-Kortum R: **Optical contrast agents and imaging systems for detection and diagnosis of cancer**. *International Journal of Cancer* 2008, **123**(9):1979-1990.
123. Yamauchi H, Woodward WA, Valero V, Alvarez RH, Lucci A, Buchholz TA, Iwamoto T, Krishnamurthy S, Yang W, Reuben JM *et al*: **Inflammatory breast cancer: what we know and what we need to learn**. *Oncologist* 2012, **17**(7):891-899.
124. van de Ven AL, Adler-Storthz K, Richards-Kortum R: **Delivery of optical contrast agents using Triton-X100, part 2: enhanced mucosal permeation for the detection of cancer biomarkers**. *Journal of Biomedical Optics* 2009, **14**(2).
125. Fleiss JL, Levin B, Paik MC: **The Measurement of Interrater Agreement**. In: *Statistical Methods for Rates and Proportions.* 3 edn. Hoboken, NJ, USA: John Wiley & Sons, Inc.; 2003.
126. Landis JR, Koch GG: **The measurement of observer agreement for categorical data**. *Biometrics* 1977, **33**(1):159-174.
127. Sim J, Wright CC: **The kappa statistic in reliability studies: use, interpretation, and sample size requirements**. *Phys Ther* 2005, **85**(3):257-268.
128. Viera AJ, Garrett JM: **Understanding interobserver agreement: the kappa statistic**. *Fam Med* 2005, **37**(5):360-363.

129. D'Halluin F, Tas P, Rouquette S, Bendavid C, Foucher F, Meshba H, Blanchot J, Coué O, Levêque J: **Intra-operative touch preparation cytology following lumpectomy for breast cancer: a series of 400 procedures.** *Breast* 2009, **18**(4):248-253.
130. Adeyi OA: **Pathology Services in Developing Countries-The West African Experience**. *Archives of Pathology & Laboratory Medicine* 2011, **135**(2):183-186.
131. Hance KW, Anderson WF, Devesa SS, Young HA, Levine PH: **Trends in inflammatory breast carcinoma incidence and survival: the surveillance, epidemiology, and end results program at the National Cancer Institute**. *Journal of the National Cancer Institute* 2005, **97**(13):966-975.
132. Anderson WF, Chu KC, Chang S: **Inflammatory breast carcinoma and noninflammatory locally advanced breast carcinoma: distinct clinicopathologic entities?** *Journal of Clinical Oncology* 2003, **21**(12):2254-2259.
133. Kumar N, Sayed S, Moloo Z, Wasike R: **Fine-Needle Aspiration in Suspected Inflammatory Breast Cancer: Case Series with Emphasis on Approach to Specimen Adequacy**. *Acta Cytologica* 2011, **55**(3):239-244.
134. Iwase T, Takahashi K, Gomi N, Horii R, Akiyama F: **Present state of and problems with core needle biopsy for non-palpable breast lesions**. *Breast cancer (Tokyo, Japan)* 2006, **13**(1):32-37.
135. Shah VI, Raju U, Chitale D, Deshpande V, Gregory N, Strand V: **False-negative core needle biopsies of the breast - An analysis of clinical, radiologic, and pathologic findings in 27 consecutive cases of missed breast cancer**. *Cancer* 2003, **97**(8):1824-1831.
136. Dillon MF, Hill ADK, Quinn CM, O'Doherty A, McDermott EW, O'Higgins N: **The accuracy of ultrasound, stereotactic, and clinical core biopsies in the diagnosis of breast cancer, with an analysis of false-negative cases**. *Annals of Surgery* 2005, **242**(5):701-707.
137. Abeytunge S, Li Y, Larson B, Peterson G, Seltzer E, Toledo-Crow R, Rajadhyaksha M: **Confocal microscopy with strip mosaicing for rapid imaging over large areas of excised tissue**. *Journal of Biomedical Optics* 2013, **18**(6).
138. Muldoon TJ, Pierce MC, Nida DL, Williams MD, Gillenwater A, Richards-Kortum R: **Subcellular-resolution molecular imaging within living tissue by fiber microendoscopy**. *Optics Express* 2007, **15**(25):16413-16423.
139. Gareau DS: **Feasibility of digitally stained multimodal confocal mosaics to simulate histopathology**. *Journal of Biomedical Optics* 2009, **14**(3).
140. Rajan R, Poniecka A, Smith TL, Yang Y, Frye D, Pusztai L, Fiterman DJ, Gal-Gombos E, Whitman G, Rouzier R *et al*: **Change in tumor cellularity of breast carcinoma after neoadjuvant chemotherapy as a variable in the pathologic assessment of response**. *Cancer* 2004, **100**(7):1365-1373.
141. Viera AJ, Garrett JM: **Understanding interobserver agreement: the kappa statistic**. *Family Medicine* 2005, **37**(5):360-363.
142. Perrot N, Jalaguier-Coudray A, Frey I, Thomassin-Naggara I, Chopier J: **US-guided core needle biopsy: False-negatives. How to reduce them?** *European Journal of Radiology* 2013, **82**(3):424-426.
143. Youk JH, Kim E-K, Kim MJ, Kwak JY, Son EJ: **Analysis of false-negative results after US-guided 14-gauge core needle breast biopsy**. *European Radiology* 2010, **20**(4):782-789.
144. Garg S, Mohan H, Bal A, Attri AK, Kochhar S: **A comparative analysis of core needle biopsy and fine-needle aspiration cytology in the evaluation of palpable mammographically suspicious breast detected lesions**. *Diagnostic Cytopathology* 2007, **35**(11):681-689.
145. Collins LC, Connolly JL, Page DL, Goulart RA, Pisano ED, Fajardo LL, Berg WA, Caudry DJ, McNeil BJ, Schnitt SJ: **Diagnostic agreement in the evaluation of image-guided breast core needle biopsies - Results from a randomized clinical**. *American Journal of Surgical Pathology* 2004, **28**(1):126-131.

146. Peter D, Gruenhagen J, Wenke R, Schaefer FKW, Schreer I: **False-negative results after stereotactically guided vacuum biopsy**. *European Radiology* 2008, **18**(1):177-182.
147. Bini J, Spain J, Nehal K, Hazelwood V, DiMarzio C, Rajadhyaksha M: **Confocal mosaicing microscopy of human skin ex vivo: spectral analysis for digital staining to simulate histology-like appearance**. *Journal of Biomedical Optics* 2011, **16**(7).
148. Mohammadi A, Rosa M, Masood S: **The Use of Fine-Needle Aspiration Biopsy Samples for the Assessment of Basal Phenotype in Triple Negative Breast Cancer Patients: A Correlative Study**. *Diagnostic Cytopathology* 2011, **39**(1):1-7.
149. Ibrahim AEK, Bateman AC, Theaker JM, Low JL, Addis B, Tidbury P, Rubin C, Briley M, Royle GT: **The role and histological classification of needle core biopsy in comparison with fine needle aspiration cytology in the preoperative assessment of impalpable breast lesions**. *Journal of Clinical Pathology* 2001, **54**(2):121-125.
150. Kass R, Henry-Tillman RS, Nurko J, Korourian S, Mancino AT, Colvert M, Johnson A, Lane S, Layeeque R, Brown H *et al*: **Touch preparation of breast core needle specimens is a new method for same-day diagnosis.** *Am J Surg* 2003, **186**(6):737-741; discussion 742.
151. Shah VI, Raju U, Chitale D, Deshpande V, Gregory N, Strand V: **False-negative core needle biopsies of the breast: an analysis of clinical, radiologic, and pathologic findings in 27 concecutive cases of missed breast cancer**. *Cancer* 2003, **97**(8):1824-1831.
152. Boughey JC, Hieken TJ, Jakub JW, Degnim AC, Grant CS, Farley DR, Thomsen KM, Osborn JB, Keeney GL, Habermann EB: **Impact of analysis of frozen-section margin on reoperation rates in women undergoing lumpectomy for breast cancer: evaluation of the National Surgical Quality Improvement Program data**. *Surgery* 2014, **156**(1):190-197.
153. Esbona K, Li Z, Wilke LG: **Intraoperative imprint cytology and frozen section pathology for margin assessment in breast conservation surgery: a systematic review**. *Ann Surg Oncol* 2012, **19**(10):3236-3245.
154. Osborn JB, Keeney GL, Jakub JW, Degnim AC, Boughey JC: **Cost-effectiveness analysis of routine frozen-section analysis of breast margins compared with reoperation for positive margins**. *Ann Surg Oncol* 2011, **18**(11):3204-3209.
155. Laucirica R: **Intraoperative assessment of the breast: guidelines and potential pitfalls**. *Arch Pathol Lab Med* 2005, **129**(12):1565-1574.
156. Thill M, Baumann K, Barinoff J: **Intraoperative assessment of margins in breast conservative surgery--still in use?** *J Surg Oncol* 2014, **110**(1):15-20.
157. Dabbs DJ, Grenko RT, Silverman JF: **FINE-NEEDLE ASPIRATION CYTOLOGY OF PLEOMORPHIC LOBULAR CARCINOMA OF THE BREAST - DUCT CARCINOMA AS A DIAGNOSTIC PITFALL**. *Acta Cytologica* 1994, **38**(6):923-926.
158. Yeh IT, Mies C: **Application of immunohistochemistry to breast lesions**. *Arch Pathol Lab Med* 2008, **132**(3):349-358.
159. Paredes J, Correia AL, Ribeiro AS, Albergaria A, Milanezi F, Schmitt FC: **P-cadherin expression in breast cancer: a review**. *Breast Cancer Res* 2007, **9**(5):214.
160. Moll R, Mitze M, Frixen UH, Birchmeier W: **Differential loss of E-cadherin expression in infiltrating ductal and lobular breast carcinomas**. *Am J Pathol* 1993, **143**(6):1731-1742.
161. Acs G, Lawton TJ, Rebbeck TR, LiVolsi VA, Zhang PJ: **Differential expression of E-cadherin in lobular and ductal neoplasms of the breast and its biologic and diagnostic implications**. *Am J Clin Pathol* 2001, **115**(1):85-98.
162. Palacios J, Sarrió D, García-Macias MC, Bryant B, Sobel ME, Merino MJ: **Frequent E-cadherin gene inactivation by loss of heterozygosity in pleomorphic lobular carcinoma of the breast**. *Mod Pathol* 2003, **16**(7):674-678.

163. Kowalski PJ, Rubin MA, Kleer CG: **E-cadherin expression in primary carcinomas of the breast and its distant metastases**. *Breast Cancer Res* 2003, **5**(6):R217-222.
164. Pinto MP, Badtke MM, Dudevoir ML, Harrell JC, Jacobsen BM, Horwitz KB: **Vascular endothelial growth factor secreted by activated stroma enhances angiogenesis and hormone-independent growth of estrogen receptor-positive breast cancer**. *Cancer Res* 2010, **70**(7):2655-2664.
165. Werling RW, Hwang H, Yaziji H, Gown AM: **Immunohistochemical distinction of invasive from noninvasive breast lesions: a comparative study of p63 versus calponin and smooth muscle myosin heavy chain**. *Am J Surg Pathol* 2003, **27**(1):82-90.
166. Dewar R, Fadare O, Gilmore H, Gown AM: **Best practices in diagnostic immunohistochemistry: myoepithelial markers in breast pathology**. *Arch Pathol Lab Med* 2011, **135**(4):422-429.
167. Palacios J, Benito N, Pizarro A, Suárez A, Espada J, Cano A, Gamallo C: **Anomalous expression of P-cadherin in breast carcinoma. Correlation with E-cadherin expression and pathological features**. *Am J Pathol* 1995, **146**(3):605-612.
168. Kovács A, Dhillon J, Walker RA: **Expression of P-cadherin, but not E-cadherin or N-cadherin, relates to pathological and functional differentiation of breast carcinomas**. *Mol Pathol* 2003, **56**(6):318-322.
169. BLOOM HJ, RICHARDSON WW: **Histological grading and prognosis in breast cancer; a study of 1409 cases of which 359 have been followed for 15 years**. *Br J Cancer* 1957, **11**(3):359-377.
170. Gilchrist KW, Kalish L, Gould VE, Hirschl S, Imbriglia JE, Levy WM, Patchefsky AS, Penner DW, Pickren J, Roth JA *et al*: **INTEROBSERVER REPRODUCIBILITY OF HISTOPATHOLOGICAL FEATURES IN STAGE-II BREAST-CANCER - AN ECOG STUDY**. *Breast Cancer Research and Treatment* 1985, **5**(1):3-10.
171. Ladekarl M, Sørensen FB: **Quantitative histopathological variables in in situ and invasive ductal and lobular carcinomas of the breast**. *APMIS* 1993, **101**(12):895-903.
172. Ozaki D, Kondo Y: **Comparative morphometric studies of benign and malignant intraductal proliferative lesions of the breast by computerized image analysis**. *Hum Pathol* 1995, **26**(10):1109-1113.
173. Rajesh L, Dey P, Joshi K: **Automated image morphometry of lobular breast carcinoma**. *Anal Quant Cytol Histol* 2002, **24**(2):81-84.
174. Latson L, Sebek B, Powell KA: **Automated cell nuclear segmentation in color images of hematoxylin and eosin-stained breast biopsy**. *Analytical and Quantitative Cytology and Histology* 2003, **25**(6):321-331.
175. Gupta S, Gupta R, Singh S, Gupta K, Kaur CJ: **Role of morphometry in evaluation of cytologically borderline breast lesions: a study of 70 cases**. *Diagn Cytopathol* 2012, **40**(3):191-196.
176. Mayr NA, Staples JJ, Robinson RA, VanMetre JE: **Intraductal breast carcinoma: initial results of a morphometric study using computerized digital image analysis**. *Clin Oncol (R Coll Radiol)* 1990, **2**(2):66-70.
177. Anderson NH, Hamilton PW, Bartels PH, Thompson D, Montironi R, Sloan JM: **Computerized scene segmentation for the discrimination of architectural features in ductal proliferative lesions of the breast**. *J Pathol* 1997, **181**(4):374-380.
178. Gao J, McNutt MA, Yi W, Chen J, Gu J: **Quantitative morphometry by image analysis of normal, hyperplastic and cancerous ductal breasts**. *Anal Quant Cytol Histol* 2009, **31**(5):255-261.
179. Nyirenda N, Farkas DL, Ramanujan VK: **Preclinical evaluation of nuclear morphometry and tissue topology for breast carcinoma detection and margin assessment**. *Breast Cancer Res Treat* 2011, **126**(2):345-354.
180. Nandakumar V, Kelbauskas L, Hernandez KF, Lintecum KM, Senechal P, Bussey KJ, Davies PC, Johnson RH, Meldrum DR: **Isotropic 3D nuclear morphometry of normal, fibrocystic and**

malignant breast epithelial cells reveals new structural alterations. *PLoS One* 2012, **7**(1):e29230.

181. Pierce M, Yu D, Richards-Kortum R: **High-resolution fiber-optic microendoscopy for in situ cellular imaging**. *J Vis Exp* 2011(47).
182. Muldoon TJ, Thekkek N, Roblyer D, Maru D, Harpaz N, Potack J, Anandasabapathy S, Richards-Kortum R: **Evaluation of quantitative image analysis criteria for the high-resolution microendoscopic detection of neoplasia in Barrett's esophagus**. *J Biomed Opt* 2010, **15**(2):026027.
183. Thekkek N, Richards-Kortum R: **Optical imaging for cervical cancer detection: solutions for a continuing global problem**. *Nat Rev Cancer* 2008, **8**(9):725-731.
184. Thekkek N, Anandasabapathy S, Richards-Kortum R: **Optical molecular imaging for detection of Barrett's-associated neoplasia**. *World J Gastroenterol* 2011, **17**(1):53-62.
185. Mueller JL, Harmany ZT, Mito JK, Kennedy SA, Kim Y, Dodd L, Geradts J, Kirsch DG, Willett RM, Brown JQ *et al*: **Quantitative Segmentation of Fluorescence Microscopy Images of Heterogeneous Tissue: Application to the Detection of Residual Disease in Tumor Margins**. *PLoS One* 2013, **8**(6):e66198.
186. Kyrish M, Dobbs J, Jain S, Wang X, Yu D, Richards-Kortum R, Tkaczyk TS: **Needle-based fluorescence endomicroscopy via structured illumination with a plastic, achromatic objective**. *J Biomed Opt* 2013, **18**(9):096003.
187. Matas J, Chum O, Urban M, Pajdla T: **Robust wide-baseline stereo from maximally stable extremal regions**. *Image and Vision Computing* 2004, **22**(10):761-767.
188. Schondorf H, Naujoks H: **DETERMINING THE NUCLEAR-AREA IN NORMAL BREAST EPITHELIA AND IN THE NUCLEI OF MAMMARY CARCINOMAS**. *Journal of Cancer Research and Clinical Oncology* 1985, **109**(3):241-244.
189. Foote FW, Stewart FW: **Lobular carcinoma in situ: A rare form of mammary cancer**. *Am J Pathol* 1941, **17**(4):491-496.493.
190. Bedard N: **Multi-Modal Imaging Techniques for Early Cancer Diagnostics**. Houston, TX, USA: Rice University; 2012.
191. Walter M, Liang S, Ghosh S, Hornsby PJ, Li R: **Interleukin 6 secreted from adipose stromal cells promotes migration and invasion of breast cancer cells**. *Oncogene* 2009, **28**(30):2745-2755.
192. Liu E, Samad F, Mueller BM: **Local adipocytes enable estrogen-dependent breast cancer growth: Role of leptin and aromatase**. *Adipocyte* 2013, **2**(3):165-169.
193. Iyengar P, Espina V, Williams TW, Lin Y, Berry D, Jelicks LA, Lee H, Temple K, Graves R, Pollard J *et al*: **Adipocyte-derived collagen VI affects early mammary tumor progression in vivo, demonstrating a critical interaction in the tumor/stroma microenvironment**. *Journal of Clinical Investigation* 2005, **115**(5):1163-1176.
194. Conklin MW, Keely PJ: **Why the stroma matters in breast cancer Insights into breast cancer patient outcomes through the examination of stromal biomarkers**. *Cell Adhesion & Migration* 2012, **6**(3):249-260.
195. Konda VJ, Meining A, Jamil LH, Giovannini M, Hwang JH, Wallace MB, Chang KJ, Siddiqui UD, Hart J, Lo SK *et al*: **A pilot study of in vivo identification of pancreatic cystic neoplasms with needle-based confocal laser endomicroscopy under endosonographic guidance**. *Endoscopy* 2013, **45**(12):1006-1013.
196. Cotruta B, Gheorghe C, Bancila I: **Magnifying endoscopy with narrow-band imaging or confocal laser endomicroscopy for in vivo rapid diagnostic of Barrett's esophagus**. *J Gastrointestin Liver Dis* 2009, **18**(2):258-259.

197. Bojarski C, Günther U, Rieger K, Heller F, Loddenkemper C, Grünbaum M, Uharek L, Zeitz M, Hoffmann JC: **In vivo diagnosis of acute intestinal graft-versus-host disease by confocal endomicroscopy**. *Endoscopy* 2009, **41**(5):433-438.
198. Thekkek N, Muldoon T, Polydorides AD, Maru DM, Harpaz N, Harris MT, Hofstettor W, Hiotis SP, Kim SA, Ky AJ *et al*: **Vital-dye enhanced fluorescence imaging of GI mucosa: metaplasia, neoplasia, inflammation**. *Gastrointest Endosc* 2012, **75**(4):877-887.
199. Thekkek N, Pierce MC, Lee MH, Polydorides AD, Flores RM, Anandasabapathy S, Richards-Kortum RR: **Modular video endoscopy for in vivo cross-polarized and vital-dye fluorescence imaging of Barrett's-associated neoplasia**. *J Biomed Opt* 2013, **18**(2):26007.
200. Groot G, Rees H, Pahwa P, Kanagaratnam S, Kinloch M: **Predicting local recurrence following breast-conserving therapy for early stage breast cancer: The significance of a narrow (≤2 mm) surgical resection margin**. *J Surg Oncol* 2011.
201. Ashwell M, Priest P, Bondoux M, Sowter C, McPherson CK: **Human fat cell sizing--a quick, simple method**. *J Lipid Res* 1976, **17**(2):190-192.
202. Sjöström L, Björntorp P, Vrána J: **Microscopic fat cell size measurements on frozen-cut adipose tissue in comparison with automatic determinations of osmium-fixed fat cells**. *J Lipid Res* 1971, **12**(5):521-530.
203. Björnheden T, Jakubowicz B, Levin M, Odén B, Edén S, Sjöström L, Lönn M: **Computerized determination of adipocyte size**. *Obes Res* 2004, **12**(1):95-105.
204. Chen HC, Farese RV: **Determination of adipocyte size by computer image analysis**. *J Lipid Res* 2002, **43**(6):986-989.
205. Osman OS, Selway JL, Kepczynska MA, Stocker CJ, O'Dowd JF, Cawthorne MA, Arch JR, Jassim S, Langlands K: **A novel automated image analysis method for accurate adipocyte quantification**. *Adipocyte* 2013, **2**(3):160-164.
206. Horst KC, Smitt MC, Goffinet DR, Carlson RW: **Predictors of local recurrence after breast-conservation therapy**. *Clin Breast Cancer* 2005, **5**(6):425-438.
207. Moran MS, Schnitt SJ, Giuliano AE, Harris JR, Khan SA, Horton J, Klimberg S, Chavez-MacGregor M, Freedman G, Houssami N *et al*: **Society of Surgical Oncology-American Society for Radiation Oncology consensus guideline on margins for breast-conserving surgery with whole-breast irradiation in stages I and II invasive breast cancer**. *Ann Surg Oncol* 2014, **21**(3):704-716.
208. Singletary SE: **Surgical margins in patients with early-stage breast cancer treated with breast conservation therapy**. *Am J Surg* 2002, **184**(5):383-393.
209. D'Halluin F, Tas P, Rouquette S, Bendavid C, Foucher F, Meshba H, Blanchot J, Coué O, Levêque J: **Intra-operative touch preparation cytology following lumpectomy for breast cancer: a series of 400 procedures**. *Breast* 2009, **18**(4):248-253.
210. Quinn MK, Bubi TC, Pierce MC, Kayembe MK, Ramogola-Masire D, Richards-Kortum R: **High-Resolution Microendoscopy for the Detection of Cervical Neoplasia in Low-Resource Settings**. *Plos One* 2012, **7**(9).
211. Arbyn M, Sankaranarayanan R, Muwonge R, Keita N, Dolo A, Mbalawa CG, Nouhou H, Sakande B, Wesley R, Somanathan T *et al*: **Pooled analysis of the accuracy of five cervical cancer screening tests assessed in eleven studies in Africa and India**. *Int J Cancer* 2008, **123**(1):153-160.
212. Ghosh P, Gandhi G, Kochhar PK, Zutshi V, Batra S: **Visual inspection of cervix with Lugol's iodine for early detection of premalignant & malignant lesions of cervix**. *Indian J Med Res* 2012, **136**(2):265-271.
213. McCaul JA, Cymerman JA, Hislop S, McConkey C, McMahon J, Mehanna H, Shaw R, Sutton DN, Dunn J: **LIHNCS - Lugol's iodine in head and neck cancer surgery: a multicentre, randomised controlled trial assessing the effectiveness of Lugol's iodine to assist excision of moderate**

dysplasia, severe dysplasia and carcinoma in situ at mucosal resection margins of oral and oropharyngeal squamous cell carcinoma: study protocol for a randomised controlled trial. *Trials* 2013, **14**:310.

214. Nakanishi Y, Ochiai A, Yoshimura K, Kato H, Shimoda T, Yamaguchi H, Tachimori Y, Watanabe H, Hirohashi S: **The clinicopathologic significance of small areas unstained by Lugol's iodine in the mucosa surrounding resected esophageal carcinoma: an analysis of 147 cases**. *Cancer* 1998, **82**(8):1454-1459.
215. Peng G, Long Q, Wu Y, Zhao J, Chen L, Li X: **Evaluation of double vital staining with lugol's iodine and methylene blue in diagnosing superficial esophageal lesions**. *Scandinavian Journal of Gastroenterology* 2011, **46**(4):8.
216. Zuluaga AF, Drezek R, Collier T, Lotan R, Follen M, Richards-Kortum R: **Contrast agents for confocal microscopy: how simple chemicals affect confocal images of normal and cancer cells in suspension**. *J Biomed Opt* 2002, **7**(3):398-403.
217. Dawsey SM, Fleischer DE, Wang GQ, Zhou B, Kidwell JA, Lu N, Lewin KJ, Roth MJ, Tio TL, Taylor PR: **Mucosal iodine staining improves endoscopic visualization of squamous dysplasia and squamous cell carcinoma of the esophagus in Linxian, China**. *Cancer* 1998, **83**(2):220-231.
218. Petruzzi M, Lucchese A, Baldoni E, Grassi FR, Serpico R: **Use of Lugol's iodine in oral cancer diagnosis: an overview**. *Oral Oncol* 2010, **46**(11):811-813.
219. Fokom-Domgue J, Combescure C, Fokom-Defo V, Tebeu PM, Vassilakos P, Kengne AP, Petignat P: **Performance of alternative strategies for primary cervical cancer screening in sub-Saharan Africa: systematic review and meta-analysis of diagnostic test accuracy studies**. *BMJ* 2015, **351**:h3084.
220. Baraldi A, Parmiggiani F: **AN INVESTIGATION OF THE TEXTURAL CHARACTERISTICS ASSOCIATED WITH GRAY-LEVEL COOCCURRENCE MATRIX STATISTICAL PARAMETERS**. *Ieee Transactions on Geoscience and Remote Sensing* 1995, **33**(2):293-304.
221. Elston CW, Sloane JP, Amendoeira I, Apostolikas N, Bellocq JP, Bianchi S, Boecker W, Bussolati G, Coleman D, Connolly CE *et al*: **Causes of inconsistency in diagnosing and classifying intraductal proliferations of the breast. European Commission Working Group on Breast Screening Pathology**. *Eur J Cancer* 2000, **36**(14):1769-1772.
222. Turner RR, Weaver DL, Cserni G, Lester SC, Hirsch K, Elashoff DA, Filzgibbons PL, Viale G, Mazzarol G, Ibarra JA *et al*: **Improving interobserver reproducibility of nodal stage classification through standardized histologic criteria and image-based training**. *Modern Pathology* 2008, **21**:57A-57A.
223. Cerussi A, Shah N, Hsiang D, Durkin A, Butler J, Tromberg BJ: **In vivo absorption, scattering, and physiologic properties of 58 malignant breast tumors determined by broadband diffuse optical spectroscopy**. *Journal of Biomedical Optics* 2006, **11**(4).
224. Tanamai W, Chen C, Siavoshi S, Cerussi A: **Diffuse optical spectroscopy measurements of healing in breast tissue after core biopsy: case study**. *Journal of Biomedical Optics* 2009, **14**(1).
225. Rajadhyaksha M, Gonzalez S, Zavislan JM, Anderson RR, Webb RH: **In vivo confocal scanning laser microscopy of human skin II: Advances in instrumentation and comparison with histology**. *Journal of Investigative Dermatology* 1999, **113**(3):293-303.
226. Rajadhyaksha M, Menaker G, Flotte T, Dwyer PJ, Gonzalez S: **Confocal examination of nonmelanoma cancers in thick skin excisions to potentially guide mohs micrographic surgery without frozen histopathology**. *Journal of Investigative Dermatology* 2001, **117**(5):1137-1143.
227. White WM, Tearney GJ, Pilch BZ, Fabian RL, Anderson RR, Gaz RD: **A novel, noninvasive imaging technique for intraoperative assessment of parathyroid glands: Confocal reflectance microscopy**. *Surgery* 2000, **128**(6):1088-1100.

228. Ruffell B, Au A, Rugo HS, Esserman LJ, Hwang ES, Coussens LM: **Leukocyte composition of human breast cancer**. *Proc Natl Acad Sci U S A* 2012, **109**(8):2796-2801.
229. Boutonnat J, Barbier M, Muirhead K, Mousseau M, Ronot X, Seigneurin D: **Optimized fluorescent probe combinations for evaluation of proliferation and necrosis in anthracycline-treated leukaemic cell lines**. *Cell Prolif* 1999, **32**(4):203-213.
230. Dirat B, Bochet L, Escourrou G, Valet P, Muller C: **Unraveling the obesity and breast cancer links: a role for cancer-associated adipocytes?** *Endocrine development* 2010, **19**:45-52.
231. Ford TN, Lim D, Mertz J: **Fast optically sectioned fluorescence HiLo endomicroscopy**. *Journal of Biomedical Optics* 2012, **17**(2):7.